DYNAMIC DARK STATE DEPLETION
A PATH TO HIGH SENSITIVITY IMAGING

A Dissertation
Presented to
The Academic Faculty

By

Christopher I. Richards

In Partial Fulfillment
Of the Requirements for the Degree
Doctor of Philosophy in the
School of Chemistry & Biochemistry

Georgia Institute of Technology

December 2009

DYNAMIC DARK STATE DEPLETION
A PATH TO HIGH SENSITIVITY IMAGING

Approved by:

Professor Robert M. Dickson,
Advisor
School of Chemistry and
Biochemistry
Georgia Institute of Technology

Professor Christoph Fahrni
School of Chemistry and
Biochemistry
Georgia Institute of Technology

Professor Christine Payne
School of Chemistry and
Biochemistry
Georgia Institute of Technology

Professor Mohan Srinivasarao
School of Chemistry and
Biochemistry, School of
Polymer, Textile, and Fiber
Engineering
Georgia Institute of Technology

Professor Jeff Petty
School of Chemistry
Furman University

Date Approved October, 2nd, 2009

ACKNOWLEDGEMENTS

Grad school has been an interesting experience. Over the past five years, I've learned a lot from my time in the Dickson lab, both in the world of science and rather surprisingly about the game of ping-pong. I am indebted to my advisor, Robert Dickson, for given me the opportunity to pursue an interesting course of research from which I've learned more than I ever thought possible. Several individuals were instrumental in any success that I've had, including in no particular order Yasuko Antoku, Sandeep Patel, Tom Vosch, Dulal Senapati, Rusty Nicovich, Junhua Yu, Sungmoon Choi, Jeng-Cheng Hsiang, Soonkyo Jung, Andrew Khalil, Nathan Hull, Aaron Danberry, and Chaoyang Fan.

My ping-pong skills, on the other hand, remain marginal at best. This is, however, in no way the fault of my two primary instructors, Junhua Yu and Soonkyo Jung, under whose diligent tutelage I have mastered the forehand top-spin stroke.

Finally, I would also like to thank my family, particularly my wife, Katie, for her unlimited patience and constant understanding. With only a little prodding, I'm hanging up the ping-pong paddle and getting back to the real world.

TABLE OF CONTENTS

LIST OF TABLES

LIST OF FIGURES

LIST OF SYMBOLS AND ABBREVIATIONS

Φ	Quantum yield
k_{ex}	Excitation rate
S_0	Ground state
S_1	Excited state
σ	Absorption cross section
I	Intensity
k_{fl}	Fluorescence rate
D	Dark state
τ_{on}	On time
τ_{off}	Off time
k_{ds}	Dark state population rate
FCS	Fluorescence correlation spectroscopy
HOMO	Highest occupied molecular orbital
LUMO	Lowest unoccupied molecular orbital
k_{et}	Energy transfer rate
r	Radius
R_0	Hydrodynamic radius
FRET	Fluorescence resonance energy transfer
TCSPC	Time-correlated single photon counting
PEG	Poly ethylene glycol
APD	Avalanche photo diode
PMT	Photo multiplier tube
CCD	Charge coupled device

SUMMARY

Silver nanoclusters encapsulated in oligonucleotide scaffolds exhibit remarkably bright emission at both the bulk and single molecule level. With emissive species across the visible and into the near infrared, these clusters offer the potential to create a new class of biological labels with vast improvements over existing dyes.

Here we evaluate and optimize many of the characteristics necessary for extending these fluorophores toward eventual applications in biological imaging. Through spectral purification, photophysical characterization at the bulk and single molecule level was achieved for several fluorescent species. Studies reveal the presence of a microsecond blinking component resulting from a short-lived dark state. The lack of intermittency on a longer time scale leads to much higher emission rates than common organic dyes.

This dark state was found to be photo-accessible with a very efficient depopulation transition leading to repopulation of the emissive state. Secondary excitation on resonance with this transition significantly shortens the residence time in the dark state giving rise to as much as 5-fold fluorescence enhancement. Manipulation of the secondary laser can be used to impose a specific waveform onto the fluorescent signal resulting in a regular modulation of the emission. Signal processing techniques can be employed to extract the modulated signal from large backgrounds, leading to drastically improved sensitivity.

This new imaging concept can be extended, beyond Ag nanoclusters, to common organic fluorophores that demonstrate large dark state quantum yields. These

fluorophores simultaneously illustrate the utility of this technique and help to define a general set of parameters for engineering ideal dyes for modulated signal extraction. Ideally suited for fluorescence enhancement, FRET pairs can be used to engineer a wide range of modulatable systems, based on detecting donor emission in the presence of a laser directly exciting the acceptor. The utility of Ag nanoclusters, organic dyes, and FRET systems for improved sensitivity are thoroughly investigated in this work.

CHAPTER 1
INTRODUCTION

1.1 Motivation

Primarily through technological developments, fluorescence microscopy has been instrumental in recent advancements in biological imaging.[1-9] New techniques have enabled investigators to address numerous biological questions such as those involving cellular pathways[10,11] and protein dynamics.[12,13] Despite our greater understanding of biological function, two fundamental problems persist- limited spatial resolution[14-16] and poor signal sensitivity.[2,5] The intricacy of biological measurements has grown as efforts to extract information target ever smaller subcellular components.[17,18] This emphasis on distinguishing features with better resolution and higher sensitivity constantly pushes the limits of existing technology. Beginning with the earliest microscopes, a steady and concerted effort has been made toward the development of newer and better technology as is necessary to address the increasingly complex issues related to both resolution and sensitivity.

Antoni van Leeuwenhoeck's 17th century development of a simple microscope using transmitted light to view microbes exposed a previously invisible world laying the foundation for many technological advances over the next few centuries.[19] Steady advancements in optical microscopy helped lead to the discovery and visualization of microbes associated with diseases such as tuberculosis and cholera.[20] With a push toward even smaller size regimes, other complementary microscopy techniques were developed. With the advent of electron microscopy in the 1930s, tremendously detailed images of minuscule cellular components were now easily obtained. The power of this technique to

conceptualize basic biological structure is best illustrated in its early use to comprehensively solve virus structures.[20] While morphology is readily resolved, the static images associated with electron microscopy are incompatible with understanding cellular function.

Proteins involved in specific biological processes are typically indistinguishable from the many other components in the cell using either optical microscopy or electron microscopy. Thus, visualization of cellular dynamics requires the isolation of subcellular components such that they can be discriminated from the rest of the cell. Coming to prominence during the middle of the 20th century, fluorescence microscopy has facilitated many advances in cellular dynamics. Attaching a fluorescent molecule to particular proteins allows specific visualization of that protein through the label's fluorescence. The utility of this technique was first demonstrated by Coons and Kaplan in the 1950s. Covalently attaching a fluorophore to an antibody, they showed that the antibody-antigen interaction could be visualized using fluorescence microscopy.[21-23] The elegant nature and specificity of these interactions are ideal for cellular dynamics as the fluorescent marker affects no other proteins. Despite this progress many challenges remain. Many cellular components naturally fluoresce which can interfere with the detection of the fluorescent label.[24] The complex dynamics of smaller size regimes often involve low copy number proteins limiting the number of fluorescent labels. As a result, the inherent cellular fluorescence can obscure the relatively dim fluorescence signal. This lack of experimental sensitivity thwarts efforts to resolve many dynamic processes and limits structural determinations. Basic experimental considerations can be advantageously employed to optimize the sensitivity, but such optimization is most often limited by the

intrinsic properties of the fluorescent label. Factors such as probe brightness, photostability, blinking dynamics, and overall size contribute to the performance of fluorophores in biological systems. Techniques including total internal reflection,[25,26] multi-photon excitation,[27,28] and confocal microscopy[29,30] are among those most commonly used to improve sensitivity. Meaningful improvements over existing fluorophores would allow higher sensitivity measurements leading to imaging on faster time scales, labeling of smaller components, and determination of protein dynamics.

This work focuses on improving sensitivity in fluorescence imaging through the development of novel fluorophores and new imaging concepts. I will demonstrate how the unique photophysical characteristics displayed by Ag nanoclusters can be advantageously employed and later extended to multiple fluorescent systems. By optically accessing normally detrimental dark states, external manipulation of fluorescence intermittency can be used to modify fluorescence properties including emission rates. This allows for controlled enhancement of fluorescence and increased sensitivity through optical modulation and specific extraction of fluorescent signals. The versatility of this technique to generate improved sensitivity suggests a wide range of possible applications in biological imaging.

1.2 Fluorescent Labels

Fluorescence microscopy is widely utilized in biological imaging,[31-34] providing detailed information about both cellular structure[35,36] and dynamics.[37,38] These studies are made possible by the labeling of proteins and other subcellular components with fluoresecent probes such as quantum dots,[39,40] organic dyes,[41,42] and fluorescent proteins.[43,44] The selection of the appropriate label is not a trivial matter and involves the

consideration of many factors. Not the least of which is brightness, which can simply be defined as the quantity of detected photons for a given excitation intensity. The two major attributes directly related to fluorophore brightness are extinction coefficient and quantum yield. The former is a measure of the ability of the fluorophore to absorb light thereby undergoing a transition that populates an excited state, while the latter describes the ratio of those excited electrons which undergo relaxation via the release of a photon. Clearly, the excitation rate can be increased giving higher emission rates, but biological imaging also suffers from very high background, resulting from cellular molecules with intrinsic fluorescence. So any increase in the excitation intensity simultaneously increases the background fluorescence. Biological imaging is not just a matter of brightness but more a matter of sensitivity. Naturally, higher quantum yields and higher extinction coefficients lead to brighter emission at lower excitation intensities, resulting in better experimental sensitivity. Commonly utilized organic dyes have extinction coefficients ranging from 50,000-300,000 M^{-1} cm^{-1} and quantum yields from 10% to 90%.[45-47] Even for the brightest of these dyes, sensitivity is still an issue in many applications,[2,5] as organic dyes exhibit insufficient emission rates as compared to background fluorescence.[48] In fact, existing fluorophores have been engineered to approach the limits of their brightness potential, leading to the exploration of alternative methods such as plasmon enhanced local excitation.[49] While moderate increases in brightness are realized through these alternatives, they come at the expense of biocompatibility and ease of conjugation, defeating two of the natural advantages of fairly well developed organic dye labeling.

Fluorescent proteins are typically not as bright as organic fluorophores with extinction coefficients of approximately 50,000 M^{-1} cm^{-1} and quantum yields approaching 50%.[50] Their ever increasing popularity in cellular applications, however, is not due to their brightness, but rather because they can be genetically encoded within biological systems.[51,52] Displaying relatively low emission rates, sensitivity for fluorescent proteins is an even bigger concern than for organic fluorophores. Despite these disadvantages fluorescent proteins are extremely popular in biologically imaging due to the elimination of exogenous based labeling of intracellular structures. This results in more well defined and precise labeling.[53] In contrast to fluorescent proteins, quantum dots are both brighter and significantly less biologically friendly. Exhibiting extremely large extinction coefficients that approach 10^6 M^{-1} cm^{-1}, quantum dots can be excited at extremely low intensities without sacrificing brightness.[54-56] The low excitation intensities minimize background fluorescence, resulting in much improved sensitivity. Thus, quantum dots can be more readily imaged in some cellular environments as they are visible above the background. Quantum dots, however, also suffer from multiple issues: their large size (30 nm), once functionalized, poor membrane permeability, and possible toxicity.[4] Despite their brightness, these factors tend to limit quantum dot applications in biological studies.

While these fluorescent systems exhibit varying levels of sensitivity, each offers advantages as well as disadvantages in terms of biological imaging applications. Many of the issues dealing with fluorophore brightness can be masked by simply increasing the labeling coverage for the biological system. When extending measurements to sub-cellular structures, however, the likelihood of system perturbation is increased with the

addition of multiple fluorescent probes. So while a high degree of labeling, as is normal in many ensemble experiments, can mask photophysical deficiencies, as the labeling coverage is reduced deleterious effects such as photobleaching and blinking dynamics start to dominate. Naturally, this diminishes the fluorophore's efficacy. At the single molecule level, this leads to additional and more complicated photophysics.

. 1.3 Single Molecule Measurements

Bulk imaging provides an extraordinary amount of information on biological systems. Helping to elucidate structure and cellular dynamics, these studies form the basis for most recent advancements in our understanding of subcellular components.[57-59] Single molecule imaging can be used as a complementary technique, providing more detailed understanding of cellular dynamics. Ensemble measurements by their nature average out individual dynamics, while single molecule studies allow the detection of kinetic events that help to define the function and illustrate the heterogeneity of molecules in the cell. Mainly demonstrated in vitro, single molecule spectroscopy has been used to study ambulatory motor proteins,[60,61] oligonucleotide folding,[62,63] and ribosome function.[64,65] Even more so than bulk studies, in vivo single molecule applications are limited by signal sensitivity.

Photophysical behavior affecting sensitivity that was concealed in ensemble experiments is often readily apparent in single molecule studies. A basic three level energy diagram (Figure 1.1) serves as an adequate representation to explain many of these processes. The rate of population ($\mathbf{k_{Ex}}$) of the singlet excited state ($\mathbf{S_1}$) is defined as the absorption cross section ($\boldsymbol{\sigma}$) multiplied by the excitation intensity ($\mathbf{I}$). As the

excitation intensity increases ($\mathbf{S_1}$) is populated at a faster rate. Fluorophore brightness is determined by the rate of fluorescence ($\mathbf{k_{Fl}}$), the population of the ($\mathbf{k_{Ex}}$), and the quantum yield ($\mathbf{\Phi}$). Once an electron reaches ($\mathbf{S_1}$) it can either return to ($\mathbf{S_0}$) via emission of a photon or it can take a non-radiative relaxation pathway. While exposed to an excitation source, the molecule continuously emits photons as the ($\mathbf{S_0}$) and ($\mathbf{S_1}$) states are alternately occupied. Ultimately the molecule transitions to a nonfluorescent state (**D**). This transition, $\mathbf{k_{dark}}$, typically has a low probability of occurring,[66,67] so requires several cycles into the singlet excited state before populating the dark state. The time the molecule spends steadily emitting by cycling between ($\mathbf{S_1}$) and ($\mathbf{S_0}$), before a dark state transition, is referred to as the "on time" ($\boldsymbol{\tau_{on}}$). The lifetime of (**D**) is referred to as the off time ($\boldsymbol{\tau_{off}}$). Higher excitation intensities lead to faster cycling into the emissive state, higher ($\mathbf{k_{Ex}}$), and result in a shorter ($\boldsymbol{\tau_{on}}$).

Ensemble experiments typically require modest excitation intensities limiting low probability transitions into the dark state. At the single molecule level, however, much higher intensities (> kW/cm^2) are required to produce detectable emission rates. Thus, transitions into the dark state occur much more often, typically in time frames less than 100 ms.[67] The transition ($\mathbf{k_{DS}}$) from (**D**) back to the emissive manifold also has a low probability of occurring, giving rise to long-lived dark states which can range from μs to seconds.[66,67] The overall emission rate is reduced based on the residence time in the dark state. The attenuation of the emission rate as a result of dark state population is shown in equation 1.1.

$$I = \frac{\tau_{on}}{\tau_{on} + \tau_{off}} I_{on} \qquad \text{Equation 1.1}$$

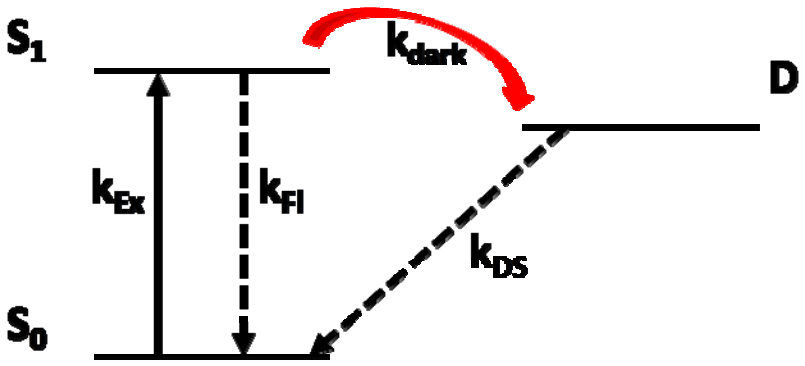

Figure 1.1. Typical three level energy diagram where S_0 is the ground singlet state, S_1 is the first single excited state, and D is the dark state. The rate of excitation from S_0 to S_1 is designated as k_{Ex}, the rate of fluorescence is k_{Fl}, the rate of intersystem crossing to the triplet state is k_{dark}, and the rate of non-radiative decay from the triplet back to the singlet ground state is k_{DS}.

At the single molecule level almost all fluorophores have been shown to exhibit blinking on time scales ranging from microseconds to a few seconds, including organic dyes;[68-70] fluorescent proteins;[71,72] and quantum dots.[73-75] Population of the dark state results in premature saturation of the fluorescence, resulting in the loss of the expected linear response of emitted light with increasing excitation intensities. Fluorescence intermittency (blinking) gives rise to other issues as well. Occupation of the dark state has also been shown to be extremely sensitive to the environment, particularly on conjugation to proteins or oligonucleotides.[76,77] In Fact, labeling of some systems can lead to increased blinking.[76,77]. Often these dark states, particularly those of triplet origin, are exceptionally reactive, potentially leading to permanent photobleaching.[78,79]

Correlation analysis has become a very powerful tool in examining the properties of dark state dynamics, successfully revealing transition probabilities and residence times in dilute solutions and immobilized molecules.[68,80-83] For example, commonly used cyanine dyes have shown complicated blinking dynamics consisting of both a triplet state and a non fluorescent photoaccessible isomer.[84,85] Despite having ensemble photophysics that should yield extremely bright single molecules, the blinking dynamics from both of these dark states result in premature saturation such that it leads to significantly lower single molecule emission rates.[85] A major issue revealed by characterization of blinking behavior is that it often occurs on the same time scale as biologically relevant dynamics, increasing the potential masking of important cellular processes.

1.4 Fluorophore Photostability

Another common issue for both bulk and ensemble imaging is photobleaching, which also has a well defined quantum yield and is equally dependent on the excitation

intensity. The best organic dyes undergo approximately ~10^7 excitation cycles before permanently photobleaching.[79] Assuming a moderate quantum yield of 50% and a detection efficiency of 5%, excitation of a typical single molecule results in approximately 250,000 total detected photons before irreversibly bleaching. In bulk imaging, photobleaching leads to a steady decrease in the emission. Often in samples where brightness is an issue, higher excitation intensities are needed to increase emission rates leading directly to more rapid photobleaching. As the sample will eventually lose all fluorescence, the duration of experiments are limited by this process. Imaging applications need to balance using a high enough excitation intensity to generate sufficient brightness and using a low enough intensity that bleaching can be avoided long enough to collect relevant data. This is particularly evident in the imaging of many smaller sub-cellular structures, which utilize fewer fluorescent labels so that higher excitation intensities are needed to generate sufficient emission.

Photobleaching in organic fluorophores is widely believed to result from population of highly reactive triplet dark states.[86,87] The long residence time in this more reactive state increases the probability of a covalent reaction that modifies the dye in such a way that it becomes permanently nonfluorescent. Leading directly to shorter on times, higher excitation intensities result in both increased background and premature bleaching due to population of reactive dark states. Clearly many of the issues encountered in biological imaging are interrelated, where photophysical processes, such as blinking, affect fluorophore behavior. Further advances in biological imaging would be assisted by more stable dyes.

1.5 Metal Cluster Theory

The size dependent properties of noble metals in the nanometer regime have been the focus of an increasing amount of research.[88,89] Such characteristics, derived from the electronic structure of these metals with electrons occupying a filled d shell and an additional electron in an s orbital, lead to unique behavior. For metals the outermost electrons are traditionally considered free electrons in the sense that within bulk metal they are delocalized and moving independently within the crystal lattice.[90] It was originally proposed by Drude that the system of free electrons could be treated as an ideal gas and thus subject to behavior based the same fundamental properties.[90,91] Then these free moving electrons would be vulnerable to collisions and scattering with both other electrons and the rather static positive ions within the crystal lattice.[91] The electronic equation of motion is described by

$$\frac{d}{dt}p(t) = qE - \frac{p(t)}{T} \qquad \text{Equation 1.2}$$

where t = time, p = electron momentum, q = charge, E = electric field, and T = mean free time between collisions. Electron interactions between collisions can be neglected, and the free electrons can act in concert rather than as individual electrons. Under certain excitation energies the entire electron cloud is simultaneously excited as a group as opposed to individually. This plasmon absorption of the collective at the proper frequency leads to electron oscillations at the same frequency as the originally absorbed light.[91]

Bulk metals exhibit a continuous density of states giving freedom of motion for the electrons due to lack of band gap formation.[91] These continuous states as described by band theory are related to the overlapping atomic orbitals. At large numbers of atoms

the resulting atomic orbitals lead to the number of molecular orbitals. The resulting band structure, valence and conduction bands, are so close in energy for a metal that no band gap exists. However as the number of orbitals is reduced, as a result of smaller particle size, the conduction and valence bands become discrete leading to an energy gap that increases with decreasing size .[92] The energy level spacing, δ, can be represented by

$$\delta = \frac{E_F}{N} \qquad \text{Equation 1.3}$$

where E_F is the Fermi level and N is the number of conduction electrons. This becomes particularly relevant to the electronic properties of the metal cluster when the size approaches that of the deBroglie wavelength of electrons at the Fermi energy level, at which point the system clearly exhibits molecular states.[93] Thus, clusters of this size develop molecular properties such as a separation between electronic states analogous to the commonly used terminology for molecules of HOMO and LUMO. At small size regimes visible and near infrared light should be sufficient to populate excited states and open the possibility of radiative decay in form of fluorescence.

1.6 Silver Clusters

In an aqueous environment without the benefit of a scaffold or template, aggregation of free silver atoms quickly leads to particles that are orders of magnitude larger than what could conceivably give well defined molecular behavior. As a result, the formation of small silver clusters in aqueous solutions has proved challenging. Alternatively, encapsulation via low temperature rare gas matrices produced the first observable demonstration of electronic transitions yielding Ag nanocluster

fluorescence.[94,95] Producing clusters ranging from 2 to 8 atoms encapsulated primarily in argon and krypton gas matrices, these studies nicely demonstrated that fluorescence can readily be generated from small silver clusters.

In argon matrices, emission peaks at 478 nm and 620 nm were assigned to Ag_2 and Ag_3, respectively, with an additional peak at 699 nm also designated as Ag3.[96] Other studies in similar matrices showed a number of emission peaks (278 nm, 286 nm, and 479 nm) generated from excitation of the Ag dimer. The same study also reported peaks for the trimer at 374nm, 616 nm, and 705 nm.[97] Further studies showed similar trends for Ag clusters, including those incorporating up to 8 atoms.[98,99] These studies demonstrated for the first time that the theorized emission from small Ag nanoclusters could be experimentally observed via controlled cluster formation. In order to make Ag nanoclusters more viable as fluorescent probes, efficient encapsulation was required beyond the somewhat idealized conditions of trapping in rare gas matrices.

Extending the formation of Ag nanoclusters to aqueous environments, Henglein used a polyphosphate to encapsulate Ag ions with subsequent γ ray exposure leading to reduction of the Ag ions and formation of various clusters.[100-102] Due to inefficient scaffolding, the survival time of the clusters before aggregation was too short to detect emission, but the authors were able to record absorption spectra of a number of species with various charged states. These studies confirmed that discrete transitions, in the form of absorption bands, can be observed for Ag nanoclusters ranging from 2 to 4 atoms in aqueous environments.[101,103] While a useful development, the short survival time and the lack of demonstrated fluorescence showed the need for a more suitable scaffold. Further studies have shown that PAMAM dendrimer scaffolds effectively encapsulate small Ag

nanoclusters leading to emission across the visible and near infrared.[104,105] These clusters, while exhibiting extremely bright fluorescence even at the single molecule level, were incompatible with biological imaging as they could not be formed in sufficient quantities. While not fully functional for use as biological probes, the presence of bright fluorescent Ag clusters illustrated that Ag nanoclusters in aqueous solutions maintained the same emissive properties as previously seen in rare gas matrices.

Building on the success seen in other scaffolds, more recently both oligonucleotides and peptides have been shown to effectively protect Ag nanoclusters from aggregation, resulting in a variety of fluorescent species.[83,106-110] With emission across the visible into the infrared, oligonucleotide encapsulated Ag nanoclusters exhibit high quantum yields and extinction coefficients, leading to extremely bright emission. While limited in their scope initial studies showed that ssDNA encapsulated Ag nanoclusters exhibited interesting and unique photophysical properties.[83] In depth characterization of these photophysical parameters is the partial basis for the work detailed in this thesis.

1.7 DNA-Ag Interactions

While the fundamental purpose of DNA is to store the genetic information necessary for the replication of biological systems, DNA has also been extensively employed as a scaffold.[111,112] Composed of a negatively charged phosphodiester backbone structure, oligonucleotides are well suited for applications in aqueous solutions and have been shown to bind a wide range of metal ions.[113] Ideally composed of distinct building blocks in the form of natural bases (cytosine, guanine, adenine, and thymine), DNA machinery can be programmed to assemble nano-sized structures based on sequence,

length, and conformation.[114-117] These structures range from relatively simple nanowires[118-120] to increasingly complex three dimensional networks.[121] While nanowires down to 10 nm can be constructed with DNA templates using a variety of metals including both gold[118,120] and silver[118,119], more elaborate structures such as Ag nanorings can also be constructed using the correct parameters.[121] The methods involved in the construction of the Ag nanorings were based on the ability of long strands of DNA to form toroidal structures via condensation. Ag ions were readily bound to the DNA structure and subsequently reduced yielding silver structures matching the shape of the DNA template. Such facile synthetic methods to form complex shapes illustrates the versatility of ssDNA as a template. An important aspect for all of these structures is that the construction processes involves the direct binding of metal ions such as Ag^+ to the DNA scaffold.

The two potential binding sites of Ag are the heterocyclic bases, Guanine, Cytosine, Adenine, and Thymine, or the negatively charged phosphodiester backbone. The negatively charged backbone seems to offer a favorable site for the binding of positively charged metal ions, and in fact divalent alkaline earth metals such as Mg^{2+} have actually been shown to bind directly to the backbone,[122] The bases offers additional binding sites as well. Studies involving transition metals show almost no interaction with the backbone phosphate groups but significant interaction with the bases.[122-124] Comparison of the Raman bands specific for the bases and for the backbone of naked DNA with various interacting metals reveals the predominance for transition metals to interact with the nucleotide bases.[122] These results were substantiated by absorption studies of similar systems that showed peaks corresponding to backbone absorption were

not perturbed with the addition of Ag ions, while those specific to the bases were significantly altered.[124]

Specific interactions of oligonucleotides with fluorescent Ag nanoclusters have been studied by Petty and coworkers to determine the origin of binding of the cluster to the DNA scaffolds.[125] The formation of fluorescent clusters was found to be highly dependent on the pH of the solution relative to the pKa of the N3 of both cytosine and thymine. The fluorescent species could only be formed once the pH of the solution exceeded the pKa, suggesting that the N3 position is instrumental in the binding of fully reduced Ag nanocluster. Thus, the base sequence as well as the pH of the solution could potentially be used to control the scaffold-Ag interaction such that specific nanocluster formation can be controlled.

Ag nanocluster excited state interactions with the DNA have proven to be important as well. Transient absorption studies of a series of fluorescent Ag nanoclusters all in scaffolds consisting of different base sequences yielded remarkably similar results. In each case a transient species existed in the microsecond time regime with an absorption peak near 700 nm.[126] These studies suggest that the origin of this state is the same in all the species studied and the likely cause of the microsecond intermittency observed in single molecules of Ag nanoclusters.[83] The transient absorption spectra were very similar to that of anionic cytosine resulting from charge injection. These similarities led Patel and coworkers to assign the origin of the fluorescence intermittency seen in Ag nanocluster emission to a charge transfer process involving the DNA.[126] The preponderance of data shows that both Ag ions and clusters interact mainly with the heterocyclic bases. While synthetic techniques in most cases are

quite simple, the ongoing interaction of the cluster with the oligonucleotide appears to be more complex, influencing Ag nanocluster photophysical properties.

1.8 Signal Extraction

Recent attempts to increase fluorophore brightness, through the development of new fluorescent labels such as quantum dots, have resulted in minimal gains in true sensitivity. The suppression of background fluorescence using near infrared emitting dyes, total internal reflection excitation, and multiphoton excitation are moderately more successful in the generation of less background, but they fail to actively separate the background fluorescence from the label emission. Cellular autofluorescence is still significant enough even at moderate excitation intensities that it can obscure both bulk and single molecule signals. Improvements beyond simply developing brighter dyes are needed. Decoupling a specific signal from the background via differences in the photophysical behavior should facilitate the use of signal processing techniques to drastically improve sensitivity through specific signal extraction. This can be accomplished by selectively imposing a specific modulation frequency onto the emission signal without affecting the background.

While rather simple conceptually, implementation with fluorescence is technically challenging. Direct excitation of a fluorophore also simultaneously excites any background fluorescence. An increase in excitation intensity results in both brighter label emission and background emission, therefore modulation of the excitation source would simultaneously modulate both as well. Only a process that acts solely on the fluorescent signal, such that it can be excited out of phase from the background, would allow for the use of modulation based signal extraction in biological imaging. Similar types of signal

processing are widely employed in science and medicine including applications such as magnetic resonance imaging[127] and absorption spectroscopy.[128] Signal processing often relies on the manipulation of a sensory signal with a specific frequency component and subsequently the selective extraction of the specifically imposed frequency.[129] Through these methods an additive signal of many components can be decomposed into the individual components. In the case of fluorescence imaging, two major components combine to make up the observed signal- probe fluorescence and background light. Coupled with external factors, these also contribute to signal noise. While there are many forms of signal decomposition, one of the most widely utilized is Fourier decomposition. Where for a given time series, f(t), the Fourier transform in order to project the time domain onto the frequency domain is

$$F(v) = \int_{-\infty}^{\infty} f(t) e^{2\pi i v t} dt \qquad \text{Equation 1.4}$$

Encoding an external periodic waveform onto the fluorescence signal would allow for its specific extraction via Fourier analysis of the resulting time based signal. The unmodulated background would be observed in the zero frequency component, and the target signal would be shifted out to the modulation frequency, decoupling it from the background. In this work I will show that Ag nanoclusters exhibit unique photophysics allowing the modulation of their fluorescence without any effect on the background signal.

1.9 Fluorescence Energy Transfer

Fluorescence Resonance Energy Transfer (FRET) has become an important technique in biological imaging, primarily in distinguishing the proximity of two separately labeled components.[130-133] Energy transfer takes place between a donor fluorophore and an acceptor fluorophore via a non-radiative dipole-dipole interaction. The rate and therefore the extent of energy transfer is governed by a number of factors, including the spectral overlap between the FRET pair, the quantum yield of the fluorophores, and the distance between the FRET pair. This extremely sensitive distance dependence can be used as a molecular ruler where distances between appropriately labeled macromolecules can be estimated based simply on the rate of energy transfer (k_{et}).[46] The rate of energy transfer, k_{et} is denoted as

$$k_{et} = \frac{1}{\tau_d} \left(\frac{R_0}{r}\right)^6$$

where τ_d is the lifetime of the donor in the absence of the acceptor, R_0 is the Forster radius, and r is the distance between the donor and acceptor. The Forster radius is defined as the distance at which the energy transfer efficiency is equal 50%. k_{et} can be defined more explicitly defined as

$$\kappa_{et} = \frac{Q_d \kappa^2}{\tau_d r^6} \frac{9000(ln10)}{128\pi N \eta^4} J(\lambda)$$

where Q_d is the quantum yield of the donor, κ_2 is the relative orientation of the dipoles, η is the refractive index of the solution, and $J(\lambda)$ is the spectral overlap in terms of the normalized emission at the acceptor absorption wavelength and the extinction coefficient of the acceptor at the same wavelength.[46,134] The energy transfer rate can be represented in many forms

$$E = \frac{{R_0}^6}{{R_0}^6 + r^6} \quad or \quad 1 - \frac{\tau_{da}}{\tau_d} \; or \; \; 1 - \frac{F_{da}}{F_d}$$

where F_{da} and F_d are the integrated fluorescence of the donor in the presence of the acceptor and the absence of the acceptor, respectively. Correspondingly, direct measurements of the quantum yield or the lifetime of the donor can be used to calculate the distance between the donor and acceptor.

Energy transfer is dependent on a donor in the excited state residing in close proximity to an acceptor with suitable spectral overlap. The presence of the acceptor opens a competing pathway for relaxation of the excited donor, reducing the probability of donor emission. The result is a lower donor quantum yield. When the acceptor is already in the excited state, the pathway for energy transfer is blocked, increasing the probability of donor emission. For example, if the fluorescence lifetime of the acceptor is significantly longer than the donor, a pile up effect can occur where energy transfer is inhibited and the donor emits for several excitation cycles while waiting for decay of the acceptor. Alternatively, energy transfer can be blocked by direct excitation of the acceptor in a process referred to as frustrated fret.[134-137] The result is a decrease in the FRET efficiency and an increase in the effective quantum yield of the donor, leading to

higher donor emission. In this way, the FRET process is analogous to that shown earlier for fluorescence intermittency. Directly exciting the acceptor with a secondary laser leads to an increase in the donor quantum yield in much the same way as depopulation of the dark state. The similar nature of these processes suggests that it may be feasible to use both dark state depopulation and frustrated FRET as way of modulating fluorescence for optical signal extraction.

CHAPTER 2
EXPERIMENTAL SECTION

2.1 Ag Nanocluster Synthesis

Ag nanoclusters examined in this work were all encapsulated in oligonucleotide scaffolds. The formation of specific Ag nanocluster species, as determined by emission wavelength, was highly reliant on the scaffold base sequence. The identification and characterization of this oligonucleotide sequence specificity will be discussed at length and is one focus of this work. Single stranded deoxyribonucleic acid (ssDNA) was purchased from Integrated DNA Technologies (IDT) typically in 1 μmole quantities and received in solid form. After standard desalting by the supplier, the actual yield received ranged from 200-800 nanomoles. This solid was dissolved in 1 mL of deionized water (18.2 MΩ) without further purification yielding a stock solution of oligonucleotide for additional experiments. The appropriate volume of this stock solution was used to create a final concentration of 50 μM of the oligonucleotide in 1 mL of the final solution. After further dilution with the required amount of deionized water necessary to reach the 1 mL final volume, $AgNO_3$ (Sigma-Aldrich, 99.9999%) was added at a molar ratio ranging from 4:1 to 7:1 to that of the oligonucleotide with the exact ratio depending on the target cluster. This solution was allowed to rest at room temperature for 10 minutes before the addition of a strong reducing agent, $NaBH_4$ (Aldrich 98%), of either 1:2 or 1:1 molar ratio to the Ag ions, again with the ratios varying with the nanocluster species. For all species, within a few minutes of the addition of the reducing agent the final solution would turn a bright yellow. This solution was kept at room temperature for approximately 2 hours at

which point fluorescence was typically observed. Samples were stored at 4º C to prolong shelf life and stability. Specific details on the oligonucleotide sequences and reactant ratios for all Ag nanocluster species are shown in table 3.1 and discussed at length in chapter 3.

Oligonucleotides functionalized, at either the 5' or the 3' end, with various organic dyes, including cy5, cy3 and texas red, were purchased from IDT after HPLC purification. The yield for 1 μmole of these samples was typically less than 100 nanomoles due to the higher level of purification. Additional oligonucleotide scaffolds functionalized with biotin were also purchased from IDT. Biotinylation was carried out at IDT and was available as 5', 3', or internal modification. Biotinylation was available directly attached to the scaffold or with an intermediate triethylene glycol spacer. Synthesis of Ag nanoclusters in biotinylated oligonucleotides was done with the same ratio of reactants as detailed for the naked DNA scaffold. These scaffolds, however, required a well regulated pH in order to maintain spectral purity and high creation efficiency. The ph dependence varied for each scaffold and is discussed in chapter 3.

2.2 Microarray and Plate Reader Analysis

DNA microarrays (Combimatrix) were used for the high throughput screening of oligonucleotide strands targeting those that selectively encapsulate specific species of Ag nanoclusters. Each array is comprised of four separate blocks containing 2240 spatially defined wells, which are 40 micrometers in diameter. Each well can be individually programmed based on oligonucleotide length and base sequence. DNA sequences are synthesized on a semiconductor chip built into the array surface via electrochemistry and

are anchored via the 3' end of the strand. All four array blocks contain the same sequences, allowing for redundancy and varying experimental parameters. Solution based synthesis is achieved by using a capping mechanism mounted to the array, creating a 30 μL reaction chamber over each block. This allows complete and independent control over synthesis conditions for each of the separate blocks. Ag ions are introduced by adding 30 μL of a 35 μM solution of $AgNO_3$ to the microchamber. This solution is allowed to react with the microarray for 30 minutes to give adequate time for the binding of the ions with the scaffold. The entire solution containing the Ag ions is then removed. The microchamber is then rinsed thoroughly with deionized water to remove any free ions not bound to the DNA on the microarray surface. Mimicking the conditions for typical synthesis of Ag nanoclusters in solution, this is followed by addition of 30 μL of a 35 μM solution of NABH4 to reduce the bound Ag ions. After sitting for 30 minutes, the solutions is removed and thoroughly rinsed again. The chamber is then filled with deionized water and left at room temperature for 2 hours at which point Ag nanoclusters have been formed within the microarray wells. To insure long term stability the array is stored at 4º C.

Imaging of arrays is performed at multiple excitation wavelengths with a goal of identifying perspective oligonucleotides that specifically encapsulate an individual fluorescent Ag nanocluster species. Monitoring the relative brightness of the emission across the entire array at a given excitation wavelength identifies the sequences that have the highest creation efficiency. At the same time excitation specificity is determined by identifying these same bright wells that also give emission from only one excitation wavelength and are dark or give little emission from all other excitation wavelengths.

Bright emission and spectral purity are used as screening criteria for sequence selection. This process eliminates strands with low creation efficiency and those that form more than one type of fluorescent Ag nanocluster. Using a high collection efficiency macroscope (MVX10 Olympus) with a 2x objective (na .5), arrays are mounted on a joystick controlled stage (Applied Scientific Inst MS-2000). Each block is then separately illuminated and imaged. Mercury lamp excitation is filtered for appropriate wavelength using a 25 mm bandpass filter accompanied by a corresponding dichroic mirror. The resulting emission is directed back through the dichroic mirror and an additional band pass filter, which is red shifted from the excitation wavelength. The fluorescence is then projected onto a CCD camera (Andor IXON). Separate images of each block are recorded for each of the various excitation wavelengths and then stored for comparison. Images are analyzed using Combimatrix MicroArray Imager 5.9.3 software, which extracts data for each spot by overlaying a grid on the image and compiling the brightness for each well. After analysis, the 5-10 strands that show the most promising combination of brightness and spectral purity for each excitation wavelength are then scaled up to higher volume synthesis. Strands for each excitation wavelength correspond to separate Ag nanocluster species.

While array studies nicely produce potential sequences, they lack well defined reactant ratios as the exact concentration of the oligonucleotides are unknown. In order to determine the optimum conditions for Ag nanocluster, oligonucleotides were synthesized with varying ratios of $AgNO_3$ and $NaBH_4$. Plate reader analysis allows for the simultaneous optimization of several synthetic parameters. This was particularly useful in the determination of the ratios of the various reactants. Utilizing a 384 well plate

with 100 uL wells, solutions, of each strand identified from the arrays, were tested by varying the ratio of the Ag:BH_4 and Ag:DNA. Each well contained 80 μL of 50 μM DNA and the ratio of Ag to DNA was varied from 1:1 to 8:1 for successive wells. For each of these ratios 5 separate wells were prepared using different BH_4 ratios while maintaining all other parameters. The Ag to BH_4 ratios were set at 1:1, 2:1, 3:1, 4:1, and 1:2. The reactants were mixed in the same sequence and timing as described for typical synthesis. The plates were scanned at multiple wavelengths, using a Spectramax M2 well plate reader. The resulting fluorescence was then compared across all wells to first determine if the scaffold still exclusively formed the cluster of interest and then to determine the ratios that resulted in the brightest emission. Once the optimum conditions had been determined, synthesis was scaled up to higher volumes, allowing for photophysical characterization.

2.3 Ensemble Photophysical Characterization

Ensemble fluorescence and absorption measurements were necessary to characterize extinction coefficients and quantum yields. Fluorescence measurements were performed with a Photon Technology International (PTI) Quanta Master 40 which is equipped with a xenon arc lamp as an excitation source and a photomultiplier tube sensitive to 900 nm as a detector. Concurrent absorption measurements were taken with a Shimadzu UV-2401 PC spectrophotometer. In all cases data was collected from samples in either a glass or quartz cuvette. Additional measurements to determine fluorescent lifetimes were performed with an Edinburgh Instruments Lifespec-ps system equipped with a Hamamatsu multi-channel photomultiplier tube detector. The excitation sources for

lifetime measurements were Picoquant laser diode heads, of varying wavelengths, controlled by either a PDL 800-B or Sepia II laser driver system from Picoquant.

2.4 Fluorescence Microscopy

All fluorescence based microscopy experiments were performed on Olympus IX-70 or IX-71 inverted microscopes. Excitation sources, both lasers and mercury lamps, were coupled through the back microscope port. Excitation light was directed toward the sample using a dichroic mirror that was selected to have near complete reflectance of the excitation light. Solution based samples utilized a water immersion objective (60x, na 1.20), while an oil immersion objective (60x, na 1.45) was used for surface based samples. In both cases the objective was used to focus the excitation light onto the sample. Emission from the sample was collected with the same objective and typically directed to either a trinocular or the side port of the microscope. Typical samples, both solution and surface based, were prepared on 22.5 mm x 22.5 mm glass coverslips (Fisher) with a thickness of .15 mm. Prior to use coverslips were cleaned via a three step process. Initially, coverslips were immersed in .05 M NaOH for 1 hour while sonicating. After thorough rinsing with deionized water, the coverslips were then sonicated in water for an additional hour. This was followed by an additional hour of sonication in acetone after which the coverslips were dried under vacuum.

2.5 Time Correlated Single Photon Counting

Time Correlated Single Photon Counting (TCSPC) involves recording the timing of individual photons with high resolution, which is the basis for most time based

techniques including many single molecule methods. This is typically accomplished by the detection of photons, with a detector capable of fast time response, usually with either an avalanche photodiode or photo multiplier tube. Upon incidence of the photon on the detector, an electronic signal is generated and sent to a photon counting module (Becker Hickl SP630 or Time Harp) which uses an external sync source as a mechanism to time stamp individual photons.[138] Working in "reverse start/stop mode" where the start signal is initiated by the incident photon and the stop signal is from the next sync pulse a histogram can be built up of the timing between the sync and the photon (microtime) with resolution on a ps time scale. Simultaneously, the photon timing from the beginning of the experimental data set is recorded giving rise to a time trace where each photon is stamped with the total elapsed experimental time (macrotime). The timing resolution is not based on the detector pulse width but rather tied to the electronics of the detector and the photon counting module, resulting in much more reliable and better resolved experimental timing.

2.6 Fluorescence Correlation Spectroscopy

Fluorescence Correlation Spectroscopy (FCS) is a solution based microscopy technique that can be used to determine several physical characteristics of both individual fluorophores and labeled macromolecules such as diffusion constants, fluorophore brightness, blinking dynamics, and hydrodynamic radii. Using a typical microscopy set up as described above, a continuous wave laser is used as an excitation source by tightly focusing the laser several microns into solution such that a small fixed focal volume is established.[80,139,140] A diagram of a typical set up for FCS is illustrated in figure 2.1.

Using an extremely dilute solution (pM-nM) allows for the restriction of 1 to a few molecules occupying the focal volume at one time. Molecules are continuously diffusing in and out of the laser focus resulting in fluctuations in the measured fluorescence that are tied to the time for the molecules to transit through the three dimensional focal volume. The fluorescence is detected by directing the emission from the sample through an filter to block the laser light and then through a pinhole to reject out of focus emission and is detected with an avalanche photodiode. The resulting time versus fluorescence intensity data trace is then processed via autocorrelation allowing the determination of both diffusion times and faster time scale blinking dynamics. Similar to FCS, correlation analysis performed on immobilized molecules was done in near identical experimental setup except the laser was focused onto the polymer-immobilized fluorophores rather than into solution. In the absence of diffusion, fluctuations in the intensity result strictly from fluorescence intermittency.

2.7 Surface Bound Molecules

Photophysical characterization of immobilized molecules requires them to be fixed under steady illumination rather than transiently entering and exiting the focal volume as in FCS. In vitro measurements in aqueous conditions were achieved by immobilizing individual species of Ag nanoclusters to the surface of a coverslip via Avidin-Biotin chemistry. Cleaned coverslips were immersed in a mixture of [3-(2-Aminoethylamino)propyl]trimethoxysilane in acetone(3mL/ 100 mL) for 1 hr which

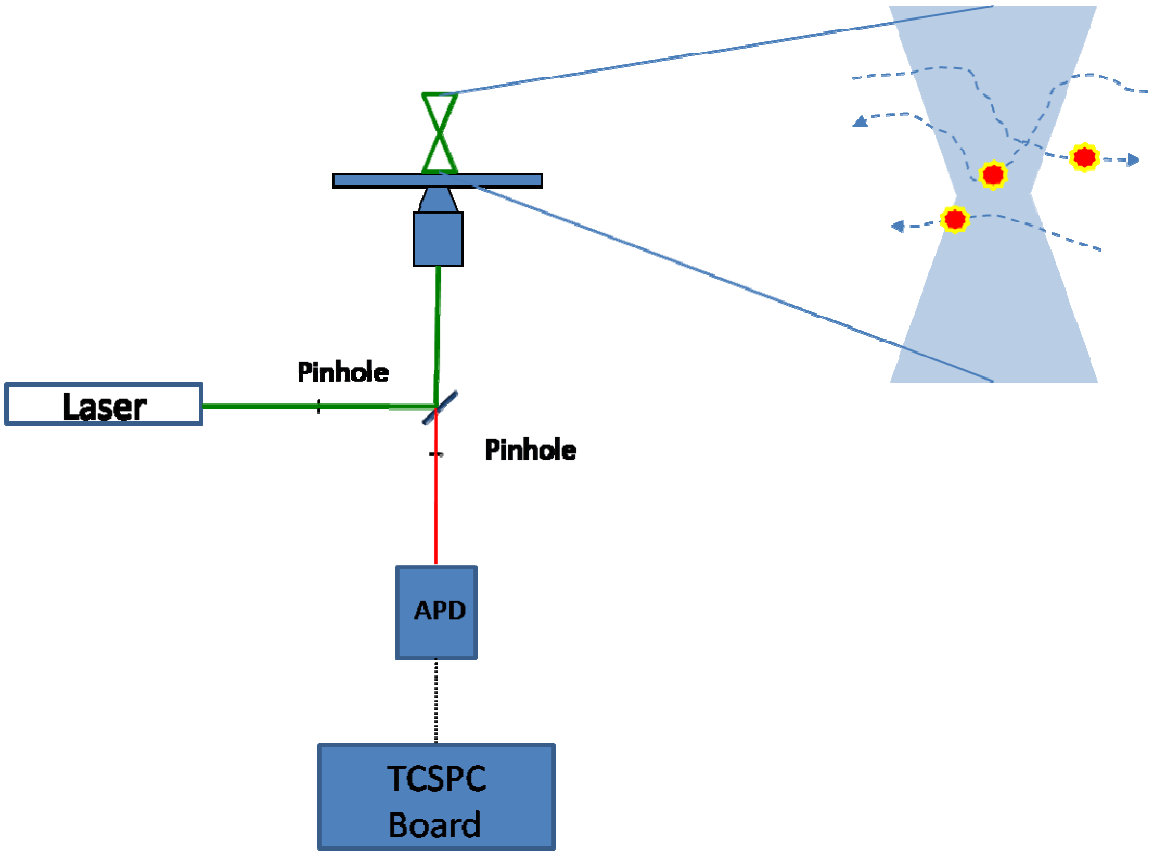

Figure 2.1. Diagram of Fluorescence Correlation Spectroscopy (FCS) experimental set up. Laser excitation is directed through the objective and focused 30 μm into the dilute sample, and the emission is directed back through the objective and through the pinhole to reject out of focus emission. The emission light is passed through a bandpass filter centered at the emission wavelength and set to block all laser light. Photons are detected at the apd and the resulting signal is sent to the photon counting board for analysis.

resulted in the functionalization of the surface with primary amines. A biotinylated polyethylene glycol (PEG) NHS ester (Pierce) which is highly amine reactive was then attached to the surface leaving exposed biotin. This was accomplished by sandwiching 2 amine functionalized coverslips around 40 μL of the biotinylated PEG-NHS ester (~50 μM) and allowed to react for 15 min before being rinsed thoroughly with deionized water. Avidin (50 μM Pierce) was then added to the coverslip with the same sandwich technique described for biotin. This was allowed to react for 10 min before rinsing several times. The now Avidin-modified coverslip was used to immobilize Ag nanoclusters encapsulated in biotinylated DNA scaffolds. After synthesis, 50 μL of the fluorescent species of interest was added to the coverslip using the sandwich technique in order to bind the molecules to the surface. Subsequent imaging and data collection of the sample was done under solution by adding 50 μL of water or buffer to the top of coverslip when mounted on the microscope.

2.8 Optical Enhancement of Ag nanolcusters

Dual laser excitation was used to optically depopulate dark states of both Ag nanoclusters and organic dye systems. Measurements required the spatial overlap of multiple laser beams for continuous wave excitation and temporal as well as spatial overlap in the case of pulsed excitation. Using a microscopy set up as described previously, primary laser excitation light was routed to the back of the microscope and through a dichroic mirror sitting just at the exterior of the scope. Simultaneously, a secondary laser, at lower energy than the emission of the fluorophore, was routed such that it reflected off the external dichroic mirror resulting in a spatial combination of the two different excitation

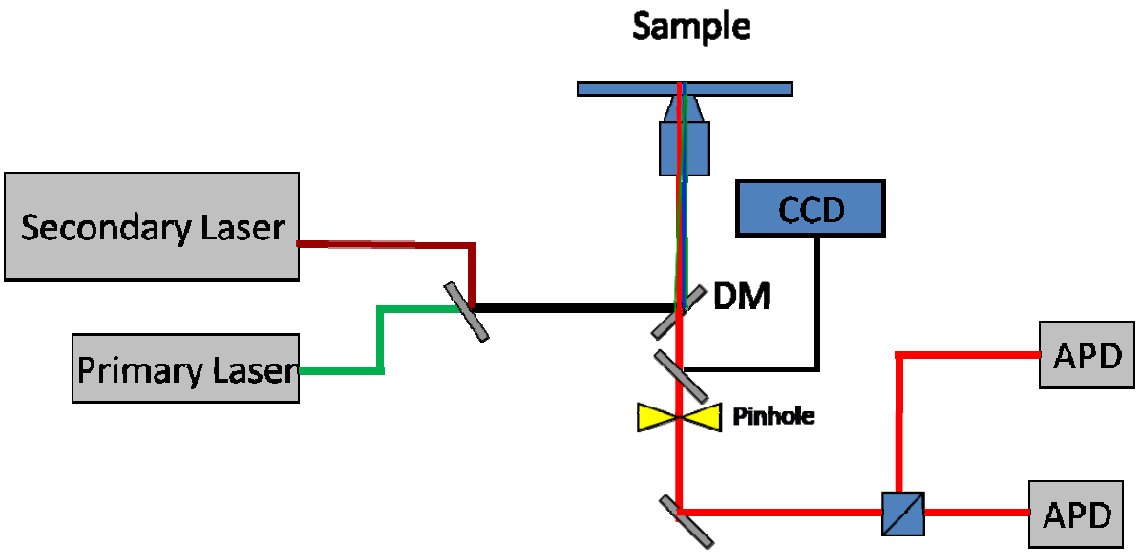

Figure 2.2. Diagram of experimental set up used for photobrightening of Ag nanoclusters. Primary and secondary lasers are overlapped by combining them with a dichroic mirror. The excitation is then directed through the objective and focused on the sample while the emission is directed back through the objective and through the pinhole to reject out of focus emission. The emission light is passed through a bandpass filter centered at the emission wavelength and set to block both the primary and secondary excitation light. Emission can alternately be directed to either a CCD camera or to either one or two apd's.

sources. A schematic of the experimental setup is detailed in Figure 2.2. In all cases the combining dichroic used was designed to pass the shorter wavelength laser while reflecting the longer wavelength secondary laser. A bandpass dichroic was used in the microscope reflecting both excitation wavelengths while transmitting flurophore emission. A variety of laser wavelengths were used as primary and secondary excitation sources including helium neon single line lasers (Spectra Physics and JDS Uniphase), tunable Argon/Krypton air-cooled lasers (Melles-Griot), and tunable Ti-sapphire (Coherent). The collection of the emission with one or two laser excitation was then done with either a CCD or a single photon counting detector (APD, Perkin-Elmer; PMT, Hamamatzu).

2.9 Single Molecule Identification

Characterization of single molecule photophysics requires high sensitivity detection, where single molecule signals can be distinguished from bulk fluorescence. Several techniques have been developed to identify single molecule behavior- dipole emission patterns, single step photobleaching, blinking behavior, and photon antibunching. Perhaps the most direct means of verifying single molecule emission is single step photobleaching. Single molecules exhibit an emission rate that fluctuates slightly, well above the background, until photobleaching causes the signal drops to drop to the background level without any intermediate steps. As multiple molecules are unlikely to transition into a permanent dark state simultaneously, single step bleaching is a strong indication of single molecule behavior. Experimentally this is readily achieved in a typical confocal microscopy set up using single photon counting techniques.

An alternative verification process of single molecule behavior relies on CCD imaging. As fluorescence is dipolar in nature, images of the resulting emission exhibit a specific pattern depending on the orientation of the molecule.[141-143] Dipole emission patterns are imaged by slightly defocusing an in focus molecule and acquiring an image with a CCD with a high numerical aperture (1.40) 100x objective and an additional 1.5x magnification. While this is indicative of single molecule behavior, imaging emission patterns can be technically challenging, as they require ideal imaging conditions. Single molecule behavior can also be established through photon antibunching.[144] Once promoted to an excited state, a molecule remains there until it either emits a photon or relaxes through a radiationless pathway. Thus, a single molecule can only emit one photon at a time and must go through an additional absorption and emission cycle to emit a subsequent photon. The probability of detecting two photons simultaneously is than near zero. With sufficient timing resolution, such that photons are tagged faster than the intrinsic lifetime of the excited state, this process can readily be observed. The emission signal from a single molecule is split into two separate signals via a beam-splitter and directed to different detectors. Cross correlation of the two signals will show anticorrelated behavior at zero time delay. Ideally the correlation goes to zero indicating that no photons arrived simultaneously at the separate detectors.

2.10 Modulation Experiments

The ability to impose an externally generated waveform onto the fluorescent signal is the primary criteria for using the optical enhancement of emission to generate greater

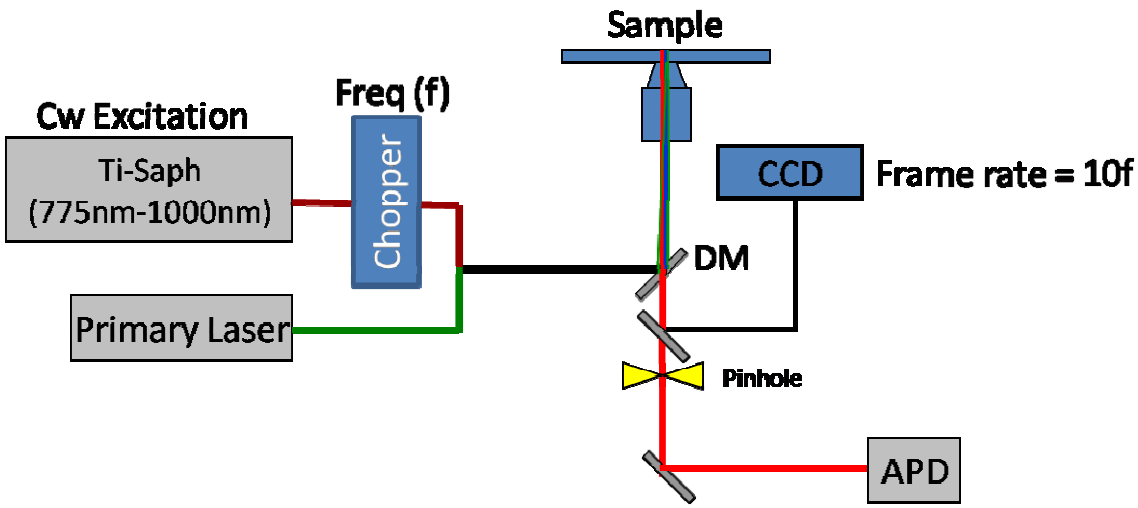

Figure 2.3. Diagram of experimental set up used for modulation of secondary laser used to impose a periodic waveform on the fluorescence signal. The secondary laser is directed either through a mechanical shutter or a chopper that can modulate the laser from 2 to 4000 Hz. Primary and secondary lasers are overlapped by combining them with a dichroic mirror. The excitation is then directed through the objective and focused on the sample while the emission is directed back through the objective and through the pinhole to reject out of focus emission. The emission light is passed through a bandpass filter centered at the emission wavelength and set to block both the primary and secondary excitation light. Emission can alternately be directed to either a CCD camera or an apd.

sensitivity. Using a typical confocal microscopy configuration samples are exposed to both a primary and a modulated secondary laser (Figure 2.3). Synchronously applied secondary laser excitation leads to modulated fluorophore brightening via a shortening of the off time. The primary laser is directed into the back port of the microscope after passing through a combining dichroic mirror. The secondary laser, at lower energy then the fluorophore emission is directed in an alternate path and is reflected off the same dichroic mirror. A variable mechanical chopper with a maximum frequency of 4000 Hz was placed in the secondary laser excitation path in order modulate the secondary laser exposure. The waveform of the modulated laser is directly imprinted onto the fluorescent signal via dynamic photobrightening in phase with the modulated laser. Frame rates using CCD detection were set at 10 times the frequency of modulation. For all species of Ag nanoclusters and organic fluorophores all secondary excitation wavelengths were > 750 nm (either Ti-sapphire Coherent or KMlabs). A time trace for each pixel was then constructed from the resulting image series. The amplitude at the modulation frequency from the Fourier transform of each time trace was then plotted to reconstruct a demodulated image.

A very similar set up as indicated in figure 2.3 was utilized for enhancement of FRET based systems. Pulsed donor and acceptor excitation requires spatial and temporal laser alignment (Figure 2.4). In order to control the timing of the pulses, a secondary laser (typically Ti-sapphire) was used to trigger the primary laser. The secondary laser is routed through a pulse picker (Con Optics) which is used to reduce the repetition rate to match the capacity (<40 MHz) of other available pulsed laser sources. The sync signal out of the pulse picker is then routed through a delay generator (DG645 Stanford

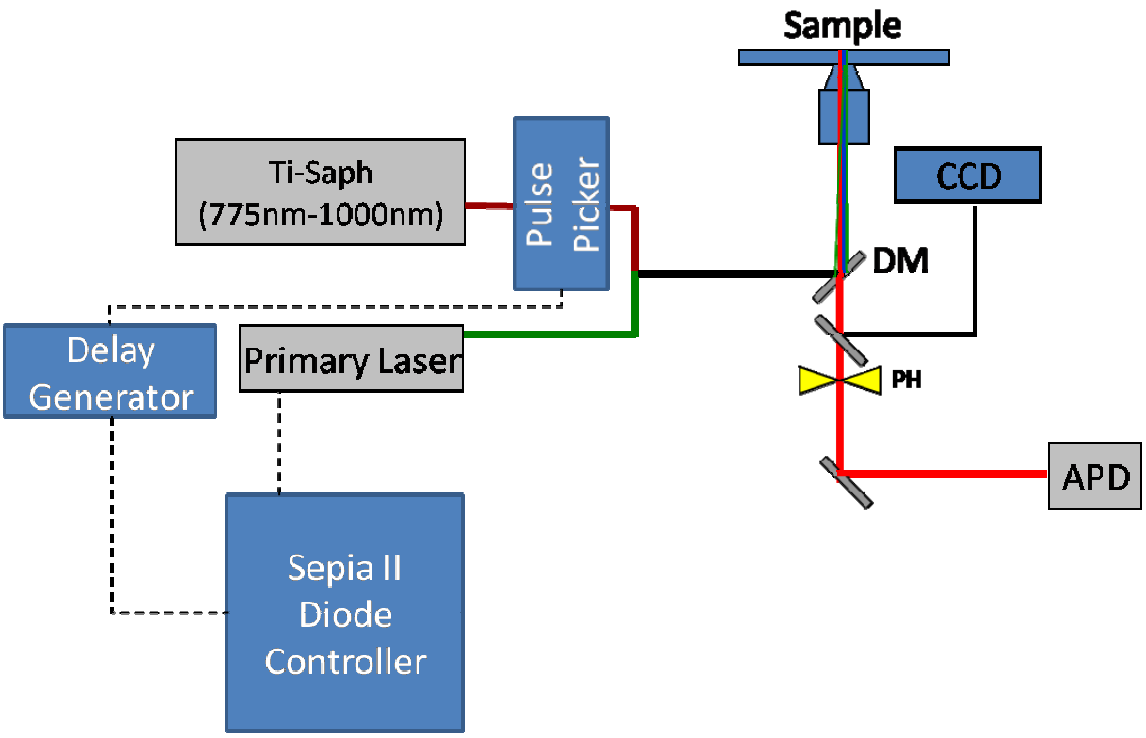

Figure 2.4. Diagram of experimental set up used for simultaneous donor and acceptor pulsed excitation designed to block energy transfer. The secondary laser (ti-saph mira 80 MHz) is directed through a pulse picker (conoptics) to reduce the repetition rate (<40 MHz). The sync signal from the pulse picker is routed through a delay generator and then used to trigger the secondary laser. The delay generator was used to delay the sync signal so as to temporally overlap the pulses from the two lasers. The excitation of both lasers is directed through the objective and focused on the sample while the emission is directed back through the objective and through the pinhole to reject out of focus emission. Donor emission light is passed through a bandpass filter centered at the emission wavelength and set to block the primary laser, secondary laser, and the acceptor emission. Emission can alternately be directed to either a CCD camera or an apd.
interpulse gap.

Instruments) with up to 8 MHz capability. The output from this unit triggered the primary laser diode controller (Picoquant Sepia II). The different path lengths and electronic triggering mechanisms result in the respective laser pulses having a large The DG645 delay generator has picosecond resolution which can be used to shift the diode laser signal (100 ps pulse width) to overlap with the Ti-sapphire secondary pulse (~200 fs). This results in both temporal and spatial overlap of primary and secondary lasers.

CHAPTER 3
Ag NANOCLUSTER SYNTHESIS & PHOTOPHYSICS

3.1 Introduction

While silver nanoclusters have long been known to exhibit bright fluorescence in rare gas matrices[94,95,145] and solid substrates,[146-148] initial attempts to harness their fluorescent properties did so in rigid environments not suitable for biological imaging. The recent use of oligonucleotides as an alternative scaffold[107,108,125,149] stemmed from a push to create these fluorophores in a biocompatible and functional form. Naturally part of the genetic process, DNA is inherently biocompatible and has been shown to effectively bind Ag ions.[122,124] Giving rise to a versatile templating effect, ssDNA and dsDNA have been used as scaffolds for a variety of metal based structures.[114,117,150,151] Initial studies of oligonucleotide encapsulated fluorescent Ag nanoclusters, however, focused primarily on poly-cytosine scaffolds[108] with the resulting fluorescent species exhibiting bright emission, relatively high quantum yields (~30%), and large extinction coefficients (>250,000 M^{-1} cm^{-1}).[83] Figure 3.1 shows the typical fluorescence for Ag nanoclusters encapsulated in 8-mer poly-cytosine where several species are formed with emission across the visible and into the near infrared. The resulting heterogeneity, with several similarly emitting species formed simultendously, makes photophysical characterization difficult as the spectral overlap interferes with clean absorption and fluorescence signals. Conjugation to biological systems would also be difficult as the functionalized scaffold

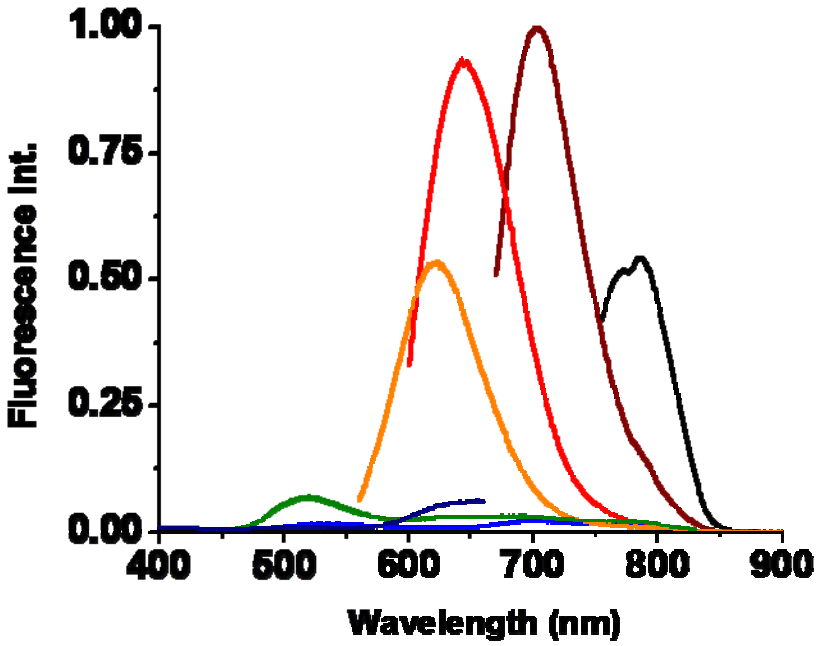

Figure 3.1. Typical fluorescence from Ag nanoclusters encapsulated in poly-cytosine oligonucleotides showing multiple bright fluorescent species and absolutely no specificity for any individual species.

would not be specific for a single fluorescent species, resulting in low yields of target nanocluster attachment.

A variety of methods have been used in an attempt to improve spectral purity including varying scaffold size, solution ionic strength, and trial and error base replacement by randomly interchanging adenine; guanine; or thymine for cytosine. While all of these methods resulted in a modification of spectral properties, few yielded spectrally pure solutions. For example, 12-mer poly-cytosine scaffolds were found to transiently form a single near infrared emitting species upon dissolution in phosphate buffered saline (PBS).[83] Unfortunately, under these conditions this species survived for only a short time (<24 hrs). More recent studies have focused on the use of hairpin forming oligonucleotides for Ag nanocluster synthesis but still with a trial and error approach to base sequence.[110,152] Oligonucleotide sequences are naturally programmable, simply through interchanging the 4 natural bases and varying the strand length. If fact, even a relatively short 12-mer oligonucleotide leads to 4^{12} possible sequence combinations. Clearly a high throughput method of screening DNA sequences is necessary for identification of optimum scaffold sequences.

3.2 Scaffold Screening with DNA Microarrays

Combimatrix microarrays consist of 2240 sequences that are synthesized by attachment of the 3' end of oligonucleotide to the array surface in separate 40 micron wells. All the sequences on an individual array can be investigated simultaneously to facilitate high throughput screening applications. Building on previous studies that showed the importance of cytosine in nanocluster formation, initial 12-mer arrays were programmed

such that the first 3 bases on the 5' end and the last 4 bases on the 3' were restricted to cytosine. The remaining 5 bases in the center of the oligonucleotide were composed of various combinations of adenine, thymine and cytosine. Guanine was excluded from initial studies due to its propensity to form quadruplex structures[153] which could interfere with the formation of the Ag nanocluster-DNA structure. While ideally scaffold length is minimized to reduce the overall fluorophore size, Combimatrix array synthesis is optimized for 24-mer and longer strands. To improve array quality, a 12-mer thymine spacer was incorporated on the 3' end. The resulting target DNA sequences were then of the form **5'-CCCXXXXXCCCC-3'**, yet on the array were attached as (**5'-CCC XXXXXCCCCTTTTTTTTTTTT-3')** due to the additional spacer.

As the reaction vessel is only 30 μL and the oligonucleotides concentration on the array are not precisely known, the ratios of reactants is difficult to control, so various concentrations of $AgNO_3$ and $NaBH_4$ were used for initial experiments. Previous studies on poly-cytosine strands showed that incorrect reactant ratios reduced or completely eliminated the formation of the fluorescence species. This was also observed on the microarray where $AgNO_3$ concentrations of more than 100 μM resulted in almost no fluorescence, while concentrations of ~30 μM of $AgNO_3$ and ~30 μM of $NaBH_4$ yielded the brightest fluorescence and the best coverage across the array. Using an Olympus MVX-10 macroscope, arrays were excited with a mercury lamp and simultaneously imaged with a CCD (Andor Ixon). Filtering for blue (~480 nm), green (~540 nm) and red (~633 nm) excitation, each strand was analyzed to determine brightness and nanocluster spectral purity.

Figure 3.2 shows the image of an array with 633 nm excitation and 700 nm +/- 40 nm detected emission. Several spots exhibit significantly brighter emission than the average spots, indicating the formation of a species that excites in the red and emits in the near infrared. Analysis under multiple wavelengths showed that the majority of the bright spots were selectively excited by 633 nm light, exhibiting little to no fluorescence under other excitation wavelengths. Similar results were obtained for both green and blue excitation. However, a larger number of sequences (>50) exhibited bright fluorescence under both blue and green excitation, but fewer of these brighter species exhibited spectral purity, indicating the formation of multiple fluorescent species.

Selecting the ten brightest spectrally-pure sequences for each excitation wavelength, additional studies were performed to optimize cluster formation in solution. Typical syntheses for poly-cytosine encapsulated Ag nanoclusters used equal ratios of Ag^+ and BH_4^- at molar ratios of 6:1 to the oligonucleotide scaffold. The synthetic conditions of the microarray, however, are not well defined. Ag^+ and Bh_4 interactions with the surface bound oligonucleotides are not precisely known, therefor the ratio of reactants needs to be determined. Enabling high-throughput analysis, 100 μL well plates were used to determine the appropriate ratios of reactants and the optimum experimental conditions for cluster synthesis. As detailed in the experimental section, forty separate conditions with varying concentrations of Ag^+ and BH_4 were compared for each of the species identified from the array. Measuring the resulting fluorescence for the solutions yielded the optimum synthetic conditions for each Ag nanocluster species. As expected several wells exhibited little to no fluorescence. This was particularly evident for the highest ratios of BH_4 and Ag which resulted in no fluorescence for all of the strands.

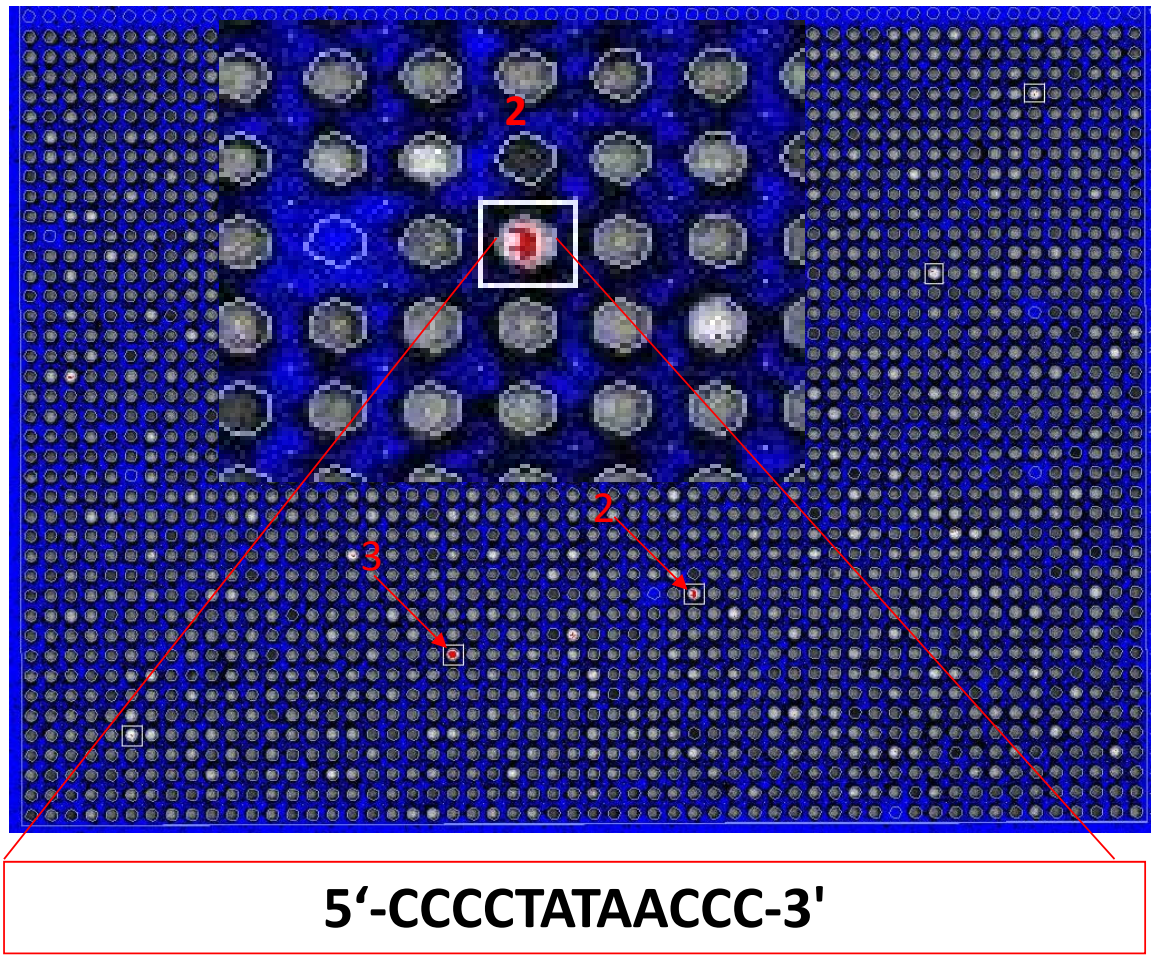

Figure 3.2. Emission from a DNA microarray excited with 633 nm light detected near 700 nm that shows several emissive sequences but 3 that are clearly much brighter than the average including the inset showing a zoomed in image of the spot labeled 2 which corresponds to the sequence 5'-CCCCTATAACCC-3'.

While optimization was successful for some strands, the majority of the sequences exhibited either very low emission or the creation of multiple fluorescent species. Of the sequences identified by the array, only ~20% showed similar excitation and emission in the plate reader studies compared to that predicted by the array. The large thymine spacer and tethering of the sequence to the array surface likely affected the conformation of the oligonucleotide, leading to disparate results in solution. Interestingly, these restrictions appear to affect some of the strands more than others.

Microarrays have not been successful, however, in optimizing conditions for all Ag nanocluster species. Poly-cytosine scaffolds, particularly 8-mer strands, show an additional fluorescent species with emission near 800 nm (Figure 3.1). Using 12-mer sequences, microarrays exhibited little to no production of this species. As the shorter 8-mer poly-cytosine strands most efficiently create this species, 8-mer microarrays were used for additional studies. Synthesis methods were identical to those described for the 12-mer arrays. Unfortunately, these arrays exhibited very little emission under 735 nm excitation. One strand (5'-CCCCAAAC-3') on the array exhibited reasonable spectral purity, though weak emission. When scaled up for solution based synthesis, this strand yielded multiple fluorescent species where the 800 nm emission was just a minor component. Array conditions likely require optimization for this species, potentially through modification of the thymine spacer and varied strand lengths, in order to identify an appropriate scaffold.

Figure 3.3 shows the spectra of four species derived from the array studies- the 600 nm emitter (Ag-600) results specifically from encapsulation in 5'-CCACCAACCACC-3', the 620 nm emitter (Ag-620) encapsulated in 5'-

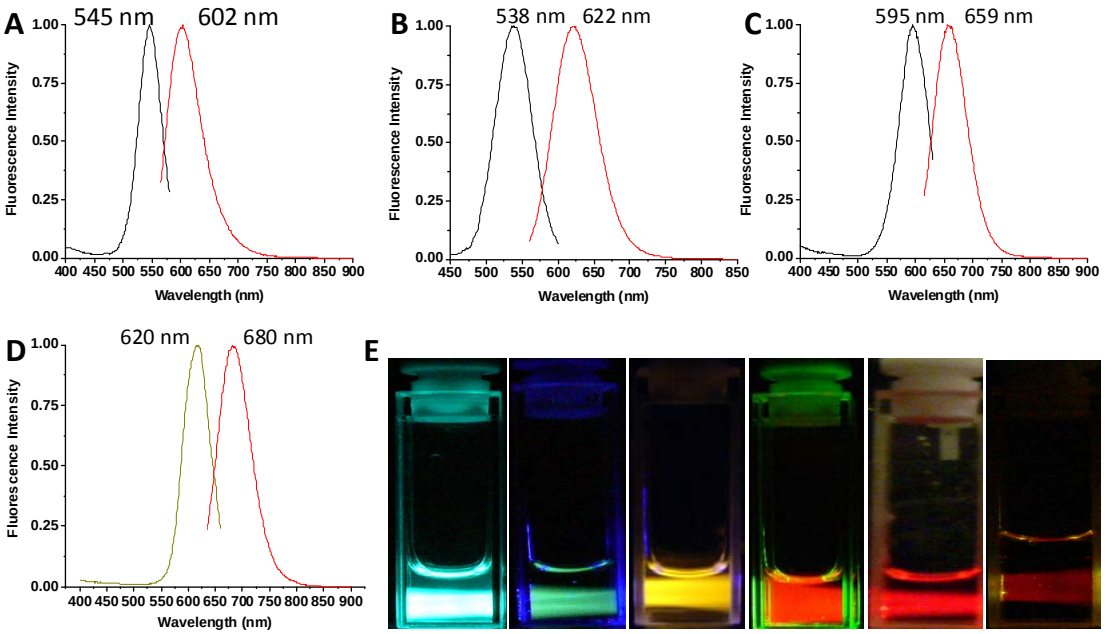

Figure 3.3. Spectrally pure emission is generated from various scaffolds resulting in several emissive species Ag-600 (A), Ag-620 (B), Ag-660 (C), and Ag-680 (D) where no other fluorescent species is present with the particular scaffold. E. Shows the emission from several species with emission ranging across the visible and into the near infrared.

Table 3.1. Shows the details on the synthesis of 4 species of Ag nanocluster identified from the microarrays including the strand sequence and the ratios of Ag and BH4 for optimum formation of each of the fluorescent species shown in figure 3.3.

Species	Ex/Em (nm)	Sequence	Ag:BH_4:DNA
Ag-600	540/600	CCACCAACCACC	6:3:1
Ag-620	540/620	CCTCCTTCCTCC	6:6:1
Ag-660	594/660	CCCATATTCCCC	5:5:1
Ag-680	620/680	CCCTATAACCCC	6:6:1

CCTCCTTCCTCC-3', the 660 nm emitter (Ag-660) encapsulated in 5'-CCCATATTCCCC-3' and the 680 nm emitter (Ag-680) encapsulated in 5'-CCCTATAACCCC-3'. Illustrating their brightness and spectral purity, images of several fluorescent Ag nanoclusters are shown separately in Figure 3.3E. While some of the sequences are quite similar, they each preferentially encapsulate completely different Ag nanocluster species. All scaffolds were optimized at ratios of Ag:DNA of 5-7:1 and BH_4 ratios ranging from 3:1 to 6:1 as specifically detailed in table 3.1. For example Ag-660 requires a specific ratio of 6:6:1 (Ag:BH4:DNA strand) in order to maximize the fluorescent component. Deviation from these values, whether in the form of too much or too little Ag or BH_4, results in a significant reduction in the yield and spectral purity of the fluorescent species. While precise synthesis was required to obtain spectrally purity, optimization of these conditions shows that an oligonucleotide template can be readily programmed for multiple emissive species.

3.3 RNA Scaffolds

Ribonucleic Acid (RNA) differs from deoxyribonucleic acid (DNA) by the presence of a 2' OH group and the replacement of thymine with uracil, which has a moderately different structure. Poly-cytosine RNA scaffolds were studied to determine if the slight backbone modification affected nanocluster formation. Under the same synthesis conditions as DNA scaffolds, 12-mer poly-cytosine RNA was found to selectively encapsulate a 650 nm emitting nanocluster. While the red emitting species was normally dominant in poly-cytosine DNA, there was typically several other species present that are not there with the RNA scaffold. Other differences were seen as well. Poly-cytosine

DNA encapsulated species are stable in solution for several days, but the RNA encapsulated species was found to be stable for several months while refrigerated at 4° C. As RNA is typically much more sensitive to the environment and degrades very easily, these results were somewhat unexpected and suggest that the presence of the nanocluster helps to protect the RNA structure. Clearly the change in the structure of the sugar backbone of the RNA from that of the DNA results in a completely different templating behavior. Ancillary to the DNA work, RNA studies suggest modification of the backbone may in fact offer an additional method to program oligonucleotides for Ag nanocluster encapsulation. This also has implications in other areas. A major challenge not addressed in this work is cellular uptake of DNA, which is challenging due to the negatively charged backbone. Future scaffolds should include noncharged backbone structures such as methylphosphonates, peptide nucleic acid, and morpholino oligonucleotides.[154] RNA studies suggest that synthesis of backbone modified oligonucleotides should be feasible with optimization of synthetic conditions.

3.4 Ensemble Photophysical Characterization

Photophysical comparisons of these newly identified Ag nanoclusters were performed against both poly-cytosine Ag nanoclusters and commonly used water soluble organic dyes. Initial studies concentrated on characterizing nanocluster brightness relative to commonly used fluorophores. Fluorescence quantum yields were determined via a comparison to known standard dyes with similar excitation and emission maxima for each of the nanocluster species. Data was collected for both absorbance and fluorescence under the same experimental conditions and equation *3.1*

$$Q_{Ag} = Q_S \frac{I_{Ag} A_S \eta_{Ag}}{I_S A_{Ag} \eta_S} \qquad \text{Equation 3.1}$$

was used to calculate the quantum yield, where I, A, and η represent the integrated fluorescence intensity, absorbance at the excitation wavelength, and the index of refraction of the solution, respectively. Comparisons between nanoclusters (subscript Ag) and standards (subscript S) were performed at various concentrations to insure accurate quantum yield calculations. Ag-620 was compared to the cyanine dye Cy3, Ag-660 was compared to Texas Red, and Ag-680 was compared to Cy5. Similar to organic fluorophores such as the cyanine dyes.[47,155] quantum yields ranged from 20 to 40% (Table 3.2).

Fluorescence correlation spectroscopy (FCS) was used to determine Ag nanocluster extinction coefficients. FCS is used to measure fluorescence intensity fluctuations which can then be correlated allowing the extraction of information about the source of the fluctuations. The most common sources of emission fluctuations are diffusion of molecules through the focal volume and blinking dynamics. A decay in the autocorrelation occurs at a time corresponding to the fluctuation events. The autocorrelation, G(t), of an intensity based time function, F(t) , is represented by equation 3.2[139]

$$G(\tau) = \frac{\langle \delta F(t) \delta F(t+\tau) \rangle}{\langle F(t) \rangle^2} \qquad Equation\ 3.2$$

where $\delta F(t) = F(t) - \langle F(t) \rangle$ is the deviation from the temporal average of the signal. Assuming a 3-dimensional Gaussian focal volume the autocorrelation can be represented as[139]

$$G(\tau) = \frac{1}{n}\left(\frac{1}{1+\frac{\tau}{\tau_D}}\right)\left(\frac{1}{1+\left(\frac{\omega_0}{\omega_z}\right)^2\left(\frac{\tau}{\tau_D}\right)}\right) \qquad \textit{Equation } 3.3$$

where n is the average number of molecules in the focal volume, τ_D is the measured diffusion time, ω_0 is the waist size defined by the boundary where the Gaussian excitation profile decays to $1/e^2$ in the x and y directions, and ω_z is the excitation decay in the z direction. At $\tau = 0$ the autocorrelation becomes G(t)= 1/n, thus the amplitude of the autocorrelation at zero lag time is the inverse of the number of molecules.

Focal volumes in FCS were determined by serial dilution of the same standard dyes used for the quantum yield measurements. By adjusting the number of molecules in the focal volume to ~1 to 2 molecules, the effective volume can then be calculated from the known diluted concentration and the average number of molecules in the solution. The Ag nanocluster solution is similarly diluted so that ~1 to 2 molecules reside in the FCS focal volume on average. In all cases, both the dyes and the nanoclusters exhibited a linear response in the measured number of molecules for each dilution. The concentration of the FCS solution is calculated from the number of molecules and the previously determined focal volume, and the original Ag nanocluster concentration is given by factoring in the dilution. The measured Ag nanocluster absorbance, A, is used to calculate the extinction coefficient, ε, with Beer's law (A=εlc) where l is the path length, and c is the concentration. Figure 3.4A shows an autocorrelation of Ag-680 with the fit indicating approximately 1 molecule on average in the focus and a diffusion time of ~ .9 ms, while 3.4B shows the autocorrelation for the standard, cy5. The values derived for Ag-620, Ag-660, and Ag-680 were 120,000 L/mol·cm, 350,000 L/mol·cm, and 125,000 L/mol·cm, respectively and are shown, along with other photophysical

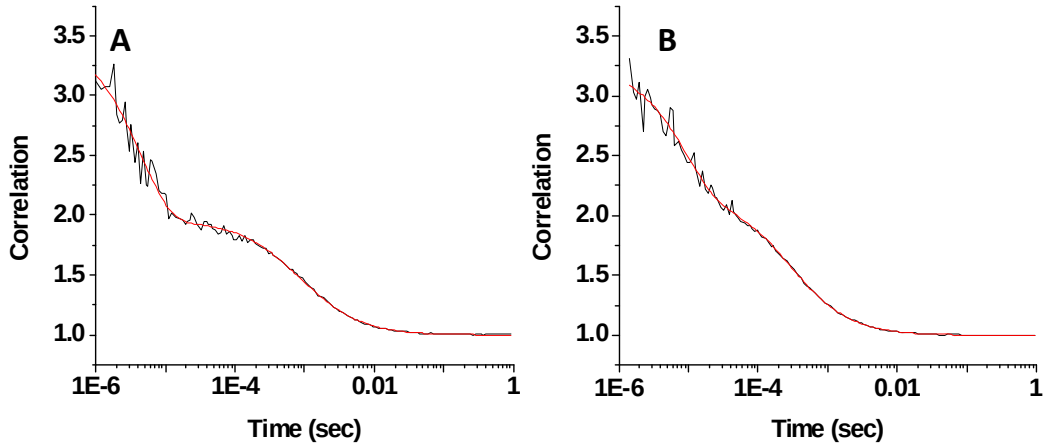

Figure 3.4. Autocorrelation from an FCS time trace under 633 nm excitation (6 kW/cm^2). A. Autocorrelation fit showing approximately 1 molecule in the focal volume with a diffusion time of .9 ms. B. Fitted autocorrelation of cy5 used as a standard showing approximately 1 molecule in the focal volume with a diffusion time of approximately 500 μs.

Table 3.2. Showing photophysical properties including excitation and emission maxima, fluorescence lifetimes, quantum yields, and extinction coefficients for species identified from array studies.

Species	**Exc/Em(nm)**	**Lifetime**	**Φ (%)**	**ε(M^{-1}·cm^{-1})**
Ag-600	545/600	2.0 ns	29	
Ag-620	540/620	2.2 ns	32	120,000
Ag-660	595/660	3.0 ns	18	350,000
Ag-680	620/680	3.0 ns	37	125,000

parameters, in table 3.2. Based on these values and the starting concentration of scaffold, typical synthetic yields of Ag nanoclusters are ~1%.

Fluorescence lifetimes were also measured for each species. Using pulsed excitation, 532 nm for Ag-620 and Ag-680, 647 nm for Ag-680, time correlated fluorescence was collected with a multi-channel photo multiplier tube. The resulting histograms of the interval between the sync pulse and the photon arrival time were fit to determine the lifetime. Similar to the poly-cytosine encapsulated Ag nanoclusters, all of the species demonstrated lifetimes in the range of a few nanoseconds (table 3.2). Nanosecond lifetimes in previously studied poly-cytosine have been predictive of relatively bright and photostable single molecule emission.

3.5 Nanocluster Size Determination

Commonly used fluorescent labels vary in size from relatively small organic dyes (mw ~ 500-1000) to extremely large fully functionalized quantum dots (30 nm). Probe size is a major concern in biological imaging, as large molecules suffer from poor cellular uptake and can alter cellular dynamics. As a consequence, probe size must be kept to a minimum. While oligonucleotide size can be estimated from strand length, the scaffold likely experiences a conformational change during encapsulation. In fact, silver ions cause a significant change in the conformation of large DNA chains and addition of BH_4 leads to further contraction of the scaffold.[156] Ag nanocluster formation likely produces a similar effect given the efficiency of the scaffold.

To determine the approximate size of the Ag nanocluster-scaffold complex, we performed fluorescence correlation spectroscopy studies comparing the clusters to a

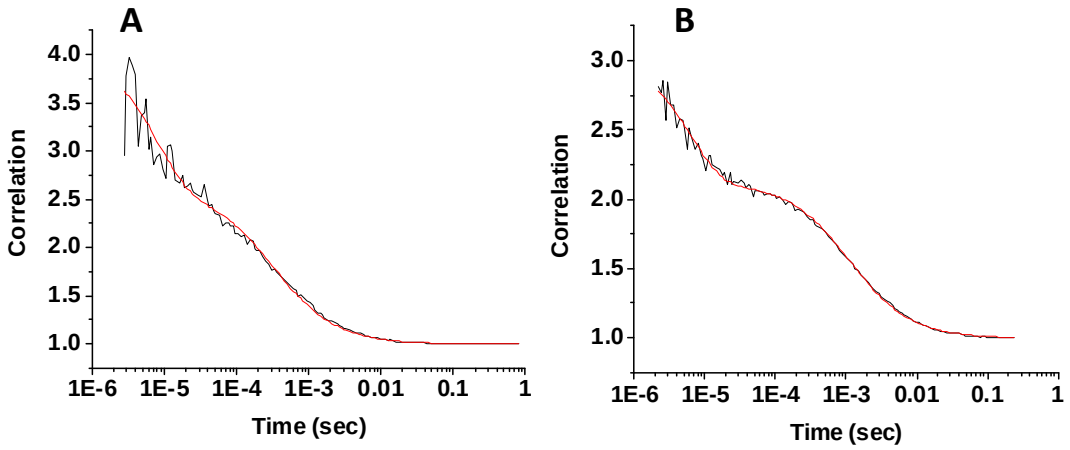

Figure 3.5. Autocorrelation from fluorescence correlation spectroscopy comparison of Cy 5 (A) to Ag-710 (B) where the correlation shows .6 molecules of Cy5 with a diffusion time of .30 ms and .8 Ag nanocluster molecules with a diffusion time of 1.1 ms.

fluorescent dye with a known diffusion constant in aqueous solutions. Cy5 is an adequate control for comparison with Ag-710, due to their similar emission wavelengths and bulk photophysical properties. Diffusion times of various concentrations of cy5 were measured by focusing a laser 30 microns into solution and collecting the resulting fluorescence. The cy5 autocorrelation, excited with a 633 nm cw laser (10 μW), shows .6 molecules on average in the focal volume with a diffusion time (τ_D) of .30 ms (Figure 4.1A). Using the same excitation intensity a solution of Ag-710 was diluted until FCS measurements showed ~1 molecule in the focal volume. Figure 4.1B shows the resulting autocorrelation of the Ag-710 solution with an average number of molecules of .8 and a diffusion time of 1.11 ms. The focal volume can be calibrated using the known diffusion constant (D) for cy5 (3.16 x 10^{-10} m^2/s) which is then used to calculate the diffusion constant for Ag-710.

Based on the FCS equations previously discussed the 3-dimensional Gaussian distributed excitation profile gives the transit time through the focal volume.

$$\tau_D = \frac{{\omega_0}^2}{4D} \qquad \text{Equation 4.2}$$

where τ_D is the measured diffusion time, ω_0 is the waist size defined by the boundary where the Gaussian excitation profile decays to $1/e^2$ in the x and y directions, and D is the diffusion constant. Using the FCS comparison the diffusion constant of Ag-710 was calculated at 8.65 x 10^{-11} m^2/s. The calculated diffusion constant relates to the hydrodynamic radius via the Einstein-Stokes equation (4.3)[157]

$$D = \frac{k_B T}{6\pi\eta R_h} \qquad \text{Equation 4.3}$$

where η = viscosity, T = temperature, k_B = Boltzman constant, and R_h= hydrodynamic radius. Solving for the radius and substituting in for the diffusion constant gives a hydrodynamic radius of 2.76 nm for the Ag nanocluster. While slightly larger than typical organic dyes, Ag nanoclusters are at least an order of magnitude smaller than quantum dots.[4,158] Even at these relatively small sizes, concern about the perturbation of biological systems is still relevant. While smaller oligonucleotide scaffolds (6-8 bases) nicely form fluorescent Ag nanoclusters, they have up to this point not been optimized to target specific fluorescent species. Reducing the overall size of the fluorescent label through smaller scaffolds should be feasible with optimization similar to that demonstrated for 12-mer DNA.

3.6 Evaluation of Scaffold Specificity

The microarray studies clearly show that variation of the base sequence alters Ag nanocluster formation. Additionally, the 20% success rate, for transitioning from the array to solution, suggests that end effects may cause changes in the formation efficiency. Oligonucleotide functionalization for attachment chemistry is vital to the use of Ag nanoclusters as biological probes. One common linker system is avidin-biotin which is widely used in biolabeling.[159,160] IDT provides oligonucleotides with biotin attached to either the 5', 3' or internally. Using these scaffolds, studies were performed to determine the effect of biotin conjugation on Ag nanocluster formation, both at the 3' and the 5' ends.

Attempting to duplicate the fluorescence from non-biotinylated scaffolds, solutions were initially synthesized with the same procedure in non buffered aqueous

solutions. In these solutions, none of the biotinylated scaffolds demonstrated the same spectral purity previously shown for the naked DNA strand. For example, the normal Ag-660 sequence lost almost all ability to form the 660 nm emissive species, forming instead a species with emission at 500 nm (Figure 3.5A). The simple addition of the small biotin unit to the DNA completely modified the encapsulation properties of each of the strands, suggesting that end effects influence the conformation of the scaffold. Exploring the possibility that a constant pH may help stabilize the conformation of the scaffold, various buffered solutions were used for synthesis of the biotinylated sequences. The same modified scaffolds in a pH 7 phosphate buffer now showed improved encapsulation properties. Figure 3.5 B shows the fluorescence spectra of the 5' biotinylated Ag-660 oligonucleotide (5'-CCCATATTCCCC-3'). The 660 nm emission is now partially recovered, but several other fluorescent species are also present. Testing the same scaffold at various other pH values (5-9) resulted in no improvement. These results suggest that Ag-660 formation is incompatible with 5' modification.

Derived initially from microarrays with 3' bound oligonucleotides, 3' modified scaffolds were investigated under similar experimental conditions. Unbuffered solutions showed significant improvement over the 5' modified scaffolds. While not completely spectrally pure, Ag-660 is the primary emissive species with only one other prominent species at higher energy emission (Figure 3.5C). Repeating the synthesis in buffered solution (pH 7 phosphate) (Figure 3.5 D) resulted in spectral purity on par with that typically seen for non-biotinylated scaffolds. Further studies at both pH 5 and pH 9 resulted in almost complete loss of all fluorescence. This demonstrates that Ag-660

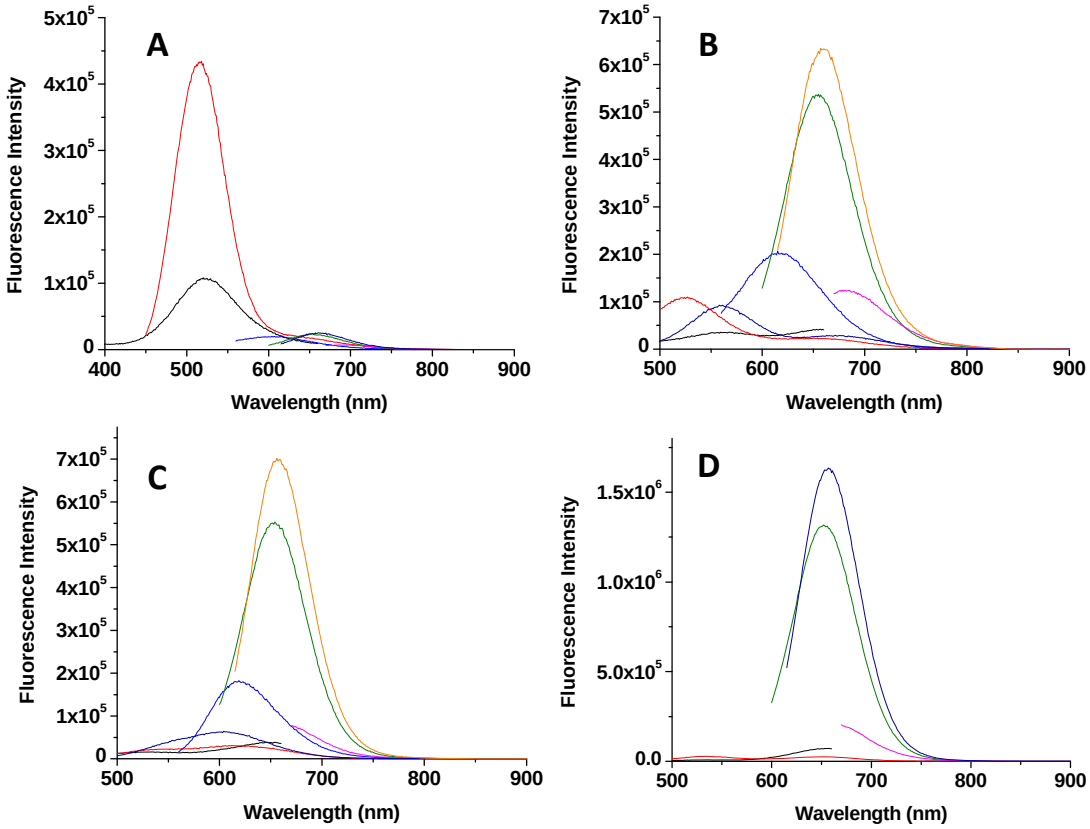

Figure 3.6. A. The 5' biotinylated scaffold for Ag-660 in an unbuffered solution showing the lack of formation of the target species. B. The 5' biotinylated scaffold for Ag-660 in a buffered solution (pH 7) showing multiple species including the target species. C. The 3' biotinylated scaffold for Ag-660 in an unbuffered solution with a predominate 660 nm peak but containing an additional species. D. The 3' biotinylated scaffold for Ag-660 at pH 7 showing spectrally pure 660 nm emission.

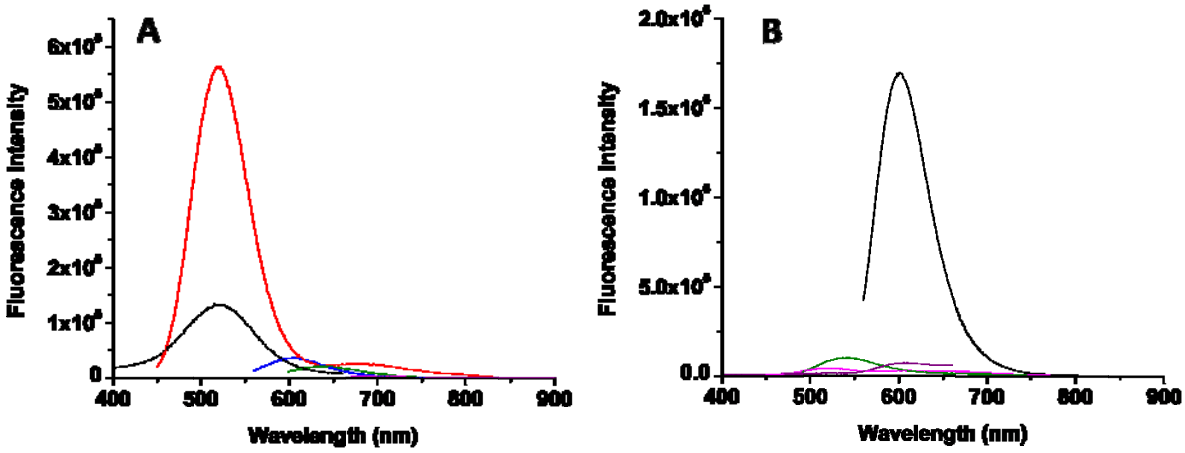

Figure 3.7. A. The 5' biotinylated scaffold for Ag-600 in an unbuffered solution showing the near spectrally pure formation of a non-target species emitting near 500 nm. B. The 5' biotinylated scaffold for Ag-600 in a buffered solution (pH 7) showing spectrally pure formation of the 600 nm emitter.

conjugation is both end and pH dependent, allowing for the optimization of fully functionalized Ag nanocluster scaffolds.

Similar experiments on the remaining fluorescent species were completed with varying degrees of success. Biotinylation of Ag-620 resulting in almost no fluorescence for either end of the oligonucleotide regardless of experimental conditions. In deionized water, 5' biotinylation of Ag-600 led to the formation of a completely new species with higher energy emission (Figure 3.6A). Interestingly, at ph 7 this completely symmetric sequence, 5'-CCACCAACCACC-3', showed remarkable spectral purity for 5' modification (Figure 3.6B), while 3' modification completely eliminated the target species. Ag-680 showed the same dependence on buffered solutions (pH 7) but was readily formed with the same spectral purity as the naked strand with either 5' or 3' modification. Ag-680 was the only sequence to demonstrate absolutely no dependence on the conjugation position. Notwithstanding the Ag-680 results, end effects seem to play a major role in the formation of most target species.

While both strand sequence and scaffold modifications directly impact templating properties, Ag-660 and Ag-680 exhibited spectral purity under various conditions. To test the specificity of these scaffolds, individual bases were systematically replaced at all 12 strand positions one at a time. Guanine was used to replace each position of the Ag-660 scaffold as shown below where individual bases that were switched are in red.

CCCATATTCCCC	Ag-660
GCCATATTCCCC	No Fluorescence
CGCATATTCCCC	No Fluorescence
CCGATATTCCCC	No Fluorescence
CCCGTATTCCCC	Transient Emission (Unstable)
CCCAGATTCCCC	610 exc 675 Emission
CCCATGTTCCCC	Transient Emission (Unstable)
CCCATAGTCCCC	Weak mixture of species
CCCATATGCCCC	570 exc 640 Emission
CCCATATTGCCC	565 exc 640 Emission
CCCATATTCGCC	No Fluorescence
CCCATATTCCGC	No Fluorescence
CCCATATTCCCG	No Fluorescence

Depending on the position of the replacement, the results varied significantly. Changing the last 3 bases on either end resulted in all fluorescence being completely eliminated, further suggesting that end effects play an important role in Ag nanocluster formation. Replacing any of the six middle bases disrupted the formation of Ag-660, giving rise to several different species depending on the replacement location. This can be seen by comparing representative fluorescence spectra, the unchanged scaffold forms spectrally pure Ag-660 (Figure 3.7A), replacing the first cytosine on the 5' end eliminates all fluorescence (Figure 3.7B), and replacing the fifth-position thymine results in an entirely different fluorescent species (Figure 3.7C). In contrast to the biotinylation studies, where buffered solutions could be used to stabilize the scaffold, identical results were observed for deionized water and pH values ranging from 5 to 9.

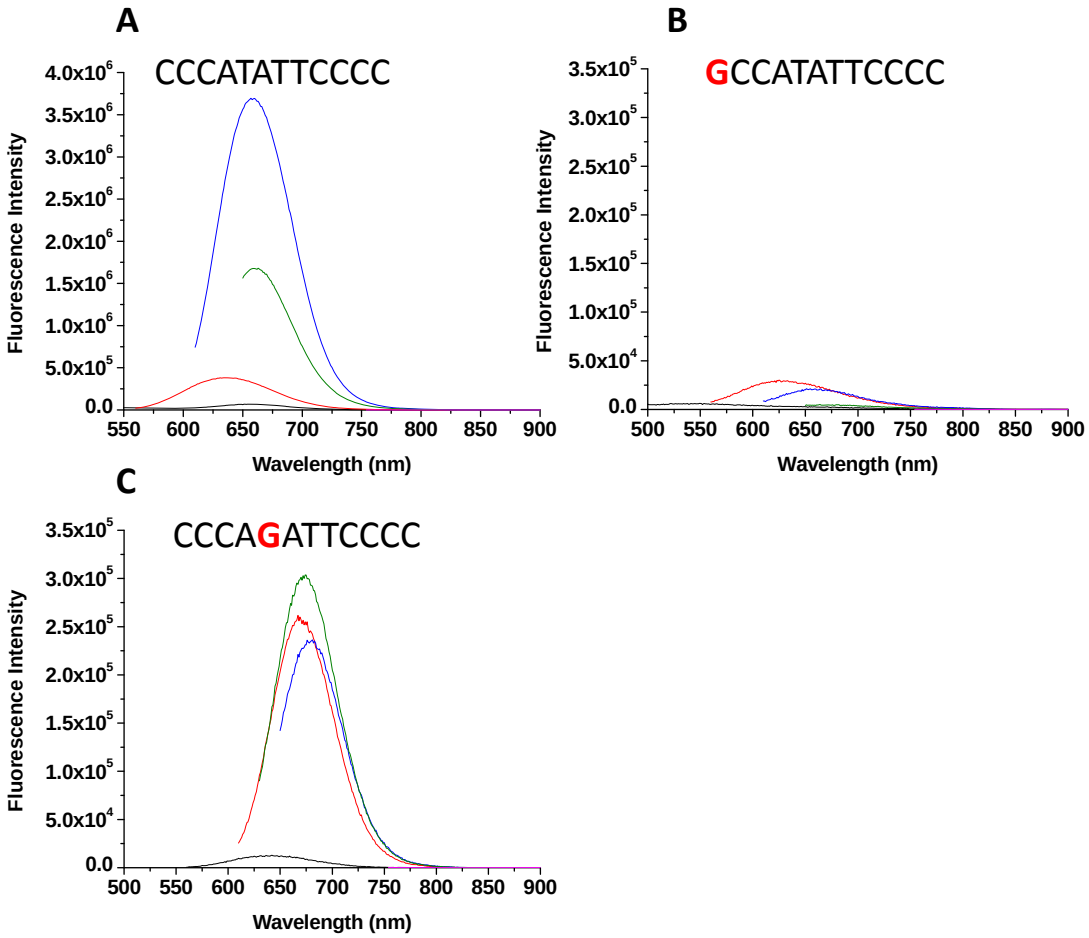

Figure 3.8. A. Spectra of typical Ag-660 in unbuffered solution. B. Spectra from a modified Ag-660 scaffold with the cytosine in the first position changed to a guanine showing almost complete elimination of all fluorescence. C. Spectra from a modified Ag-660 scaffold with the thymine in the 5th position changed to a guanine showing the formation of a completely different fluorescence species.

Replacing the bases in the same systematic fashion for Ag-680, yields almost identical trends. Changing the first 3 or last 3 positions resulted in the complete elimination of all fluorescent species; yet changing the interior bases merely changed the fluorescent species formed. For both Ag-660 and Ag-680, buffered solutions had no affect on the formation of the fluorescence. It is hard to draw conclusions from these studies on the role of the individual bases in the binding of the cluster or in the conformation of the sequence. The results, however, clearly show the specificity of individual sequences for Ag nanocluster formation.

3.7 Conclusion

While poly-cytosine oligonucleotides readily encapsulated fluorescent Ag nanoclusters, these scaffolds lacked specificity, simultaneously forming multiple fluorescent species. Using microarray screening, scaffolds were identified that specifically encapsulated individual species of Ag nanocluster, resulting in spectrally pure solutions. Several species were discovered and characterized. Demonstrating high quantum yields, large extinction coefficients, and relatively short lifetimes, these new species exhibited bright emission. These scaffolds are highly sensitive to sequence modifications and scaffold functionalization, where slight changes disrupt cluster formation. Despite these issues, attachment chemistry was optimized for several spectrally pure species confirming their potential as biolabels.

CHAPTER 4
SINGLE MOLECULE PHOTOPHYSICS

4.1 Introduction

Complementary to bulk imaging, single molecule spectroscopy can be used to study specific kinetic events, revealing subcellular dynamics that are often masked by ensemble averaging. Single molecule imaging in biology, however, is mainly restricted to in vitro studies due to a lack of sensitivity influenced by both insufficient probe brightness and high intracellular background. Despite exhibiting bright emission at the bulk level, photophysical behavior under single molecule imaging conditions often results in reduced emission rates and poor photostability.[161,162] This is particularly evident in single molecule blinking, caused by stochastic transitions into a dark state. The high excitation intensities (>1 kW/cm^2) required for single molecule imaging, lead to more frequent dark state transitions and to faster photobleaching as compared to bulk imaging which typically uses lower intensities.

While blinking is universally exhibited by fluorescent dyes,[68-70] it originates from many different processes including triplet transitions, isomerization, and charge transfer. Dark state lifetimes in these states range from microseconds to several milliseconds.[69,78,86,87,163] Regardless of its origin, dark state population reduces fluorophore brightness through premature saturation by limiting subsequent ground state absorption needed to regenerate the emissive state. The amount of fluorescence dampening can be described by equation 4.1

$$I = \frac{\tau_{on}}{\tau_{on} + \tau_{off}} I_{on} + \frac{\tau_{off}}{\tau_{on} + \tau_{off}} I_{off} \qquad \text{Equation 4.1}$$

where τ_{on} is the time the molecule cycles between the ground and emissive state before transitioning to the dark state and τ_{off} is the life time of the dark state. Clearly, the average intensity is reduced by long dark state residence. The process only marginally affects bulk imaging where the signal is generated by simultaneous emission from multiple fluroophores, but is readily evident in single molecule measurements.

Single molecule spectroscopy can be used to explore the dynamics of individual biological activity such as transcription,[7,164,165] protein interactions,[166,167] and protein folding.[168] Studies, however, are limited by experimental sensitivity partially due to reduced brightness as a result of this dampening effect. Additionally residence time in these dark states is often directly correlated to photostability.[69,79] Therefore, understanding blinking dynamics is instrumental in determining a probes utility as a single molecule fluorophore. Poly-cytosine encapsulated Ag nanoclusters have previously demonstrated bright single molecule emission and limited dark state dynamics on the microsecond time scale. Initial studies suggest, that these spectrally pure nanoclusters are likely to exhibit similarly high emission rates at the single molecule level.

4.2 Blinking Dynamics of Immobilized Molecules

The detrimental effect of blinking is multifold: depression of emission intensities, complication of measured biological kinetics, and a creation of a pathway to accelerate permanent photobleaching. Blinking dynamics can be investigated at the ensemble level with the use of excited state transient absorption. Such studies readily yield dark state lifetimes and details of excited state absorption but provide little information on how

these processes affect emission rates. For multiple Ag nanocluster species, transient absorption revealed the presence of microsecond long dark states.[126] Correlation analysis of immobilized molecules can be used to get a more thorough understanding of these dark states and how they relates to the apparently high emission rates.[67] Similar to FCS, correlation analysis can be used to determine the time scale of intensity fluctuations from single molecule emission. Here the molecule is held in the laser focus rather than diffusing through, as is the case with FCS. The result is that intensity fluctuations can be monitored for long times until the molecule ultimately photobleaches. Understanding these processes should help provide insight to how they affect emission rates and photostability.

Poly(vinyl alcohol) (PVA) films were used to immobilize Ag nanoclusters by diluting stock solution of the red emitting species 1 to 10,000 in PVA. The solution was then spin coated onto a coverslip rotating at 1000 revolutions per minute. This results in an even film across the surface where individual molecules are fixed and well separated. Cyanine dyes exhibit similar bulk characteristics to several Ag nanocluster species, so are used for a comparison of both brightness and blinking dynamics. Dye samples were immobilized in the same as described for nanoclusters. Exciting separate samples of red emitting Ag nanoclusters and cy3 each with a 568 nm laser (1.3 kW/cm^2), single molecule time traces were recorded. Long time scale blinking dynamics can be observed simply by averaging the time trace intensity (binning) at time increments faster than the blinking dynamics. This process can be used to identify dynamics down to milliseconds

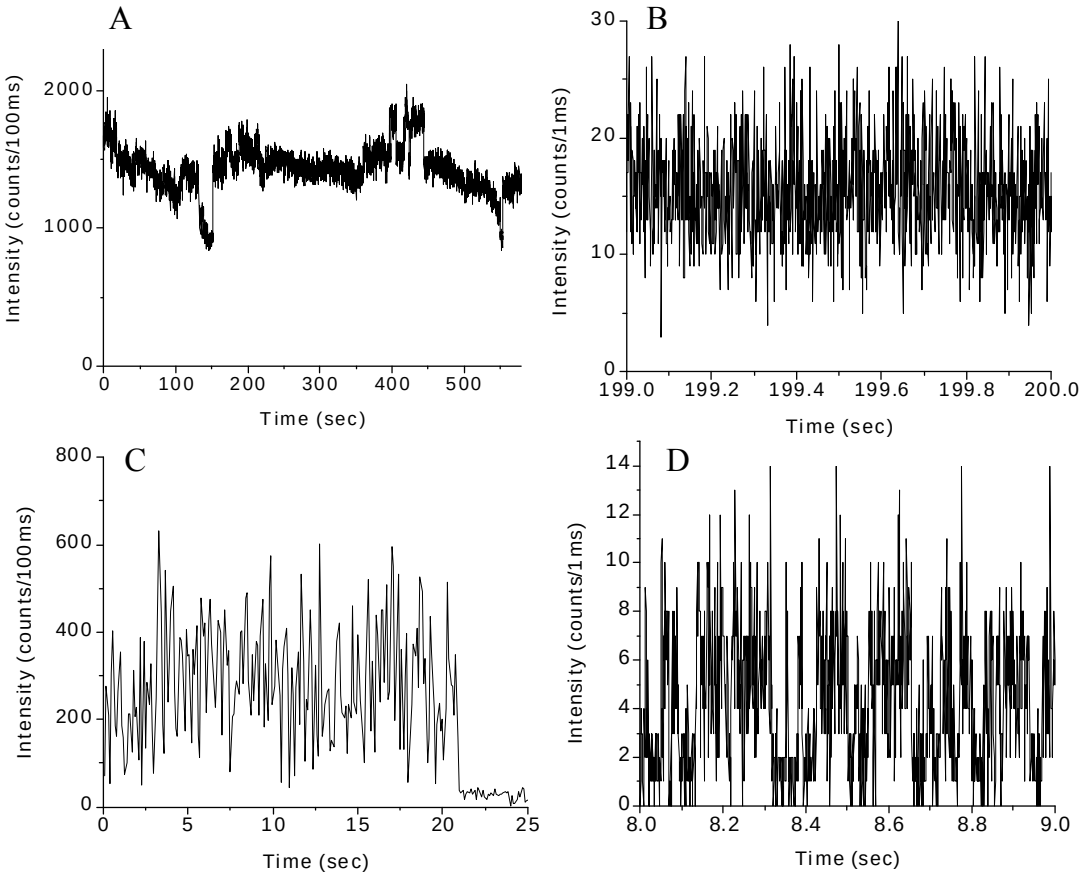

Figure 4.1. PVA immobilized samples of Ag nanocluster and cy3 excited with 568 nm laser (1.3 kW/cm^2) A. Time trace of the red emitting Ag nanocluster binned at 100 ms and (B) binned at 1 ms showing no fluorescence intermittency on this time scale. C. Time trace of an individual molecule of cy3 binned at 100 ms and (D) binned at 1 ms showing periodic fluorescence intermittency.

given sufficient count rates. Simple inspection of time traces of Ag nanocluster emission binned at 100 ms (fig 4.1A) and 1ms (4.1B) show no obvious blinking activity verifying intermittency occurs only at faster time scales. Comparative cy3 data binned at 100 ms (fig 4.1C) appears to show some poorly resolved blinking. This blinking becomes more evident with 1ms binning (4.1D). Characterized by the intensity periodically falling to the background, cy3 blinking leads to diminished emission rates. The spikes of fluorescence in between off states easily reach 10 counts/ms, corresponding to a count rate of 10,000 cnts per second while in the on state. As a result of the blinking the average cy3 emission intensity is merely ~4000 counts per second. On the other hand, Ag nanoclusters show average emission rates of 15,000 counts per second (figures 4.1A &B). With similar ensemble photophysics, this factor of 4 difference in brightness stems directly from the contrasting blinking dynamics.

Additionally, the cy3 molecule bleaches rapidly (~ 20 sec, Figure 4.1C) while the Ag nanocluster emits continuously for nearly 600 seconds before bleaching (Figure 4.1A). The presence of the dark state alone is not sufficient to suggest that it is associated with bleaching, but it is clear that cy3 blinks on a longer time scale and bleaches much more rapidly than Ag nanoclusters. Clearly in terms of single molecule brightness, Ag nanoclusters hold distinct advantages over cy3.

Using the same experimental conditions, ~100 single molecule time traces were collected. Correlation analysis of these molecules was used to build up statistical information on Ag nanocluster blinking dynamics. Individual molecules were incrementally excited for 10 seconds at three separate intensity levels 1, 5.2, and 10

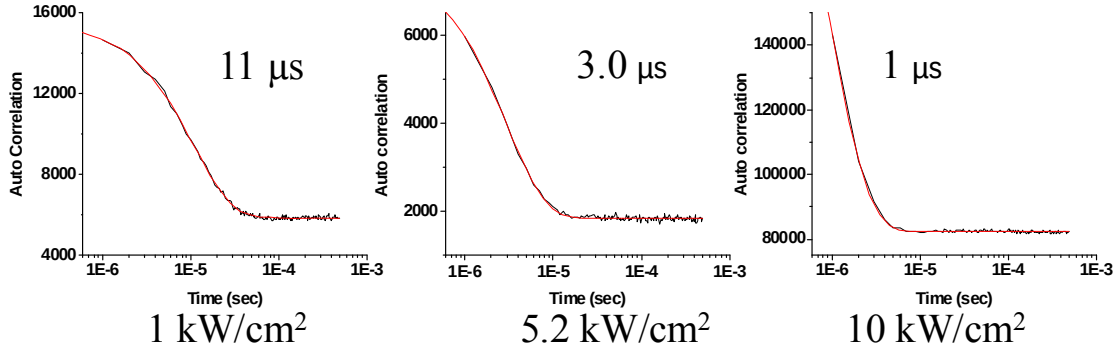

Figure 4.2. Autocorrelation of an individual red emitting Ag nanocluster immobilized in a polymer film excited at (A) 1 kW/cm^2, (B) 5.2 kW/cm^2, and (C) 10.4 kW/cm^2 showing exponential decays of 11 µs, 3 µs, and 1 µs, respectively.

kW/cm^2. Typical auto correlations taken for each segment of the resulting time traces are shown in figure 4.2. Fitting the correlations to an exponential decay extracts the time characteristic of the blinking process. Comparing the three different intensities reveals a clear trend. As the excitation intensity is increased the decay time decreases going from 11 μs to 3 μs down 1 μs at 1, 5.2 and 10 kW/cm^2, respectively.

The intensity dependence for the decay time of the fluorescence intermittency is expected based on dark state population photophysics. The "on time" is directly related to the dark state quantum yield and the excitation rate into the emissive state, so higher intensities should lead to a shortening of the "on time". The faster the molecule cycles between the ground and excited states (higher excitation intensity), the larger the probability of depopulating the emissive state. Conversely, the off time (residence time in the dark state) should have no sensitivity to the laser intensity as it would not be accessible by the same laser excitation. Although some researchers have reported dyes with optically accessible dark states that excite at the same wavelength as the ground state absorption, they were only viable with MW/cm^2 intensities.[169]

Specific off ($\boldsymbol{\tau_{off}}$) and on ($\boldsymbol{\tau_{on}}$) times can be extracted from the fitted correlation time ($\boldsymbol{\tau_c}$) by modeling the photophysical processes assuming a 3-level system. The relationships described in equations 4.2-4.5 can be used to derive values for the "on times", "off times", and the rate constant for the dark state transition ($\mathbf{K_D}$). Here Φ_{fl} is the fluorescence quantum yield (0.32), Φ_{eff} is the detection efficiency (0.05), τ_{fl} is the fluorescence lifetime, and I_{on} is the intensity/bin while in the "on state".

$$C(t) = A+Be^{-t/\tau_c} \qquad \text{Equation 4.2}$$

$$1/\tau_c = 1/\tau_{on} + 1/\tau_{off} \qquad \text{Equation 4.3}$$

$$\tau_{on}/\tau_{off} = A/B \qquad \text{Equation 4.4}$$

$$K_D=\Phi_{fl}\Phi_{eff}/\tau_{fl}\tau_{on}I_{on} \qquad \text{Equation 4.5}$$

Extracted on and off times averaged for ~100 molecules are listed for each of the excitation intensities in table 4.1. When excited at a relatively low intensity (1 kW/cm^2), the corresponding on and off times were both approximately 30 microseconds. As the intensity was increased, the expected decrease in the "on time" was evident, reducing to less than 3 μs at 10 kW/cm^2. As predicted, this nicely obeys the photophysical model. As we increase the rate of population of the excited state, the dark state population also increases shortening the on time.

An unexpected consequence of increasing the intensity was a corresponding decrease in the off time. The off time reduced from 30 μs to 7 μs when the intensity was increased from 1 to 10 kW/cm^2. Neither the larger emissive state excitation rate nor more rapid dark state population should contribute to residence time in the dark state. This suggests that the dark state undergoes some optically induced transition, that is at least partially in resonance with the excitation. The laser is either pushing the electron into a higher energy dark state that repopulates the emissive manifold or stimulating a radiationless transition directly back to the ground state. Both pathways repopulate the emissive state allowing ground state absorption and subsequent early regeneration of the on cycle. This surprising behavior helps to ameliorate the detrimental effect of non-fluorescing dark states. As will be explored in later chapters, optically shortening the dark state and repopulating the emissive manifold can be used to develop new imaging concepts based on fluorophore photobrightening.

Table 4.1. Extracted data from exponential fits of autocorrelation decays showing the on and off time averaged from 100 molecules and the rate constant for dark state population.

568nm (kW/cm^2)	τ_{on} (μs)	τ_{off} (μs)	K_D (s^{-1})	Φ_D	Burst Intensities Counts/sec
1.0	35.6	39.8	3038953	.009	46709
5.2	15.2	23.2	3177262	.009	144169
10.4	2.7	6.8	5475174	.016	399938

4.3 Photostability and Brightness

While the intensity levels necessary for single molecule excitation result in blinking behavior that reduces emission rates, another important single molecule characteristic is total photons emitted prior to photobleaching. For example, most organic dyes can emit approximately 10^7 photons prior to transitioning to a permanent dark state.[79] The high count rates necessary for single molecule observations, therefore restrict experimental observations times. With a fixed number of available photons, increasing the photons per second decreases the photostability of the molecule. While reducing excitation intensities results in longer lived molecules, it does so at the expense of emission rates. Of course reducing label brightness, particularly for diffusing biomolecules, in the presence of cellular autofluorescence leads to even lower sensitivity. These issue are also exacerbated in some environments. The presence of quenchers, such as oxygen, in biological systems tends to cause significantly faster bleaching as compared to deoxygenated solutions.[170,171] Thus, Ag nanocluster photostability at various excitation intensities, both in polymer films and more biologically relevant conditions, was investigated by comparison to organic dyes.

Solutions of Ag-620 were diluted (1:1,000) in saturated PVA solutions and then spin coated at 1000 rpm for 1 min in order to isolate individual molecules. Figure 4.3A show an image, with a 1-second exposure time, of individual Ag-620 molecules throughout the field of view. Figure 4.3B shows a corresponding frame 300 seconds later where approximately half of the original molecules are still fluorescing. These samples were exposed to relatively low intensity mercury lamp excitation which should limit dark

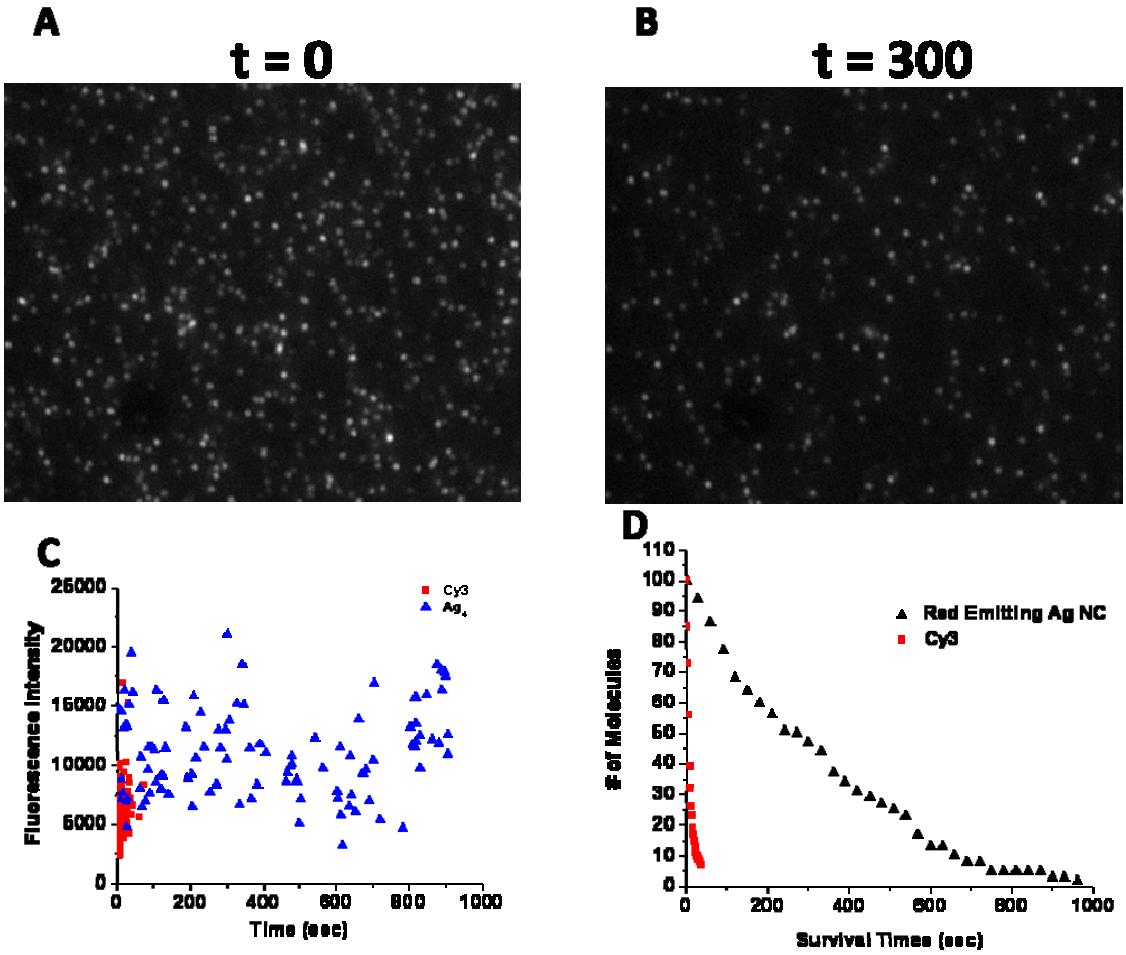

Figure 4.3. A. Initial frame of individual molecules of Ag-620 in a PVA film excited with low intensity mercury lamp detected with a ccd camera. B. The same set of molecules 300 seconds later showing approximately 50% of the molecules remaining. C. Plot of emission intensity vs failure time for 100 molecules of Ag nanocluster (blue triangles) and cy3 (red squares). D. Plot of failure times.

state transitions and reduce photobleaching. The Ag-620 molecules here appear to be much more stable than typically reported for organic dyes, which is consistent with the results seen in figure 4.1. For a more quantitative comparison, similarly emitting cy3 molecules, also immobilized in a PVA film, were imaged under identical conditions. Plotting the failure times, under prolonged mercury lamp excitation, of 100 molecules of both cy3 (red squares) and Ag-620 (black triangles) shows a stark difference between the two fluorophores (Figure 4.3C). Cy3 molecules bleach very rapidly with less than half the molecules still fluorescent after 20 seconds. In contrast, constant excitation of the Ag-620 molecules leads to bleaching of half the population only after more than 300 seconds. Simultaneous evaluation of fluorophore brightness showed that Ag nanoclusters yield an average of ~2500 counts per second, while cy3 had an average detected count rate of ~1500. Despite the similar ensemble photophysical parameters, Ag nanoclusters hold a clear advantage in brightness due to the more frequent and long lived dark state exhibited by the cyanine dye. It is unclear if photobleaching in either fluorophore is connected to the blinking, but Ag nanoclusters exhibit significantly better photostability as well. Under moderate excitation, which should limit transitions into the dark state and photobleaching, we already see clear advantage for Ag nanoclusters. At higher excitation intensities, typical for single molecule experiments, the difference should be more pronounced.

For high intensity excitation, spin coated films of Ag-710 were prepared with 1 to 10,000 dilution in PVA. With a confocal detection setup, 1 kW/cm^2 excitation (633 nm) resulted in emission rates of greater than 20,000 counts per second (Figure 4.4 black).

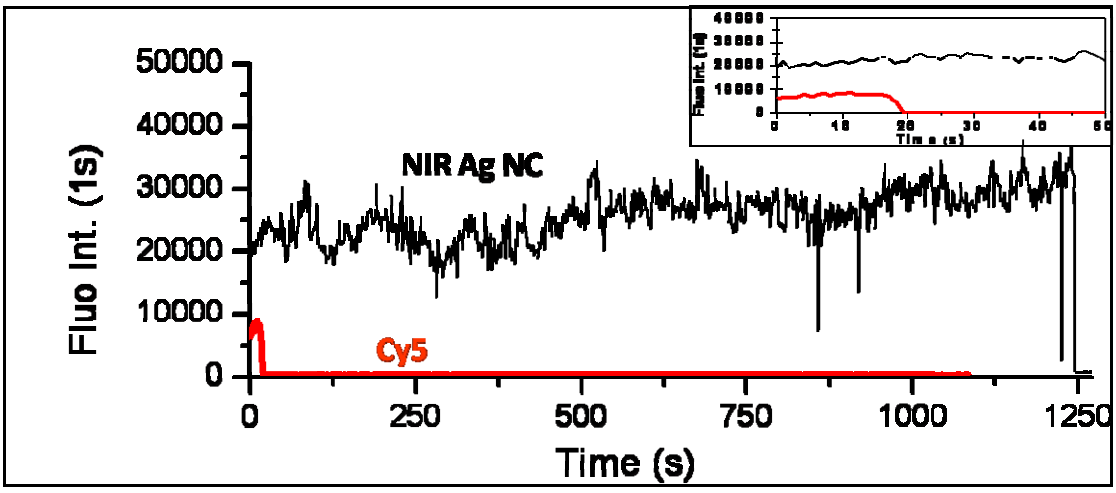

Figure 4.4. Single molecule time trace Ag-710 (black) and cy5 (red) under cw excitation at 633 nm (xx kW/cm^2). Inset is a zoomed in region showing cy5 bleaching.

Individual molecules of similarly emitting cy5, under the same conditions, emitted at less than half the rate of Ag nanoclusters (Figure 4.4 red). Even greater contrast is observed in the photostability. The Ag-710 molecule continues to emit for over 1200 seconds while the cy5 molecule bleaches in less than 20 seconds (inset figure 4.4). The disparity in the emission rate grew larger as the excitation intensity increased, suggesting the longer time scale intermittency caused greater attenuation of the relative emission rates for the organic fluorophore. This corresponds well with the model of premature saturation resulting from increased population of a long lived dark state.

While polymer films are a somewhat idealized environment, devoid of likely quenchers and at least partially impermeable to oxygen, these studies nicely demonstrate that commonly used organic dyes bleach at a significantly faster rate than Ag nanoclusters. A detection efficiency of 5% would indicate that this particular nanocluster emitted $6x10^8$ photons prior to bleaching. Factoring in the fluorescence quantum yield (.35), this level of emission equates to $\sim 10^9$ excitation cycles prior to irreversible photobleaching. This represents an increase of two orders of magnitude over typical organic dyes.

4.4 In Vitro Single Molecule Analysis

While important to understanding the photophysical properties of fluorescent systems, immobilized studies in polymer films lack any biological relevance. Biological imaging involves conditions that contain many components that can alter or detrimentally affect the photophysical properties of fluorescent dyes.[172] While FCS studies gave some insight into probe behavior in aqueous environments, individual dyes were exposed to the

excitation beam for a short period of time (< 1ms) when diffusing through the focal volume. Such studies are incompatible with accurate bleaching analysis. Additionally, the typical excitation intensities for FCS experiments (>10 kW/cm^2) are quite high relative to those for immobilized molecules. These higher excitation intensities lead to more rapid population of the dark state and premature photobleaching giving a skewed measure of the relevant photophysical behavior. Similar to most other dyes, Ag nanoclusters in solution are likely to exhibit significantly different behavior than seen in PVA. In order to immobilize molecules in an aqueous environment, avidin-biotin linker chemistry was used to attach the scaffold to the surface of a coverslip. An amine-terminated silane was used to functionalize the coverslip, coating the surface with amines. The coverslip was then exposed to a solution of .1% amine reactive biotinylated poly ethylene glycol (PEG) and 99.9% methyl terminated PEG. After rinsing, an excess of avidin is added to the coverslip to react with the biotinylated PEG on the surface of the coverslip. This results in a wide dispersion of the protein across the surface. The bioinylated scaffolds developed in chapter 3 are then used to anchor Ag nanoclusters to the surface attached proteins.

Ag-660 was synthesized in a biotinylated scaffold as described in chapter 3. These biotinylated Ag nanoclusters exhibit photophysical properties that are indistinct from traditionally synthesized clusters. Single molecule brightness studies were performed on isolated molecules in a typical confocal setup. Initially tracking isolated single molecules with a CCD camera, Ag-660 molecules were aligned to the pinhole to record single molecule trajectories. Figure 4.5 (black) shows the time trace of an isolated single molecule under solution (phosphate buffer pH 7). Initially excited at 1.1 kW/cm^2

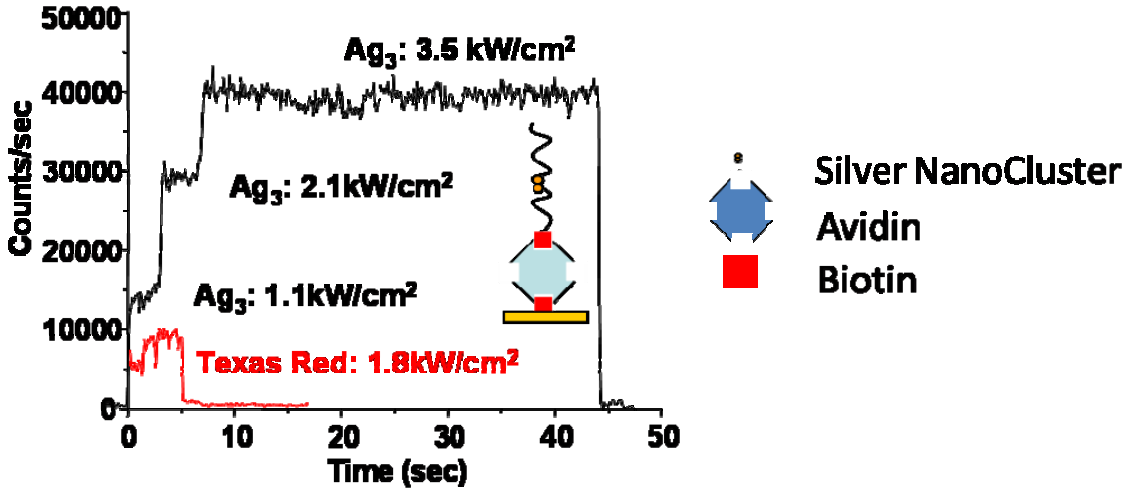

Figure 4.5. Time trace of an immobilized molecule under solution of Ag nanocluster (black) and texas red (red) with cw 594 excitation at increasing intensities.

(594 nm), emission rates reached ~14,000 counts per second. While moderately lower than the emission rates from PVA experiments, single Ag-660 molecules were significantly brighter than individual texas red molecules emitting at ~10,000 counts per (Figure 4.5 red) which was achieved only after increasing the excitation intensity to almost twice (1.8 kW/cm^2) that needed for Ag-660. Despite slightly diminished Ag nanocluster count rates, the relevant comparison is still between the Ag nanocluster and the organic dye which suffers from similar reductions. Texas red was substituted for cyanine dyes in these experiments as initial studies of surface bound cy5 and cy3 resulted in rapid photobleaching, to the extent that molecules would not survive the alignment procedure. While better than the cyanine dyes, texas red molecules only survived for ~5 seconds. After several seconds, the Ag nanocluster excitation intensity was increased by a factor of two resulting in a corresponding increase in the emission rate. The excitation intensity was then raised to 3.5 kW/cm^2 yielding emission of 40,000 counts per second. This molecule continuously emitted until finally bleaching after 45 seconds.

Demonstrating bright emission and excellent photostability in aqueous environments, single molecules of Ag-660 emitted close to 2 million detected photons before bleaching. Texas red barely emitted 50,000 detected photons under the same conditions. Such bright emission at lower excitation intensities should lead to improved sensitivity in biological imaging.

4.5 Long Time Scale Blinking Dynamics

Fluorescence intermittency is pervasive across almost all species of fluorescence dyes.[68-70] Blinking results from transitions into a variety of states, which are often sensitive to environmental conditions. These states include spin forbidden transitions to triplet states, charge transfer states resulting in electron delocalization, and structural changes in the fluorescent molecule via isomerization.[69,78,86,87,163] Patel and coworkers proposed that the microsecond blinking behavior expressed in all species of Ag nanocluster originates from charge transfer from the cluster that is delocalized along the ssDNA scaffold.[126] Detailed transient absorption studies showed that several Ag nanocluster species had near identical excited state absorption spectra. A rapidly formed dark state was also observed that exhibited a several microsecond lifetime, which is consistent with the blinking dynamics revealed through correlation analysis. Additionally, the absorption spectra of this state was remarkably similar to the spectra seen for photoinduced transfer to cytosine producing anionic cytosine.[173] The agreement between these studies suggests that delocalization of the excited electron onto the cytosine rich ssDNA is the origin of the blinking.

While blinking analysis has been thoroughly investigated for Ag nanoclusters in PVA films and aqueous solutions, studies had not been completed for clusters after conjugation to a relatively large macromolecule such as avidin. Immobilized molecules in polymer films with normal excitation intensities (< 4 kw/cm^2) yielded only the microsecond blinking component, however, higher intensities resulted in infrequent and random transitions to longer dark state (>1 sec). Given these poorly understood long lived dark states, and the proximity of the protein to the DNA scaffold it is possible that

further delocalization could occur lengthening the time scale of the intermittency under such conditions.

Anchoring Ag-660 to the surface as described earlier, molecules were imaged using a ccd-camera to record any long term blinking behavior. Using a defocused 594 nm laser (3 kW/cm^2) several molecules were simultaneously imaged. Upon initial excitation several molecules were observed blinking on a time scale longer than the frame rate (1 sec). In fact observing several continuous frames revealed that individual molecules remained dark for several frames before flashing back on intermittently. This is illustrated in a comparison of Figure 4.6A and B which shows frames of the same series 2 seconds apart. Initially several individual molecules are in the field of view, yet 2 seconds later nearly all of these molecules are no longer present, however, an entirely new set of molecules are visible. Thus, molecules exhibit such long off and on intervals that 1 second frame rates cannot resolve the blinking behavior. Such blinking, induced by simple conjugation chemistry, would render Ag nanoclusters useless as a biological label.

Following the model proposed for nanocluster dark state formation, electron transfer should result in a cationic silver cluster. As the long time scale blinking is seen only after attachment to avidin, further electron delocalization beyond the scaffold is the likely cause. Recently Tinnefeld and coworkers have explored the effects of various oxidizing and reducing solutions on the blinking dynamics of various fluorophores.[87,170,174] They showed that dark state transitions, resulting in a cationic radical fluorophore, could be readily restored to the emissive state with the addition of a weak reducing agent such as ascorbic acid.[174] Applying the same concept to Ag

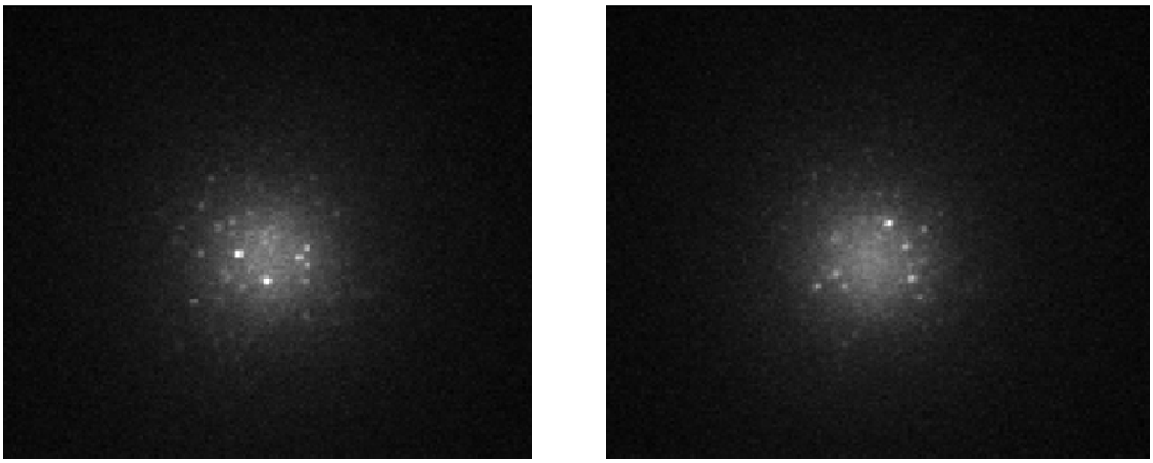

Frame 10 Frame 12

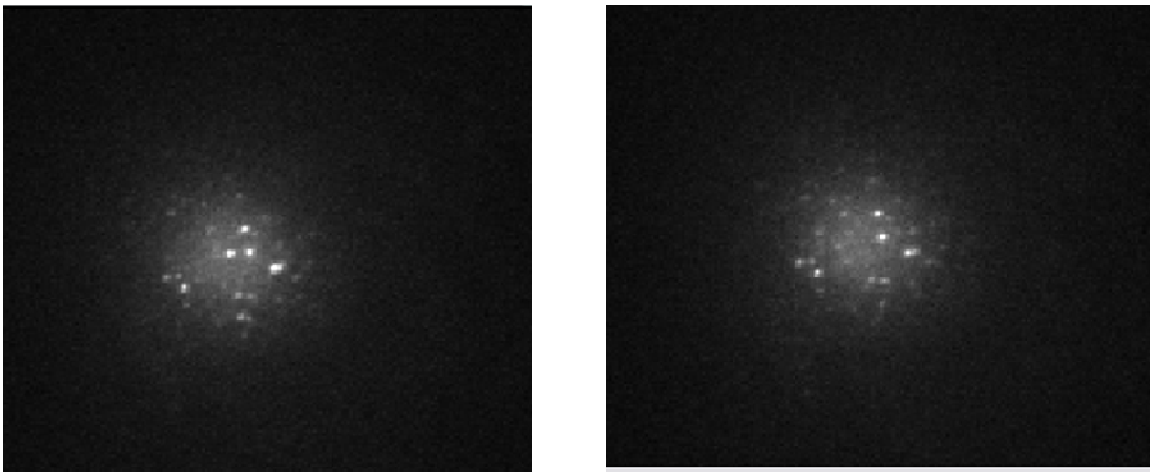

Frame 10 Frame 17

Figure 4.6. Frame 10 of a movie of Ag-660 molecules bound to the surface under solution (pH 7) and a frame from 2 seconds later illustrating the blinking. Frame 10 of a movie of Ag-660 molecules bound to the surface under solution (pH 7) including 100 μM ascorbic acid and a frame from 7 seconds later demonstrating an elimination of the blinking component.

nanoclusters 100 μM ascorbic acid was added to the exact same sample that exhibited the long time scale blinking in fig 4.6 A and 4.6B. Imaging with the same intensity and the same frame rate, a remarkable improvement in the stability of the fluorescence was observed, with no indication from frame to frame of any evident blinking behavior. A comparison of figure 4.6C and 4.6D demonstrates the marked difference. Taken 7 frames (7 sec) after C, the frame in D shows almost the exact same molecules as those exhibited in the earlier frame with the appearance of no additional fluorescent molecules. These molecules, even under relatively high excitation intensity (3 kW/cm^2), were quite photostable. The majority were actually still fluorescing at the end of the data collection (52 sec). Elimination of the long lived dark state through the addition of a reducing agent agreed quite well with the results shown by Tinnefeld. These results also help to substantiate Patel and coworkers proposed charge transfer blinking model.

While the long term blinking seen on conjugation to avidin can readily be eliminated, the addition of ascorbic acid could pose problems for biological samples. As a result, commercially available biotinylated DNA was ordered with a triethylene glycol (TEG) situated between the biotin and the oligonucleotide. This introduced a separation of approximately 1.5 nanometers. The scaffold with the TEG spacer showed identical Ag nanocluster phtophysics as that of the typical biotinylated scaffold and was readily synthesized with the same procedure. On binding with Avidin, Ag nanoclusters in these scaffolds demonstrated no long time scale blinking, behaving similarly to those seen in figure 4.6C & D. While adding size to the overall cluster-scaffold construct, the use of a spacer is more preferable for biological imaging than the addition of a potentially harmful reducing agent.

4.6 Conclusion

In this chapter, photophysical analysis of Ag nanoclusters was used to determine their viability as single molecule fluorophores for biological imaging. Comparison to standard fluorophores showed that several species of Ag nanoclusters exhibit significantly improved photostability and much higher emission rates. Unlike the cyanine dyes, Ag nanocluster exhibit intermittency only in the less biologically relevant microsecond time regime, reducing potential interference with the interpretation of biological dynamics and increasing brightness. Failure times of Ag nanoclusters under low excitation intensities showed that the red emitting species emitted roughly 40 times longer than the cy3 molecules under similar experimental conditions. Under higher excitation intensities typical for confocal microscopy led to an even greater disparity between nanoclusters and cyanine dyes, where clusters were emissive for close to 100 times longer.

Issues with longer time scale blinking of Ag nanoclusters were addressed through introduction of a weak reducing agent or by sufficiently separating the scaffold from the biotin-avidin linker with a TEG spacer. The increase in the scaffold size resulting from the addition of the spacer is not ideal. This places even greater importance on developing smaller oligonucleotide scaffolds. Addressing some of the issues that are prevalent in biological imaging such as photostability and probe brightness, the properties demonstrated here show marked improvement over most available fluorophores. As a result Ag nanoclusters show promise for improving sensitivity in biological imaging and in the development of new imaging techniques.

CHAPTER 5
HIGH SENSITIVITY SIGNAL EXTRACTION

5.1 Introduction

A lack of sensitivity is one of the most persistent challenges in biological imaging.[2,5] Complicated by deficient fluorophore brightness and high backgrounds, poor sensitivity limits fluorescence based applications, prohibiting true intracellular single molecule imaging. As seen in the previous chapter, already low fluorescence rates are diminished further by detrimental blinking, through the population of long lived dark states. Blinking is directly observed at the single molecule level, yet also manifests itself in bulk fluorescence, through decreased emission rates and more rapid photobleaching. Long lived dark states essentially trap the molecule such that it can no longer cycle between the ground and emissive states leading to premature saturation of the ground state absorption. One way to increase fluorophore brightness is to increase the excitation intensity. While this has the desired effect of increasing emission rates, the on time is also shortened, populating the dark state even more rapidly. Additionally, higher excitation intensities lead to increased background fluorescence resulting in limited or no increase in overall sensitivity.

If the dark state can be eliminated or rapidly depopulated, the emission rate would be enhanced relative to the fluorescence in the presence of the dark state. In fact, any depopulation of this dark state at a faster rate than the natural decay will enhance the rate of fluorescence. Achieving this without affecting the background fluorescence would also lead to improved sensitivity. A number of techniques have recently been employed in an effort to shorten the dark state lifetime. Tinnefeld and coworkers investigated

fluorescent systems that create charged states during dark state formation and used reducing and oxidative solutions to repopulate the emissive manifold.[87,174] Moderately successful at reducing fluorophore blinking, these methods are limited in biological imaging due to the introduction of highly concentrated reducing agents. Optical depopulation of the dark state has also been investigated as way to enhance fluorescence. Here a secondary laser, at lower energy than the emission, is used to excite the molecule to a higher energy dark state that subsequently repopulates the emissive manifold.

Ringemann and coworkers studied a series of fluorescent dyes and evaluated fluorescence under dual laser excitation observing only moderate enhancements (<10%) in solution.[175] Even these small increases in fluorescence, required extremely high secondary laser intensities (> MW/cm^2) due to the low action cross section for depopulation of the dark state. Not surprisingly, such large excitation intensities led to rapid photobleaching.[175] As previously detailed by equation 4.1, fluorescence dampening is directly related to the off time. As a result the fluorescence enhancement is also tied to the off time where the maximum possible enhancement is shown in equation 5.1

$$Max\ Enhancement = \frac{\tau_{on} + \tau_{off}}{\tau_{on}} \qquad \text{Equation 5.1}$$

This suggests that elimination of the dark state could lead to significant enhancement for many systems including Ag nanoclusters.

Examination of Ag nanocluster blinking dynamics revealed significant intensity dependence, with higher intensities leading to both on and off time shortening. In this case the primary laser excitation is directly depopulating the dark state. While increasing the intensity of this laser gives shorter off times and higher emission, the background

would also exhibit a corresponding increase, as it is directly dependent on the excitation intensity. However, if a secondary laser at lower energy than the emission can be used to depopulate the dark state, the target fluorescence would be increased while the background was unaffected. With higher emission but fixed background fluorescence, longer wavelength induced photobrightening should significantly improve sensitivity.

5.2. Dark State Depopulation

Increasing primary laser intensities was found to efficiently reduce dark state residence time for Ag nanoclusters. The primary excitation, therefore, likely co-excites the dark state and repopulates the emissive manifold. Several factors regulate this process. The excitation rate out of the dark state, k_D, depends on the absorption cross section, $\sigma_{D,}$ and the excitation intensity, I, where $k_D = \sigma_D I$. A large cross section allows for excitation at lower intensities. Once excited, the molecule can either cross over to the emissive manifold or simply relax back to the lower energy level. The probability for repopulating the emissive manifold is the dark sate quantum yield, Q_D^-. The action cross section, $\sigma_{Ac,}$ for this back transfer is the product of σ_D and Q_D^- where ($\sigma_{Ac} = \sigma_D Q_D^-$). So, efficient repopulation of the emissive manifold is characterized by large actions cross sections. To avoid increasing the background, while simultaneously enhancing the fluorescence; this transition should be efficient at lower energy (i.e. longer wavelength) than the emission.

Initial studies were performed to determine the optimum secondary wavelength for Ag nanocluster enhancement. A PVA immobilized sample, cast from a solution containing 100 nM Ag-710, was simultaneously excited with a 633 nm laser (1.2 kW/cm^2) and a tunable Ti-sapphire laser which was scanned from 750 nm to 975 nm (4

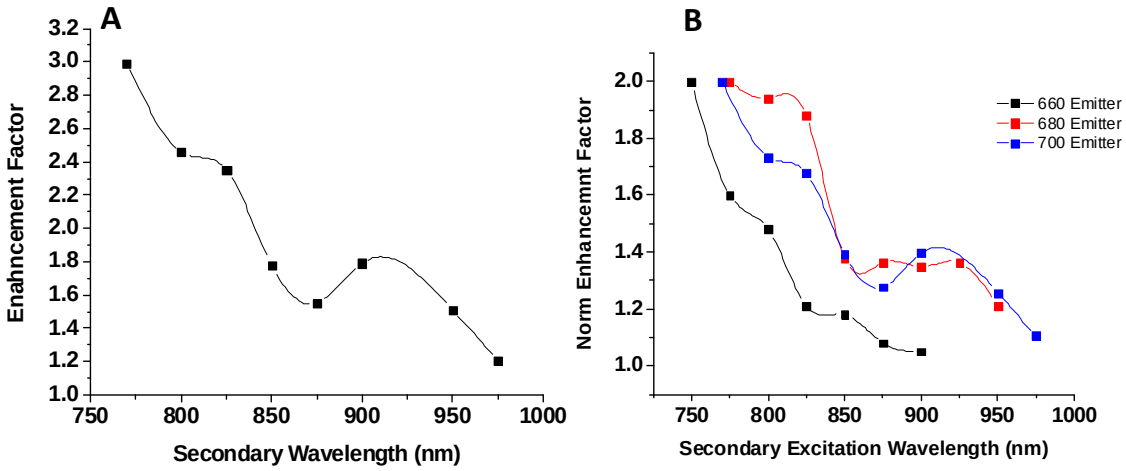

Figure 5.1. A. Excitation scan of the secondary laser inducing photobrightening shown by plotting the Enhancement factor versus the secondary wavelength. B. An overlay of the excitation scans for Ag-660 (black), Ag-680 (red), and Ag-710 (blue).

kW/cm^2). The emission rate during dual laser excitation was divided by the signal from single laser excitation giving an enhancement factor for each of the secondary wavelengths. Figure 5.1A shows the resulting secondary laser excitation scan, which reflects the relative action cross section for repopulation of the emissive manifold. Significant photobrightening (>50%) occurs over a majority of the spectrum and trends upward at shorter wavelengths. Spectral overlap between the secondary laser and the collected emission limited scans to the low energy side of 750 nm, thus a true excitation maximum was not observed. Repeating the experiment with additional Ag nanocluster species reveals similar behavior, where an overlay of the excitation scans for Ag-660, Ag-680, and Ag-710 shows remarkable similarities in the relative action cross sections (Figure 5.1B). As predicted by the anionic cytosine dark state model, this suggests a common origin for both the dark state and depopulation pathways. These studies demonstrate that lower energy secondary excitation can efficiently depopulate Ag nanocluster dark states, with three orders of magnitude lower intensities than used by Ringemann for common organic fluorophores.

5.3 Ag Nanocluster Photobrightening

Fluorescence enhancement induced by dark state depopulation should be feasible at both the ensemble and single molecule level. Ideally low excitation intensities, of no more than a few kW/cm^2, would be sufficient to generate maximum enhancement. Even though the secondary laser generates no additional background at the detection wavelength, high intensities could potentially be incompatible with biological studies. Based on the typical on and off times exhibited by Ag nanoclusters, single molecule

enhancement could be as much as 4 or 5 fold over single laser excitation. As sensitivity gains are directly tied to the level of enhancement, determination of these values and the factors affecting them are crucial to understanding potential applications in biological imaging.

Single molecule samples of Ag nanoclusters in PVA, prepared as described earlier, were initially excited with just a primary laser and then afterwards with a simultaneous secondary laser. For all studies a secondary wavelength of 805 nm was used as it is sufficiently removed from the emission of each of the nanoclusters but still generates significant enhancement. Recording the emission for both cases, enhancement factors were determined by calculating the ratio of emission from dual laser excitation to the emission from single laser excitation. To insure optimum polarization, a half wave plate was placed in the beam path of the primary laser and adjusted until the emission was maximized. The polarization for the secondary laser was then optimized by maximizing the enhancement. Both the primary and secondary excitation were sensitive to the polarization.

Exciting a single Ag-710 molecule with 633 nm primary laser (1.4 kW/cm^2), yielded an emission rate of roughly 40,000 counts per sec (Figure 5.2A). At the 10 second mark the sample was simultaneously exposed to an 805 nm secondary laser (6 kW/cm^2) which caused a near instantaneous increase in the count rate to 160,000 counts per sec (Figure 5.2A). The resulting 4-fold increase in the fluorescence intensity reveals significant single molecule photobrightening from relatively low secondary excitation intensity. Remarkably, even at these high emission rates the molecule still continuously emitted for almost 100 seconds before photobleaching. Assuming 5% detection

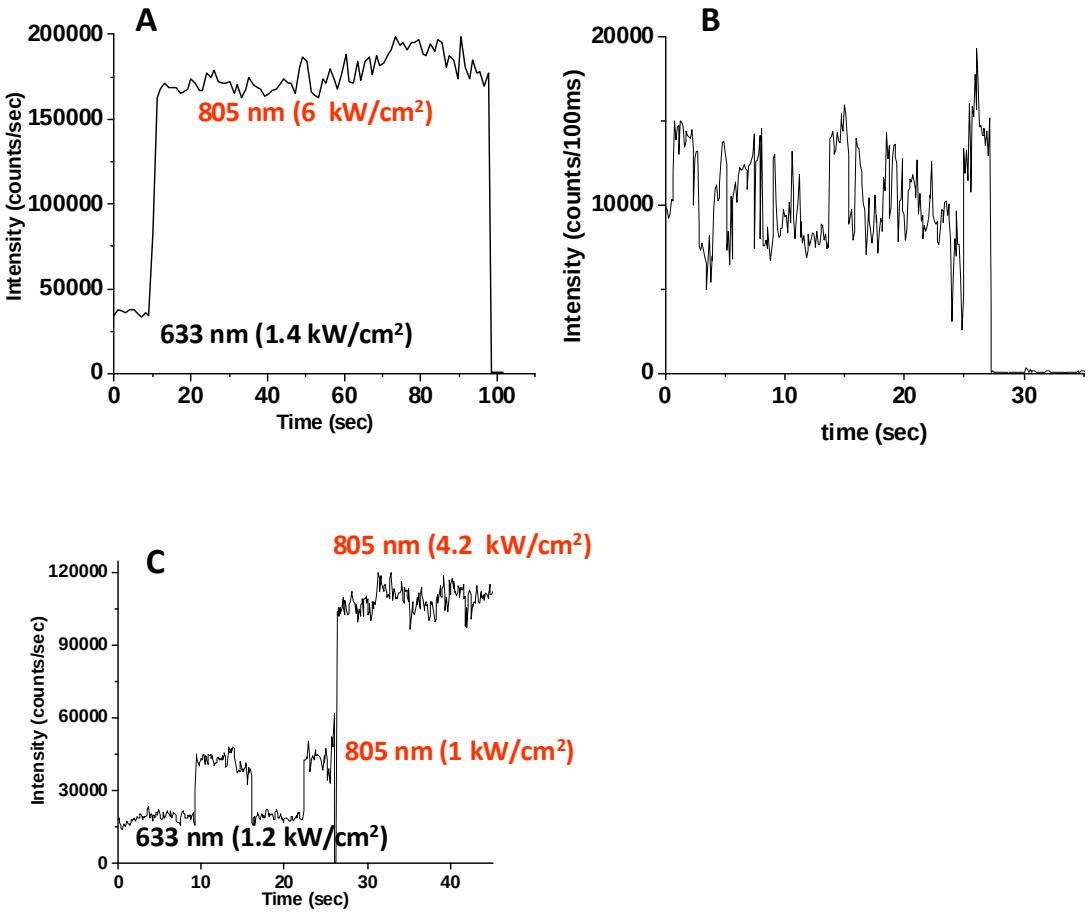

Figure 5.2. A. Time trace of a single Ag-710 molecule in PVA exposed initially to just a 633 nm laser (1.4 kW/cm^2) and then simultaneously exposed to an 800 nm laser (6 kW/cm^2). B. Time trace under single laser laser 633 nm excitation (6 kW/cm^2) showing high emission rates. C. Time trace under 633nm laser (1.2 kW/cm^2) and then simultaneously exposed to an 800 nm laser (1 kW/cm^2) and (4.2 kW/cm^2).

efficiency, this corresponds to approximately 300 million emitted photons prior to photobleaching. Factoring in the fluorescence quantum yield (35%), this level of emission represents approximately 10^{10} excitation cycles before permanent bleaching.

In terms of total number of emitted photons and excitation cycles, these studies fall within the same range seen for single laser excitation of an Ag-710 molecule with detected emission rates of ~ 35,000 counts per second (chapter 4). The strong correlation suggests that, although the secondary laser significantly increases the overall count rate, it does not result in more rapid photobleaching. If the dark state was an intermediate step leading to photobleaching, the reduced dark state lifetime would lead to better photostability. The evidence seen here suggests that bleaching is connected to a separate photophysical process altogether.

When the primary laser intensity is increased to sufficient levels ($6kW/cm^2$) to generate 150,000 counts per second, behavior with respect to bleaching and blinking changes considerably (Figure 5.2B). Much more rapid photobleaching is observed, resulting in barely 75 million emitted photons. Additionally, the intensity in the time trace fluctuates wildly before finally photobleaching at 28 seconds. Clearly higher primary laser intensities increase the probability of accessing photophysical processes that are unaffected by the secondary laser. These results, however, are preliminary, and additional studies are necessary to fully characterize the photophysical mechanism of Ag nanocluster bleaching. Still, dual laser excitation can generate constant emission at high count rates, without sacrificing the overall number of photons emitted.

Additional studies were performed to test the response of single molecule emission to varying secondary laser intensities. A single Ag-710 molecule was exposed

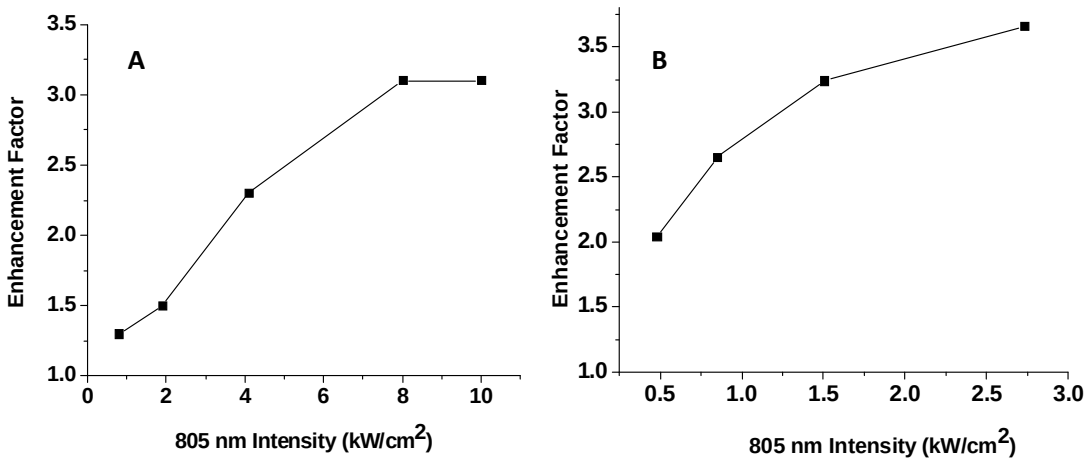

Figure 5.3. Secondary laser intensity dependence for Ag-710 (A) and Ag-620 (B). For both species the primary laser was held constant at 1.1 kW/cm^2 while the secondary laser was varied.

to a 633 nm laser (1.2 kW/cm^2) giving 20,000 counts per second (Figure 5.2C). In the presence of the secondary laser (1 kW/cm^2) the emission rate increased to 40,000 counts per second but dropped back to the lower single laser level when the secondary laser exposure was again interrupted (figure 5.2C). The same molecule was then exposed to higher secondary laser intensity (4.2 kW/cm^2), driving the emission rate over 100,000 counts per second. The ability to cycle back and forth between the lower and higher fluorescence levels in response to secondary laser exposure, suggests the fluorescence signal can be imparted with the properties of the secondary laser waveform.

To further examine the intensity dependence of the secondary laser, samples of both Ag-620 and Ag-710 were prepared such that single molecules were dispersed throughout the film and roughly 3-5 molecules were within the focus of the laser. Even at low secondary laser intensities (< 1kW/cm^2), both Ag-710 (Figure 5.3A) and Ag-620 (Figure 5.3B) exhibit fluorescence enhancement. The enhancement of Ag-710 starts to saturate near 10 kW/cm^2, while Ag-620 actually begins to saturate in less than 5 kW/cm^2, in both cases suggesting very efficient optical depopulation. This suggests large action cross section for transitions out of the dark state and back to the emissive manifold. The moderate secondary excitation intensities seen here are encouraging. Even though the secondary laser results in no additional background, extremely high intensities would still be prohibitive in biological imaging.

While single step bleaching such as that indicated in figure 5.2 A&B is suggestive of single molecule emission, photon antibunching experiments were performed for verification. Using a two detector confocal setup emission from an individual molecule, simultaneously excited with 633 nm (2 kW/cm^2) and 805 nm (8 kW/cm^2) light, was split

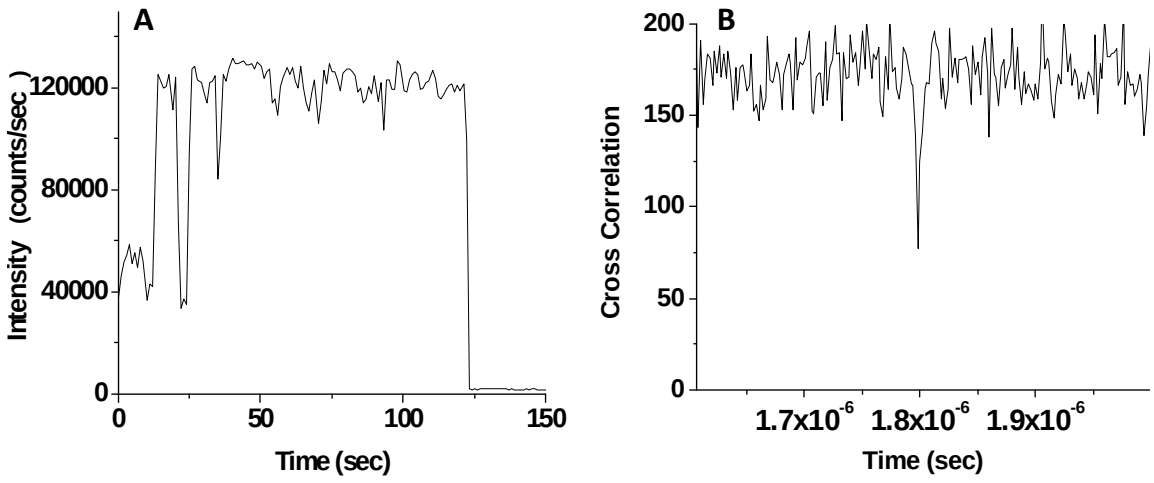

Figure 5.4. A. Combined time trace from 2 channels of an individual Ag-710 molecule excited with a 633 nm cw laser (2 kW/cm^2) and after 15 sec a secondary laser at 805 nm (8 kW/cm^2). B. The resulting cross correlation from A showing an antibunching peak at the delay time of 1.8 μs.

into two separate signals via a beam splitting fiber (100 μm). The resulting time traces from each fiber were collected separately at corresponding detectors. A 1.8 μs artificial delay was built into one channel so that the effective zero time difference between the channels could be shifted to a measurable value. As a single molecule can only emit one photon per excitation cycle, the probability of photons of the same molecule arriving simultaneously at the two detectors is near zero. The presence of a dip at 1.8 μs is then indicative of photon antibunching. Figure 5.4A shows a single molecule time trace which is the combined signal from the two separate channels, and the resulting cross correlation with ns resolution is shown in 5.4B. There is a clear dip below 50% of the base amplitude verifying single molecule emission.

5.4 Ag Nanocluster Photobrightening in Aqueous Environments

While studies in PVA films are useful for investigating photophysical properties, they are of little biological relevance. As a result, additional studies in aqueous solutions were performed to more adequately show the viability of Ag nanocluster photobrightening. FCS can be used to determine the number of molecules (N) in the focal volume which in conjunction with the average count rate (I) is used to calculate the brightness per molecule (q). This is achieved by simply dividing the average count rate by the number of molecules. From this a relative brightness comparison can be made between single and dual laser excitation.

A solution of Ag-710 was diluted by a factor of 1 to 5000 resulting in approximately one molecule in the focal volume on average. The sample was initially monitored under just 633 nm excitation (4 kW/cm^2) and afterwards was simultaneously

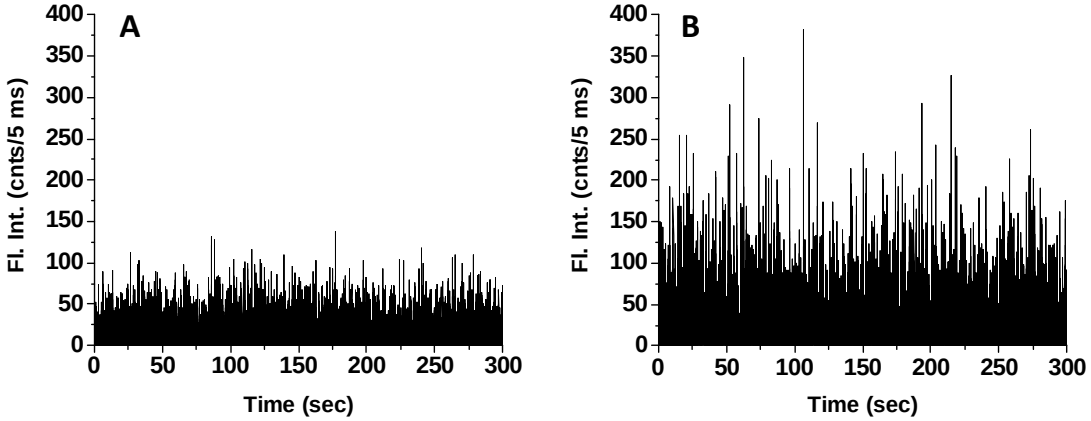

Figure 5.5. A. FCS time trace showing burst heights under single laser 633 nm excitation (4 kW/cm^2). B. FCS time trace showing burst heights under dual laser excitiong with simultaneous 805 nm excitation (10 kW/cm^2).

exposed to 805 nm secondary laser (10 kW/cm^2), again extracting the number of molecules. This difference in brightness can be directly observed by binning the time trace at a fine enough resolution (5 ms) to reveal fluorescence intensity bursts due to individual molecules diffusing in and out of the focal volume. Figure 5.5 A & B show the burst heights from single laser excitation and dual laser excitation, respectively. Individual burst heights average approximately 75 (cnts/5ms) when exposed to just one laser, but jump up 225 (cnts/5ms) once exposed to the second laser, resulting in a 3 fold increase in fluorescence brightness. The corresponding brightness per molecule calculation for this sample showed an increase from ~1200 to ~3600 counts per molecule in the presence of the second laser, agreeing well with the burst height analysis. The photobrightening originally observed in PVA films is also readily conveyed to Ag nanoclusters in solution. While some individual molecules in PVA exhibited as much as 6-fold enhancement, molecules in solution reached a maximum of 3-fold enhancement. This disparity is likely due to two main factors- the enhancement in solution is averaged over many molecules and the polarization is no longer optimized for diffusing molecules.

Efficient repopulation of the emissive state should reverse the premature saturation seen as a result of the long lifetime of the dark state. Saturation causes a sub-linear response to the excitation intensity, where the expected emission rates are not proportional to the increase in the excitation intensity. Rapid depopulation of the dark state should at least partially recover the expected linearity in the emission rate. Plotting the primary laser intensity (633 nm) versus the brightness per molecule, calculated from FCS measurements, shows the onset of saturation at 4 kW/cm^2 (figure 5.6 black).

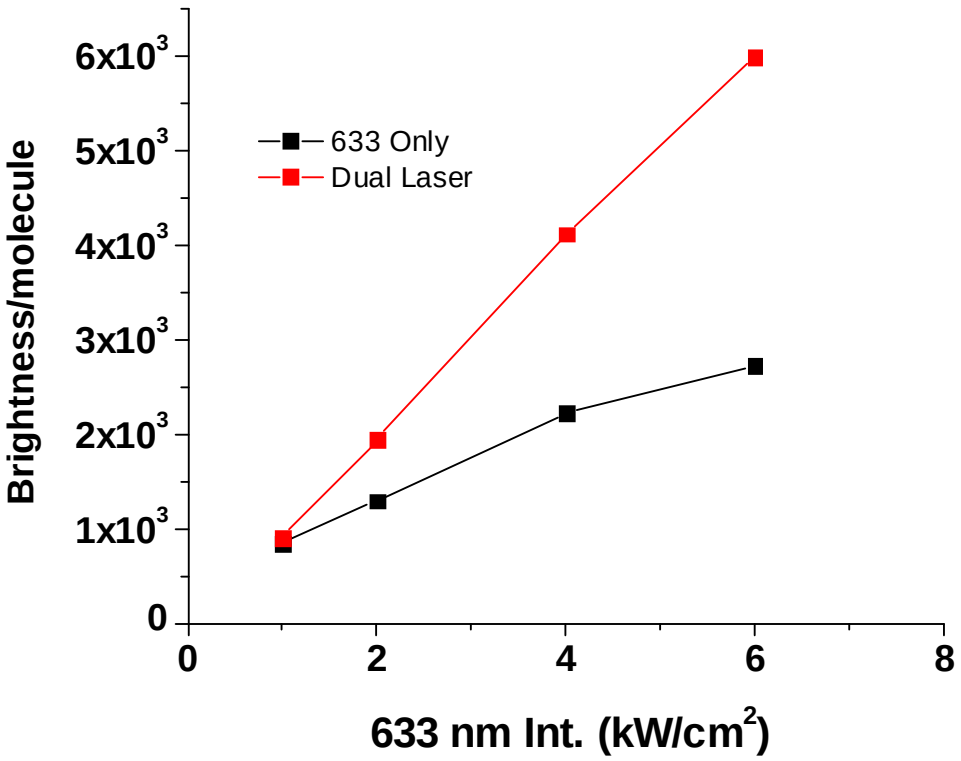

Figure 5.6. Brightness per molecule plotted vs the primary laser intensity for single laser excitation (black) and with simultaneous secondary laser excitation at 805 nm (8 kW/cm^2) (red).

Beyond this relatively low excitation intensity, little emission is gained from increasing the laser intensity. Under simultaneous secondary laser excitation (805 nm, 8 kW/cm^2) the brightness per molecule data shows a recovery of the expected linearity with no obvious saturation out to 6 kW/cm^2.

These results suggest that depopulation of the dark state occurs so efficiently that the residence time in the dark state is pushed to faster time scales rendering it insignificant. Furthermore, the enhancement seen in FCS experiments suggests that dynamic photobrightening could be feasible in biological imaging. It should be noted, however, that in FCS individual molecules are in the focal volume for a relatively short time (< 1ms), thus long term photobleaching measurements are not possible. While initial experiments are promising, additional characterization in relevant conditions is required.

5.5 Dual Laser Correlation Analysis

While these previous studies strongly suggest that Ag nanocluster fluorescence enhancement originates from a dark state shortening, correlation analysis can be used to directly extract changes in the off time between single and dual laser excitation for verification. Similar to the off time extraction illustrated in chapter 4, single Ag-710 molecules were isolated in PVA films and excited initially with a 633 nm laser and then with a simultaneous 805 nm secondary laser. Recording intensity versus time data, single molecule trajectories were initially collected with just 633 nm excitation (1.8 kW/cm^2). An autocorrelation of this data exhibited the expected microsecond decay similar to previous studies (Figure 5.7A black). Exposing the same molecule to the secondary laser

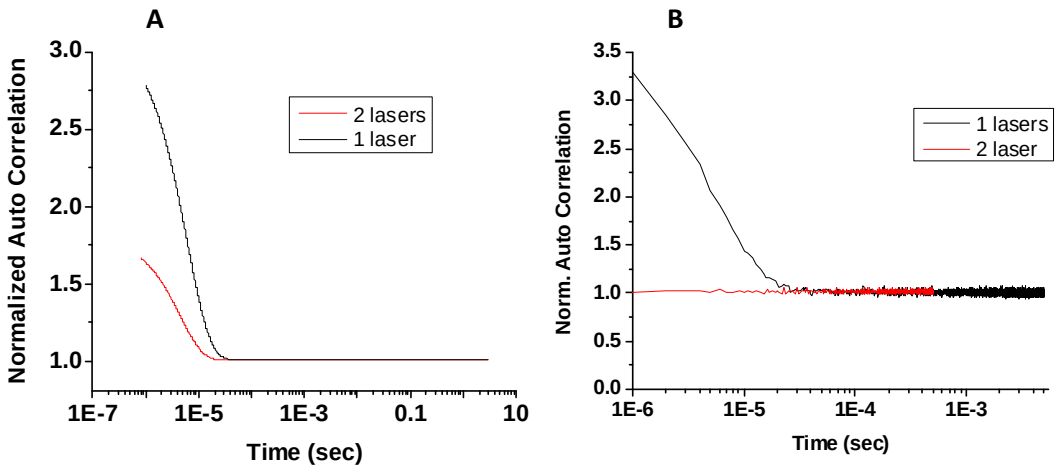

Figure 5.7. A. Autocorrelation from a single molecule time trace from 633 nm excitation (1.8 kW/cm^2) (black) and the autocorrelation from the same molecule while also being exposed to 805 nm secondary excitation (700 W/cm^2) (red). B. Autocorrelation of a time trace under 633 nm excitation (1.8 kW/cm^2) (black) and the autocorrelation from the time trace during exposure to 4 kW/cm^2 805 nm excitation (red).

at a relatively low intensity, 700 W/cm^2, additional time trace data was collected. The autocorrelation of the dual laser time trace showed significant changes compared to its single laser counterpart (Figure 5.7A red). In correlation analysis, the amplitude of the decay corresponds to the relative population in the dark state, and the decay time is indicative of the time scale of the intermittency. The decrease in the autocorrelation decay from the black to the red curve suggests a decrease in the population of the dark state tied to rapid depopulation. Additionally the slight shift to a faster decay time also indicates a shorter dark state lifetime. The extracted on and off times (Equations 4.2-4.5) for the single laser time trace were 8.9 μs and 18.7 μs, respectively. These values are typical for single laser excitation of Ag nanoclusters as seen in chapter 4. Extraction of the dual laser components show that the on time remained virtually unchanged, while the off time decreased to 7.9 μs. Clearly, the increase in the emission rate is accompanied by a corresponding reduction in the off time verifying that enhancement is tied to depopulation of the dark state. Additional data was collected comparing single molecule autocorrelations with higher secondary laser intensities (4 kW/cm^2). While the single laser correlation is similar to that seen in 5.7A, the dual laser correlation now shows a flat line indicating no apparent decay in the microsecond time regime (Figure 5.7B). This suggests the rapid depopulation has pushed the residence time in the dark state to much faster time regimes than can be measured in our experimental setup.

5.6 Optical Modulation

Fluorescence enhancement in both single molecule and bulk imaging applications will naturally lead to increased imaging sensitivity. Such gains, while useful, are not

sufficient to address all sensitivity issues related to imaging subcellular components, particularly those involving low copy number proteins or single molecule measurements. Dynamic photobrightening, however, could potentially provide even larger sensitivity gains then seen from just increasing fluorophore brightness. At the single molecule level, photobrightening is simply the result of increasing the average time in the emissive manifold through a decrease in the dark state. Analogously, at the ensemble level, we can view photobrightening as simply increasing the probability of the fluorophore population residing in the emissive manifold. The synchronous application of a secondary laser, that serves to depopulate the dark state, should result in an enhanced fluorescence signal at a specific and regular frequency. Regular modulated signals could then be directly extracted using signal processing techniques.

Turning the secondary laser on and off effectively modulates the enhancement by causing the fluorescence signal to alternate between the low and high levels of fluorescence at the same frequency as secondary laser exposure. The modulation frequency is then only limited by the fundamental on and off times of the Ag nanocluster system. Where if the modulation approaches the time frame of a complete on and off cycle for the dark state, the modulation frequency is obscured as the system cannot respond. The response time of the fluorescence system is directly linked to a combination of the off and on times. While intuitive for single molecules, the concept of off and on times is less obvious for bulk samples where this process can be viewed as the modification of the probability of occupation of the emissive manifold.

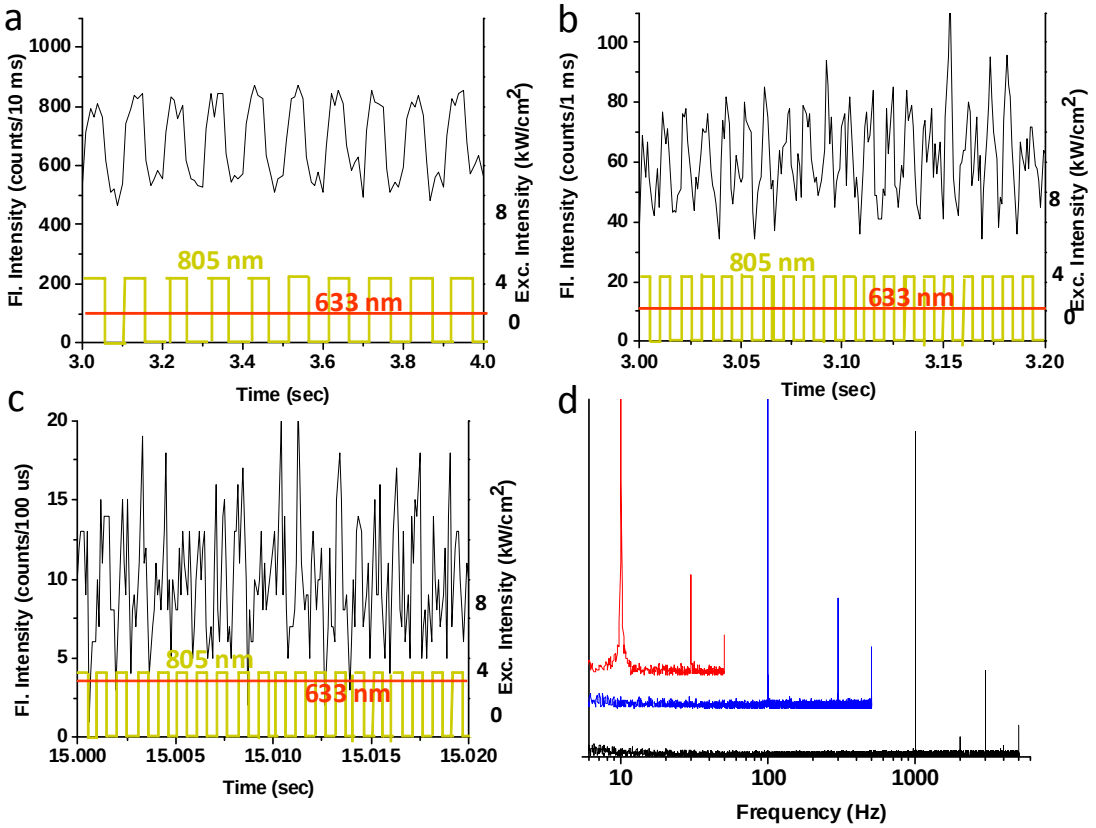

Figure 5.8. PVA-immobilized Ag nanodot emission under constant 633 nm excitation and 805nm excitation modulated at (A) 10, (B) 100, and (C) 1000 Hz. (D) Fourier transforms of the emission in (A-C) (red, blue, and green, respectively),each binned an order of magnitude faster than the modulation.

Using a PVA immobilized sample of Ag-710 where several molecules were in the focus of the laser at the same time, the response of the enhancement to the varied modulation frequencies was tested for time scales ranging from several hertz to 1 kHz (figure 5.8). The modulation frequency can clearly be seen in the fluorescence time traces, where the lower emission levels correspond to just 633 nm excitation (1.6 kW/cm^2) and the higher levels to simultaneous 805 nm excitation (4 kW/cm^2) (Figure 5.8a-c). At all frequencies, single laser excitation yields ~60,000 detected photons per second, while simultaneous illumination at 805 nm results in increased fluorescence. A key here is that the modulation resulted in dynamic photobrightening, where the enhancement alternated between high and low levels perfectly in phase with secondary laser exposure. In all cases the primary and secondary lasers were kept at the same intensities. The modulation frequency, thus, can be explicitly controlled through changing the laser chopping frequency without the necessity of increasing the laser intensity.

To verify that the laser modulation frequency was imprinted on the fluorescence waveform, the frequency components of each data set was analyzed. Fourier transforms of the resulting time traces reveal the original laser modulation frequency in each case: 10, 100 or 1000 Hz, corresponding to Fig 5.8A, 5.8B, and 5.8C, respectively. Perhaps the most interesting aspect of controlling the modulation frequency is that it allows for specific tuning of the fluorescence waveform based on experimental parameters. For example, biological systems exhibit dynamics across a wide range of timescales, thus the capability of shifting the modulation frequency away from these dynamics increases the potential scope of this technique.

5.7 Synchronous Modulation Image Extraction

Periodically amplifying fluorescence signals, such that photobrightening occurs at regular intervals, should allow selective signal extraction through lock-in type detection. Recently, Marriott and coworkers demonstrated that photoswitchable dyes, with thermally stable dark states, can be turned off and then on with sequential dual laser excitation resulting in regular modulation of the fluorescent signal.[176,177] In contrast to dynamic modulation, this technique employed a rather slow switching process. Additionally, the rate of switching to and from the dark state was dependent on the laser intensity, and as the waveform was not externally applied it had to be monitored with a separate internal control, complicating both image collection and processing. Creation of the proper fluorescence waveform required near complete photobleaching of all the molecules and then subsequent recover with a higher energy secondary laser. The limitations of this technique stem from the photophysical properties of the fluorophore and include background generating high-energy secondary excitation, a slow switching mechanism, alternate rather than simultaneous application of excitation lasers, and a lack of external control over the modulation cycle.

The dynamic photobrightening exhibited by Ag nanoclusters should allow for their selective enhancement and extraction. Thus, images that contain an amplified signal, even buried within a large background, can be delineated simply by identification of those pixels which exhibit the requisite waveform. Fourier analysis, $F(v) = \int_{-\infty}^{\infty} f(t)e^{2\pi ivt}dt$, of each pixel will be able select fluorescence related to the target signal versus those related to the background. Those pixels containing no regular frequency component will show up in the zero frequency component, while those containing target

fluorescence will be shifted to the frequency of the modulation. The signal which was completely obscured in the time based data is now revealed creating a digital signal processing detection system for each individual pixel.

Cy5, which emits at a similar wavelength as Ag-710, was used to create an artificially large background by which to test nanocluster signal extraction. Ag-710 was immobilized in a PVA film and place on top of a coverslip containing a 15-μM solution of Cy5. Exciting the Ag nanoclusters, by focusing 633 nm (3kW/cm^2) light on to the film through the cy5 solution and detecting with a ccd camera in an epifluorescence arrangement, resulted in an image showing a large fluorescent area mainly due to out of focus fluorescence from cy5 (Figure 5.9A). Simultaneously, an 805 nm laser (2 kW/cm^2) was focused onto the nanocluster sample and modulated at 10Hz while the frame rate of the camera was set at 100 Hz. A time trace was reconstructed for each pixel from the series of frames taken at 100 Hz and a Fourier transform of the resulting time trace was used to monitor for the frequency component matching the modulated laser. Plotting the amplitude at 10 Hz for each pixel resulted in the demodulated image where the cy5 fluorescence was completely eliminated (Figure 5.9B).

Examination of the time trace from a pixel under dual laser illumination shows a steady fluorescence at approximately 60,000 counts/pixel with a regular waveform imposed by the modulated secondary laser of about 2% of the base fluorescence. The recovered image is roughly the same size (4 pixels FWHM) as the 805 nm laser spot size, demonstrating background elimination through demodulated signal recovery. This illustrates that even relatively low emission on top of a large background can readily be extracted upon demodulation and averaging over several modulation cycles. Thus, the

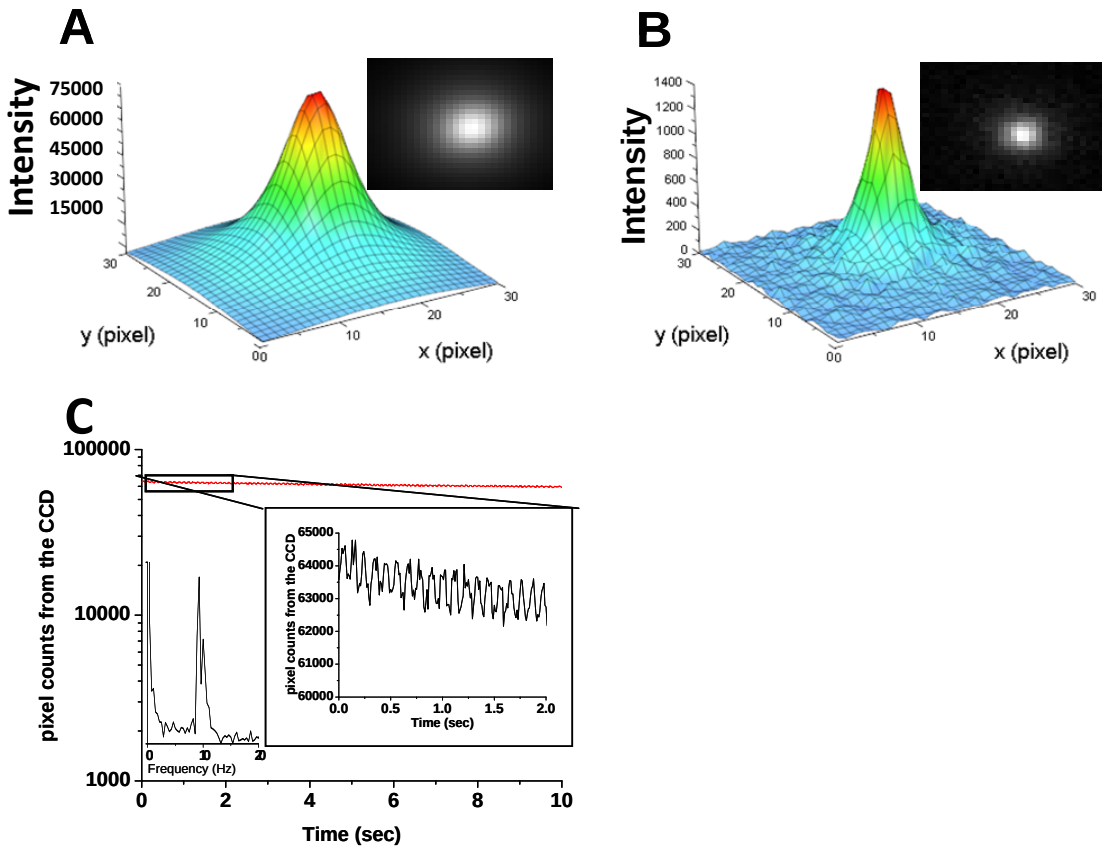

Figure 5.9. PVA immobilized Ag-710 imaged through a 15 µM Cy5 solution with constant defocused 633 nm excitation (3 kW/cm2) and optically chopped and focused 805 nm excitation (2 kW/cm2). (A) 3D plot of a typical raw 10 ms exposure ccd frame. Inset: raw 2D ccd image. (B) 3D plot of the demodulated signal recovering only the Ag nanocluster signal. Inset: raw 2D ccd image. C Time trace of an individual pixel for 10 sec with **insets** of (right) a zoomed in region of the time trace revealing the modulated intensity (from Ag nanodots) over the high Cy5 background and (left) the Fourier transform of the same time trace showing the modulation frequency component.

concept of fluorescence based modulated signal extraction was nicely demonstrated and shows great promise for potential applications in similar high background environments.

5.8 Synchronous Modulation Image Extraction of Single Molecules

As bulk signals were readily extracted from extremely high background, single molecule extraction should also be feasible. Given the nature of the detection system, ccd camera, and the presence of background generated photons, verification of single molecule detection is challenging. Due to the dipolar nature of the emission, single molecules exhibit a sine squared intensity distribution about the dipole. These emission patterns, characteristic of single molecules, can be visualized with ccd camera detection. In order to demonstrate single molecule signal extraction from high background, a sample containing 200 nM cy5 and 500 pM Ag-710 was immobilized in PVA by spin coating onto a coverslip. The concentration of Ag-710 was sufficiently low such that individual molecules were well spaced throughout the film. Using an identical procedure to that outlined for the bulk sample, images of the sample were taking at 40 Hz while illuminating with constant 633 nm (800 W/cm^2) and modulated the 805 nm (6 kW/cm^2) laser at 4 Hz. Raw images of the entire illuminated area show a rather uniform intensity across the image with no apparent single molecules visible (Figure 5.10A). Upon demodulation, sharp structures were observed in the demodulated image (figure 5.10B). The pixel size of these structures suggests that they are single molecules, but definitive identification in this environment is not feasible. Therefore, separate samples of Ag-710 (~500pM) and cy5 (200 nM) were immobilized in PVA and each was imaged with

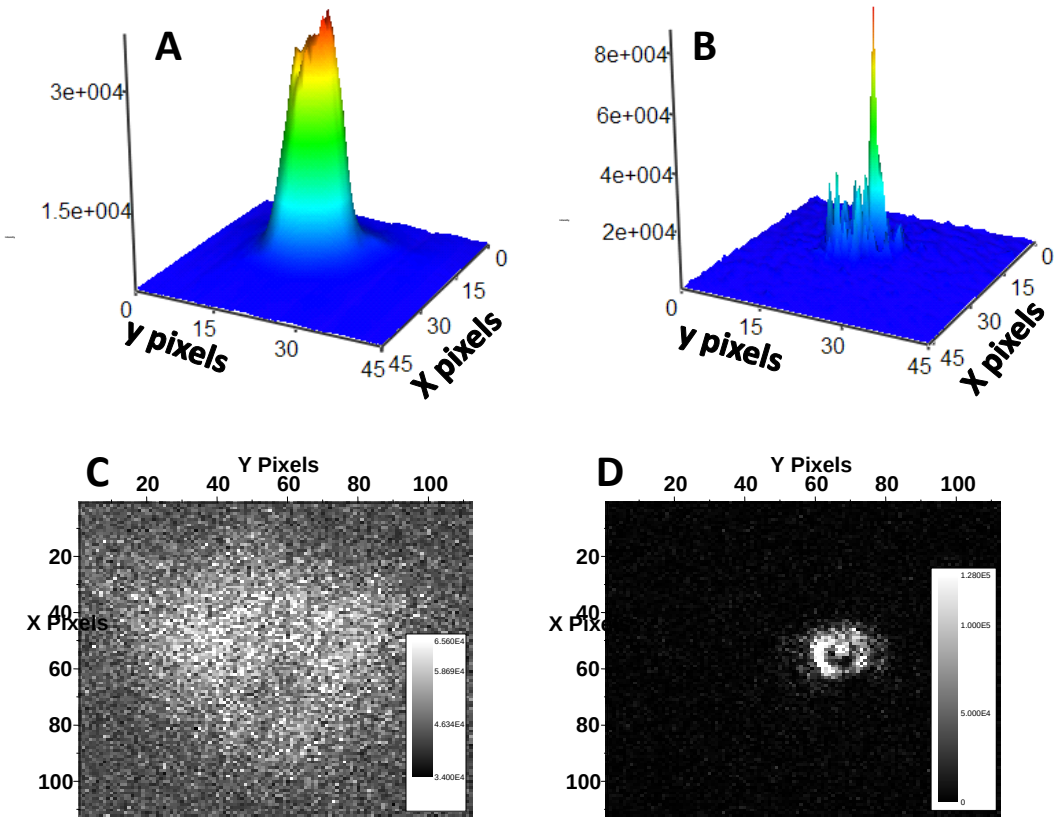

Figure 5.10. A. Raw image of a PVA immobilized sample composed of both cy5 and low concentration Ag-710 excited with constant 633 nm (800 W/cm^2) and modulated 805 nm (6 kW/cm^2) laser at 4 Hz. B. Demodulated image of (A) showing sharp spikes corresponding to single molecules. C. Raw image of combined separate images of cy5 and Ag-710 immobilized in PVA both excited with constant 633 nm (2 kW/cm^2) and modulated 805 nm (6 kW/cm^2) laser at 4 Hz. D. Demodulated image of (C) showing the recovery of a Ag-710 dipole emission pattern.

constant 633 nm (2 kW/cm^2) excitation and modulated (4 Hz) 805 nm excitation (6 kW/cm^2). The cy5 sample exhibited only a bright homogeneous background while the Ag-710 sample, with proper focusing, showed a dipole emission pattern from a single molecule. These two separate data sets were added together where the resulting combined image completely obscured the dipole emission pattern (Figure 5.10C). Subsequent demodulation readily recovers the original dipole emission verifying the extraction of single molecule signals from obscuring backgrounds (Figure 5.10D).

5.9 Conclusion

The extension of signal processing techniques to fluorescence imaging represents an important advancement in overcoming complications related to limited sensitivity in biological imaging. Both probe brightness and inherent background fluorescence inhibit many applications involving ensemble and single molecule imaging of subcellular components. We have explored unique photophysical behavior of Ag nanoclusters that enable the optical depopulation of long lived dark states. Blinking suppresses emission rates through premature saturation, limiting fluorophore brightness, but rapid depopulation of the dark state reduces residence times reversing this detrimental behavior. This process can be used to dynamically modulate Ag nanocluster fluorescence, leading to an entirely new high sensitivity imaging technique. Even at low intensities relative to the overall background fluorescence, Ag nanoclusters signals can be readily extracted, allowing recovery of the original features illuminated by dual laser excitation.

While Ag nanocluster based imaging may be potentially relevant to many biological applications suffering from poor sensitivity, several challenges remain. Complete characterization of these fluorophores, particularly a thorough understanding of how they behave in cellular environments, needs to be completed before they can be widely implemented in bioapplications.

CHAPTER 6
SIGNAL EXTRACTION OF ALTERNATE SYSTEMS

6.1 Introduction

The extension of high sensitivity imaging techniques developed for Ag nanoclusters to other more widely used organic probes, would greatly increase its potential application in biological imaging. Relying on the depopulation of intrinsic dark states, potential fluorophores would have to exhibit some of the distinct photophysical properties seen in Ag nanoclusters. While still widely viewed as detrimental, the selective population and depopulation of dark states has recently been advantageously employed in a number of new imaging techniques which focus primarily on improving spatial resolution.[16,178,179] Utilizing fluorescent systems with thermally stable dark states, most applications rely on serial location of single molecules for high resolution imaging. The behavior of these systems provides some context for the application of signal modulation. Under laser excitation, these fluorophores exhibit typical emission until transitioning into a permanent off (dark) state. These non-fluorescent states are optically depopulated through photoisomerization with exposure to higher energy secondary excitation, transitioning the molecule back to the emissive state. Serial location techniques, initially pioneered in the use of stochastic optical reconstruction microscopy (STORM)[178] and photo-activated localization microscopy (PALM)[16,179] use the stochastic nature of fluorophore switching to randomly populate the sample with a small number of single molecules. A high resolution mapping of the entire imaged structure is achieved by successively marking the location of single molecules as they become fluorescent. These techniques require sequential alternating exposure to the two lasers, and they are also

dependent on the excitation intensity of both lasers to control the rate of molecules transitioning into and out of the dark state.

More relevant to optical modulation, Marriott and coworkers have extended the use of photoswitchable dyes to high sensitivity imaging through the development of optical lock-in detection (OLID).[176,177] Similar to the serial location techniques, here fluorophores are also driven in to a dark state and then optically recovered with higher energy secondary excitation. Exposing the sample to sufficient intensity and duration of the primary laser, results in the switching of nearly the entire population of fluorophores. Repeating this process for multiple cycles then imprints a regular frequency onto the fluorescence signal which can be used for targeted extraction. This results in a similar fluorescence signal to that shown for Ag nanocluster modulation. While a regular waveform is established, it is not, however, based on an externally controlled frequency and as such an internal standard needs to be simultaneously measured to extract the modulated component. The use of photoswitchable fluorescent systems involves a number of other limitations as well. The secondary laser works at higher energy than the emission so both lasers cannot be operated simultaneously. Requiring that nearly the whole population is pushed back and forth between the states on each cycle, OLID is a much slower process than demonstrated for Ag nanoclusters. While certainly a useful technique for imaging static structures, in its present form OLID does not have the capability to resolve dynamics even on relatively slow time scales. Photoswitchable dyes with thermally stable dark states appear to be poor candidates for optical modulation.

Dynamic control of the modulation frequency exhibited with Ag nanoclusters is a direct result of the transient nature of the dark state which naturally decays on a

microsecond time scale. This allows for the regular transition between two different fluorescence levels where the system is continuously emitting just at a higher rate in the presence of the lower energy secondary laser. In contrast to photoswitches where the rate of transition between off and on states is dependent on the laser intensities, modulation frequencies using meta-stable dark states follow the waveform of the externally applied laser with complete independence from the laser intensity. Extending signal extraction techniques beyond Ag nanoclusters, will ideally involve the development of fluorescent systems with these naturally decaying dark states. In order to generate enhancement, dark states also need to be optically accessible, such that exposure to lower energy excitation drives the molecule back to the emissive state faster than natural decay.

Existing literature on dyes that show photobrightening via optical depopulation of the dark state is quite limited. The most thorough investigation was carried out by Eggeling and coworkers who evaluated the photobrightening capability of several fluorophores.[175] A number of interesting results were seen. They found that several dyes readily exhibited some type fluorescence enhancement when embedded in a polymer film, albeit only with secondary laser intensities exceeding MW/cm^2 (3 orders of magnitude higher than Ag nanoclusters). When the dyes were studied in aqueous solution the vast majority showed no enhancement at all with the exceptions of FITC (10% enhancement) and EYFP (5% enhancement) both at MW/cm^2 intensities. The high intensities needed for these fluorophores to exhibit photobrightening not surprisingly resulted in very rapid photobleaching. As the selection process of dyes for modulation based imaging will require the analysis of many fluorescent systems, clearly the development of a standard set of screening criteria would help facilitate identification.

6.2 Xanthene Dye Systems

Xanthene dyes with heavy atom ring substitutions typically exhibit very efficient population of a triplet dark state. Rose bengal, erythrosine b, and eosin y all fit into this category with triplet quantum yields of .98,[180] .90,[181] and .56,[181] respectively. Such large triplet quantum yields result in very short on times diminishing the fluorescence quantum yield, therefore all three are exceptionally poor fluorophores for imaging. Despite its limited application in imaging, rose bengal in particular has been fairly well characterized and has been shown to exhibit a rather large triplet state absorption cross section (~10^{-16} cm^2) in the visible range.[182] The large relative population and long lived lifetime of the triplet state could potentially lend itself to optical depopulation and give some insight into the photophysical properties governing the processes leading to efficient photobrightening.

In order to determine the optimum conditions for enhancement, initial studies were performed to ascertain the appropriate range of wavelengths for secondary excitation. Exciting a 10 μM solution of rose bengal with a constant primary laser (530 nm at 30 W/cm^2), the secondary wavelength (350 kW/cm^2) was scanned from 725 nm to 975 nm. An excitation scan was constructed by plotting the enhancement factor versus the secondary wavelength, showing a resonance near 900 nm and significant enhancement ranging from 800 nm to 950 nm (Figure 6.1A). This curve simply represents the propensity of the dye to revert from the dark state back to the emissive state. The reverse transition is based on an action cross section defined as the absorption cross section times the quantum yield for crossing from the triplet to the singlet state, for that reason previous transient absorption studies do not reflect the well defined resonance

as shown here. Most importantly these studies verify that photobrightening of rose bengal is feasible and can be accomplished via excitation at lower energy than the emission.

In order to determine the effect of the primary laser excitation intensity on the observed enhancement, experiments were performed at various 530 nm and 568 nm excitation intensities while under constant 800 nm secondary excitation (300 kW/cm^2) (Figure 6.1B). Higher primary laser excitation intensities should lead to more rapid depopulation of the singlet state, shortening τ_{on} and giving larger enhancement; however, this process is complicated by the already miniscule on time due to rose bengal's large triplet quantum yield (98%). So in this case only a moderate increase in the enhancement should be observed. Upon increasing the intensity of the primary laser, both for 530 nm and 568 nm excitation, the enhancement factor actually decreases significantly. In fact, enhancement is only observed at relatively low intensities (< 400 W/cm^2) (Figure 6.1B). Given the already efficient generation of the dark state and fundamental photophysical limits it is unlikely that the observed inverse intensity dependence is related to generation of the triplet state, suggesting the presence of other photo-induced transitions tied not to the on time but rather to the off time. The most likely cause is direct excitation out of the dark state via primary laser excitation. Inducing these transitions at such low intensities, the action cross section at the primary wavelength would have to be much larger than at the secondary wavelength. Comparing 530 nm versus 568 nm excitation shows slightly lower enhancement at the latter suggesting more efficient depopulation of the triplet state. In line with our experimental data, recently reported results show a very large action cross section for reverse intersystem crossing at 532 nm (~10^{-16} cm^2) on par with the

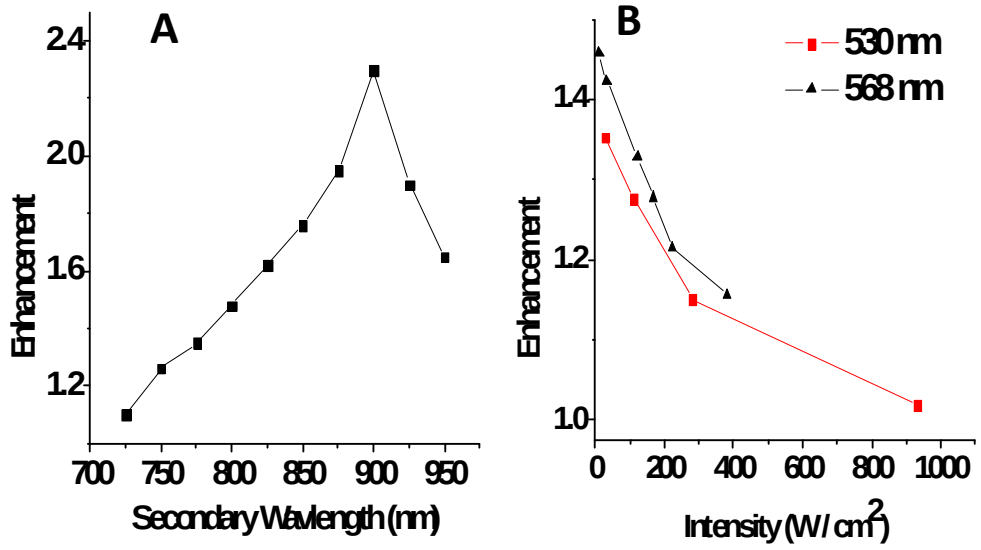

Figure 6.1. A. Secondary laser excitation scan at 350 kW/cm^{2}from 725 nm to 950 nm with continuous primary excitation at 530 nm (30 W/cm^2) showing enhancement above 800 nm with a resonance near 900 nm. B. Plot of 530 nm (red) and 568 nm (black) at increasing intensity vs enhancement factor with constant 805 nm (300 kW/cm^2) showing an enhancement at low intensities that decreases as the primary intensity increases.

singlet to singlet absorption cross section.[183] Such a competing process through simultaneous absorption of 530 nm light from the triplet ground state creates a major hindrance to the use of rose bengal for modulation based experiments.

6.3 Optimization of Rose Bengal Enhancement

To determine whether the primary laser was in fact simultaneously exciting the singlet transition and depopulating the dark state, a relatively low repetition rate (10 kHz) pulsed laser was used for primary excitation. At similar average intensities to those used for continuous wave (cw) excitation, with a constant secondary laser excitation (805 nm, 300 kW/cm^2), significantly larger enhancement was observed than previously seen with cw primary excitation (Figure 6.2A). Additionally, as the excitation intensity of the 532 nm laser was increased a corresponding increase in the enhancement was observed in contrast to what was seen with primary cw excitation (Figure 6.2A). The long time interval between primary laser pulses (~100 μs) coupled with sufficient intensity of the secondary laser ensures that the depopulation of the dark state arises solely from the lower energy excitation without any competition from the primary laser. The effect of the long interval between excitation pulses is further illustrated in the comparison of the intensity dependence of the secondary excitation under constant cw 530 nm (11 W/cm^2) and pulsed 532 nm (200 W/cm^2) primary excitation (Figure 6.2B). Due to the competing absorption, the maximum enhancement with 530 nm cw excitation is less than a factor of 2 and only approaches that value with secondary excitation intensities of ~600 kW/cm^2. Pulsed excitation yields 2 fold enhancement below 100 kW/cm^2 secondary laser intensity (Figure 6.2B) with maximum enhancements reaching a factor of 5. Eliminating the more

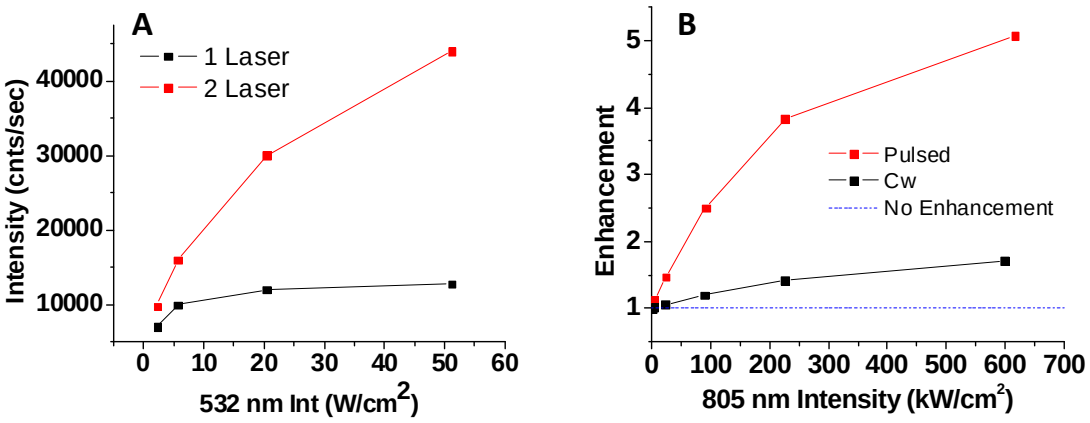

Figure 6.2. A. Plot of 532 nm pulsed excitation intensity vs. emission rate for single laser excitation (black) and dual laser excitation (red) (300 kW/cm^2) comparing the saturation levels showing a substantial increase in the fluorescence. B. Enhancement factor dependence on the 805 nm secondary laser intensity for cw (11 W/cm^2) and pulsed (200 W/cm^2) primary excitation.

efficient reverse intersystem crossing from the primary laser excitation allows for significantly lower secondary laser excitation intensities and larger overall enhancement as compared to single laser excitation. Desaturation of absorption due to low energy secondary laser excitation yields significant enhancement of bulk fluorescence by facilitating a larger population in the ground singlet state to be excited with the subsequent 532 nm pulse. The high rate of intersystem crossing reduces required primary intensities. Another consequence of the very efficient population of the dark state is a diminished fluorescence quantum yield (2%).

6.4 Erythrosin B & Eosin Y Enhancement

While enhancement of rose bengal illustrates the necessity of an efficient population of the dark state for photobrightening, in many ways it is a limiting example based on its weak overall fluorescence. Studying the photophysics of dyes in the same family, eosin y and erythrosin b, with moderately higher quantum yields should give further insight into the characteristics promoting optical enhancement. Initial experiments to test the photobrightening of erythrosin b showed similar results as rose bengal except with slightly lower levels of enhancement. On the other hand, secondary excitation (800 nm, 300 kW/cm^2) of eosin y not only resulted in no enhancement, but significant fluorescence dampening was seen where the fluorescence signal was reduced by as much as 50%. This sudden decrease in fluorescence is likely due to rapid photobleaching induced by populating more reactive high energy triplet states. Interestingly, similar behavior could also be induced in erythrosin b but only at very high secondary laser intensities (>800 kW/cm^2). This fits well with the results reported by

Eggeling for several dyes including eosin y.[175] As the presence of oxygen should facilitate the bleaching process, additional experiments were performed in an oxygen free environment by continuous flow of nitrogen through a sealed fluorescence observation chamber. Using these new conditions, a 1 μM solution of eosin y readily demonstrated fluorescence enhancement on exposure to the secondary laser. So adopting the proper conditions all three dyes can be photobrigthened, warranting a detailed comparison of the three. This should lead to a better understanding of how the specific photophysics demonstrated here affect enhancement properties.

As all three dyes have different intersystem crossing rates and fluorescence quantum yields, investigation of how the enhancement of each system is affected by the varying photophysics was performed. To minimize the effects of photobleaching, comparisons were made for deaerated samples of all dyes. Using 532 nm pulsed primary excitation (200 W/cm^2) in deoxygenated aqueous solutions, 6 fold rose bengal, 2 fold erythrosin b, and 1.1 fold eosin y enhancements were observed at identical secondary excitation intensities (Figure 6.3A). An identical experiment with aerated samples resulted in lower levels of enhancement for both rose bengal and erythrosin b, presumably from oxygen assisted photobleaching (Figure 6.3B). The large triplet quantum yield for rose bengal facilitates efficient population of the dark state even with an individual pulse of the primary laser. The other dyes with lower triplet quantum yields exhibit less efficient crossing to the dark state. Resulting in larger enhancement, rose bengal's efficient intersystem crossing, however, also leads to a lower fluorescence quantum yield. The dyes studied here follow an obvious trend where higher dark state

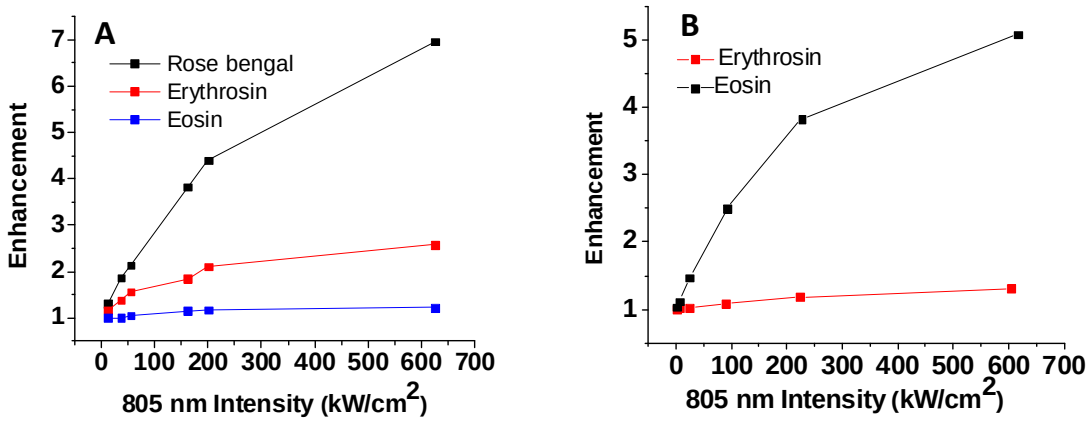

Figure 6.3. A. Enhancement dependence in a deoxygenated solution for rose bengal (black), erythrosin b (red), and eosin y (blue) on the 805 nm secondary laser intensity using 532-nm primary pulsed excitation (200 W/cm^2). B. Enhancement dependence in an aerated solution for rose bengal (black), erythrosin b (red) on the 805 nm secondary laser intensity using 532-nm primary pulsed excitation (200 W/cm^2).

quantum yields lead to larger enhancement factors. Clearly the formation efficiency and the long lifetime of that dark state (off time) are major factors in the determining a dyes capacity for fluorescence enhancement. These considerations, however, need to be taken in the context of overall fluorophore quality. The potential for significant enhancement in the presence of dominant dark state photophysics becomes detrimental if fluorophore emission rates are simultaneously constrained.

6.5 Modulation and Signal Extraction

All three of the xanthenes-based dyes showed at least moderate enhancement which should allow fluorescence modulation via secondary laser excitation. In order to determine the feasibility of signal modulation, each dye was simultaneously exposed to a constant primary laser and modulated secondary laser. Figure 6.4A shows the time trace from a 1 μM solution of eosin y in a nitrogen rich environment while exposed to a primary 530 nm laser (70 W/cm^2) and a secondary 805 nm laser (280 kW/cm^2) modulated at 1 kHz. A modulated component appears to be present in the emission, but given the high repetition rate it is difficult to determine the actual frequency. Taking a Fourier transform of the time trace, a clear peak is seen at 1 kHz indicating that the laser modulation has been imprinted on the fluorescence signal (Figure 6.4B). Rose bengal and erythrosin exhibited similar modulation in both aerated and deaerated conditions. Since fluorescence signals can readily be modulated in the presence of a chopped secondary laser, specific signal extraction should be feasible in the same fashion previously demonstrated with Ag nanoclusters.

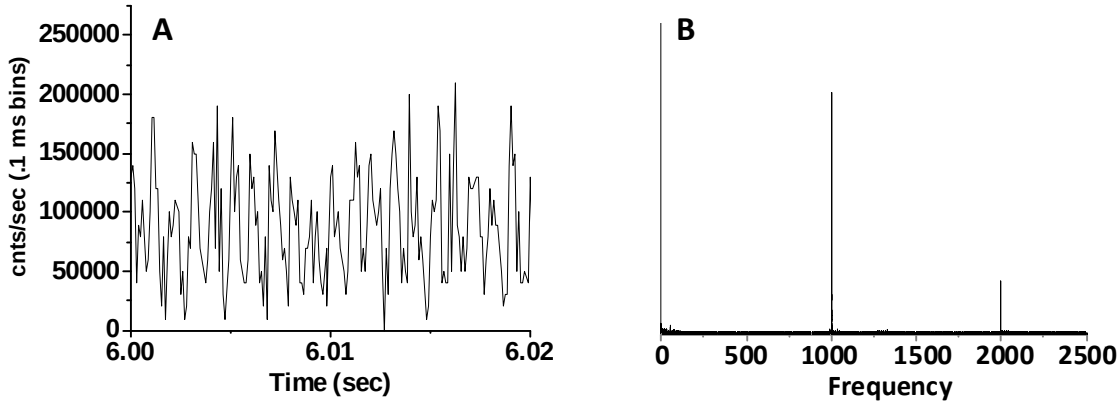

Figure 6.4 A. Time trace of deoxygenated 1 μM aqueous eosin Y with 530 nm (70 W/cm^2) and 805 nm excitation (280 kW/cm^2) modulated at 1000 Hz showing enhancement in phase with the modulation. B. Fourier transform of the time trace verifying the frequency component imposed on the fluorescence signal.

In order to verify that fluorophores with the general enhancement characteristics shown by these dyes are suitable for signal extraction, a simple demonstration was performed using rose bengal. A large area was illuminated with 530 nm primary excitation (50 W/cm^2), with a smaller secondary 805 nm laser (400 kW/cm^2) spot focused in the center of the larger 530 nm spot. A 3-dimensinal plot of an average frame from the raw data shows a nearly homogeneous fluorescent signal across the entire image (Figure 6.5A). The signal from dual laser exposure is slightly visible is slightly visible with the high background as indicated by the arrow in figure 6.5A. Upon demodulation by extracting the frequency component that matches the modulation frequency (2 Hz) for each pixel, only the ones simultaneously exposed to both lasers are revealed while all others are eliminated. The 70 pixel wide feature in the raw image is reduced to a 5 pixel wide area matching the size of the 805 nm laser. The barely discernible shoulder in the raw image is now the only feature in the demodulated image. The Fourier transfer of a time trace of a pixel from the area exposed to the 530 nm laser (Figure 6.5C) shows no obvious frequency component, however, the Fourier transform of a pixel simultaneously exposed to both lasers (Figure 6.5D) shows that modulation (2 Hz) is clearly imposed on the pixels with dual laser excitation but not in the other. This nicely demonstrates that a signal which was seemingly buried within large background fluorescence can be extracted simply by selectively modulating the desired signal. In order to quantify the actual background elimination, the intensity of a pixel in the area illuminated by two lasers was compared to a corresponding pixel from single laser illumination. In the average image, a typical dual-laser-illuminated pixel (inset 6.5D) showed a modulated

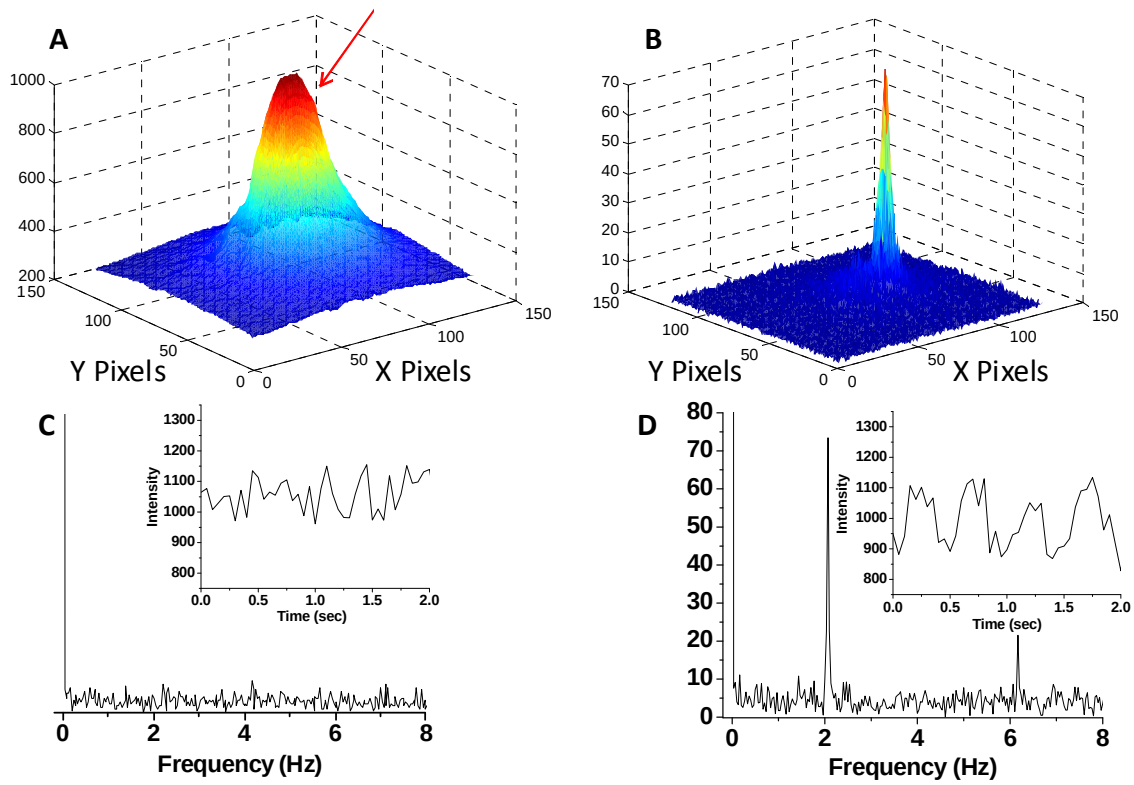

Figure 6.5. A. Raw 3-dimensional plot of an individual frame of rose bengal solution fluorescence with defocused 530 nm excitation (~50 W/cm^2) and tightly focused 805 nm co-excitation (400 kW/cm^2) modulated at 2 Hz, coupled with synchronous ccd detection at 20 Hz. B. Demodulated 3-dimensional plot showing the extraction of the signal from the pixels that are simultaneously exposed to both lasers. C. Fourier transform of a fluorescence trajectory from an area only exposed to the 530 nm laser (no modulated component). D. Fourier transform of a fluorescence trajectory from an area exposed to both lasers showing the 2 Hz frequency matching the modulation frequency.

signal amplitude of A~71 counts (based on the amplitude of the 2-Hz component in the Fourier transform, Fig. 6.5D). With a background of ~1000 counts, the signal (6.5C) to background ratio is ~0.14. For the demodulated image the modulated signal amplitude, A, is ~71 but now the background has been reduced to ~4 counts, yielding a signal:background of ~18. Thus, as modulation depth is the crucial parameter for signal extraction, even these weakly emitting dyes yield >100-fold improvements in signal visibility. The signal to noise improvement can be estimated in a similar fashion. The average counts during dual laser exposure are 1071, while single laser excitation gives an average count rate of 933, resulting in an enhancement of 138 counts. The noise estimated from the standard deviations of the enhanced and non-enhanced portions of the time trace were 47 and 44, respectively. Subtracting the single laser-excited background yields an estimated signal (138) to noise ($\sqrt{44^2 + 47^2} \sim 64$) of ~2.16. In the demodulated image, only the noise at the modulation frequency (2.1 counts) contributes (as estimated from standard deviation of the frequency dependent intensities in the Fourier transform), yielding a demodulated signal to noise of 71/2.1 ~34. This corresponds to a >15-fold signal to noise improvement over the averaged, background-subtracted image.

Despite their limited brightness which renders them poor biological imaging agents, these dyes nicely demonstrate the concept of improved sensitivity defining a general set of parameters for engineering and selecting more viable dyes. Clearly dark state absorption must be at lower energy than the collected fluorescence. This allows longer wavelength excitation to achieve fluorescence enhancement without generating any additional background. Thus, the secondary excitation waveform can be selectively applied only to the target fluorophore. Additionally, the dark state should have a finite

lifetime such that it naturally decays, repopulating the emissive state. In such systems the fluorophore is continuously emitting simply at a lower intensity level under one laser excitation and a higher level under dual laser excitation. The secondary laser can be used to regularly cycle between the two states without the need to transiently bleach the fluorophore such as with a photoswitchable dye. Resulting in complete dynamic control over the modulation frequency, the external laser drives the cycling frequency with absolutely no dependence on the actual laser intensity. The population of this dark state is also crucial. While the fluorophore must have relatively efficient crossing into the dark state, an abbreviated on time coupled with a long off time leads to significantly diminished fluorescence quantum yields. As discussed previously, the ratio of off and on times determines the potential enhancement factor where the on time is dependent on the probability of transitioning to the dark state. This ratio must be large enough to yield substantial enhancement (~3x), yet small enough to avoid severely limiting the fluorescence quantum yield. As the off time needs to be transiently shortened to induce modulation, optical depopulation of the dark state must also be highly efficient. This requires large action cross sections. Allowing for low secondary laser excitation intensities, efficient repopulation of the emissive manifold limits the required number of absorption cycles out of the lower level dark state. As demonstrated by the rapid photobleaching of eosin y during two laser excitation, higher energy excited states must be relatively non-reactive. Not only does this limit potential enhancement; bleaching also leads to signal degradation hindering biological characterization. Spectral overlap between absorption of the dark state and the primary excitation is also problematic. If the primary laser induces dark state depopulation, the off time is prematurely shortened

lowering the potential enhancement from the secondary laser. Thus, fluorophores should have complete spectral separation between the primary and the secondary absorption. Additionally, depopulating the dark state with near infrared excitation would be ideal as it results in lower background in general than exciting with higher energy visible light.

Despite their poor fluorescence quantum yield, these dyes were useful in determining the characteristics described above. From these results it is clear that complicated photophysical processes influence fluorescence enhancement. Few existing fluorophores are likely to exhibit the properties necessary for efficient optical modulation, which explains the uniqueness of Ag nanoclusters. The most direct path to an ideal fluorophore for signal modulation will involve engineered dyes based on an existing system that already exhibits a majority of the necessary criteria.

6.6 FRET-Based Fluorescence Enhancement

While fluorescence intermittency based on dark states shows potential, systems with engineered dark states based on easily managed parameters may be more ideal for optical modulation. It is useful to think of enhancement in general terms that can be applied to all fluorescent systems. The effect of fluorescence intermittency can be readily described by changes in the fluorescence quantum yield, where the fluorophores exhibit a lower quantum yield as the dark state is populated and higher quantum yield in the presence of a secondary laser. Analogously, donor emission in Forster resonance energy transfer (FRET) systems also exhibits a change in fluorescence quantum yield. The presence of an acceptor molecule lowers the donor emission rate (quantum yield) through energy

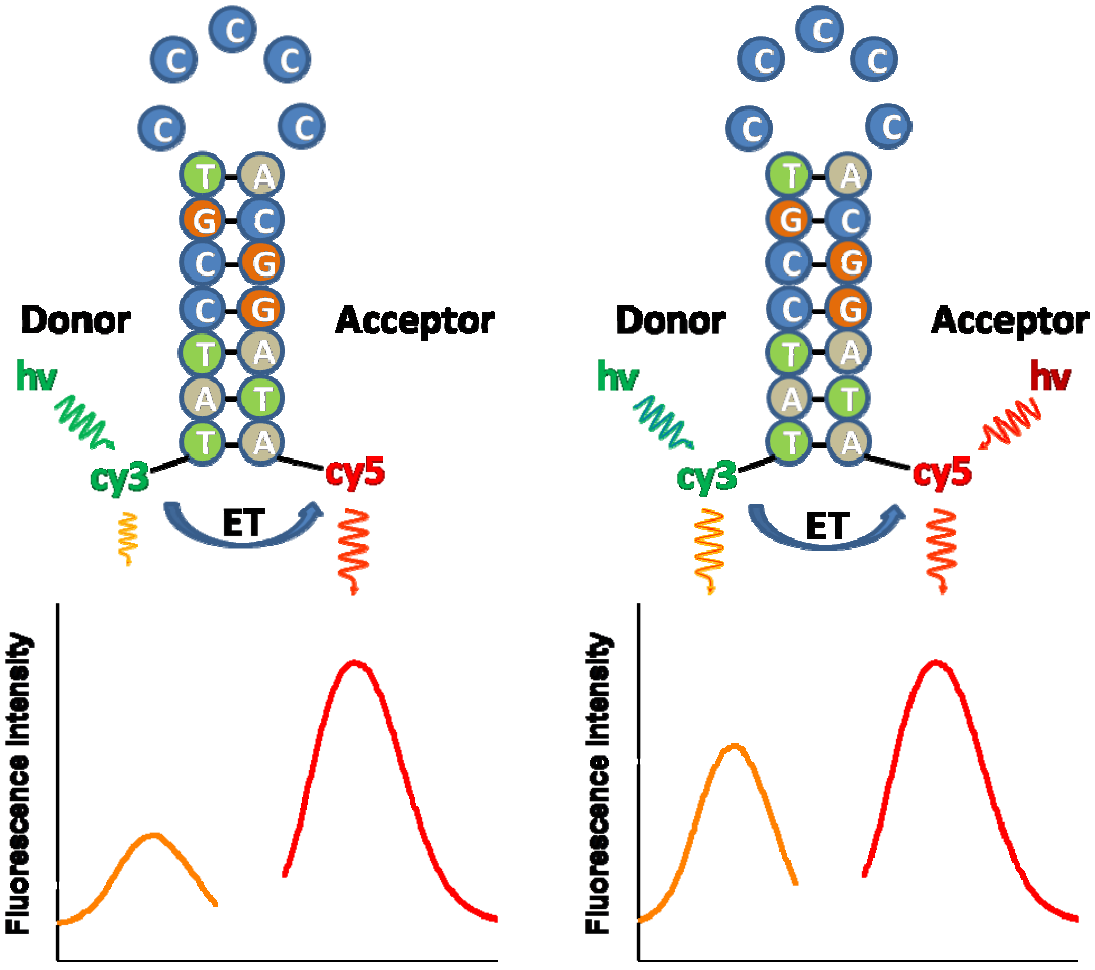

Figure 6.6. Schematic of a 19 base hairpin exhibiting FRET with a Cy3 donor and Cy5 acceptor. A. Typical FRET process when only the donor is excited, leading to highly quenched donor fluorescence. B. Inhibited FRET and increased donor fluorescence quantum yield resulting from simultaneous acceptor direct excitation that inhibits FRET through creating a higher steady state acceptor excited state population, thereby increasing, and enabling modulation of donor fluorescence.

transfer. Thus, any process that inhibits energy transfer would result in a corresponding increase in the donor emission. The level of potential donor enhancement is tied directly to the FRET efficiency. Theoretically, FRET systems could allow the donor fluorescence to range from near zero to the full typical emission all controlled by engineering the distance between the donor and acceptor. As the enhancement is linked to the increase in quantum yield, the maximum enhancement factor is also determined by FRET pair separation.

Donor to acceptor energy transfer can be blocked via direct excitation of the acceptor with a secondary laser. This alternate excitation leads to population of the acceptor excited state inhibiting the energy transfer pathway resulting in higher donor emission. This process has been successfully demonstrated for cyanine based dyes[137] as well as fluorescent proteins.[134,135] FRET based optical modulation could be used to circumvent several of the issues involved in the direct modulation of existing organic dyes. Bioimaging applications involving FRET are wide-spread and accessible with a variety of different fluorophores. Thus, nearly any fluorescent label could be incorporated into a signal modulation scheme dramatically expanding the scope of the technique. Additionally, enhancement with common fluorophores requires complex photophysical interactions involving dark state transitions which potentially diminish the dye's quantum yield. In contrast to this, FRET based systems maintain the inherent fluorescence quantum yield of the donor and are not subject to potential repeated dark state cycling prior to emission. The concept of FRET based modulation using a DNA hairpin structure with cy3 and cy5 is schematically outlined in figure 6.6. The proximity of the donor and acceptor should result in relatively large FRET efficiencies, advancing

the potential for large enhancement. Increasing the 570 nm donor emission, simultaneous exposure to the secondary laser on resonance with the acceptor excitation disrupts the energy transfer. As the secondary laser is at lower energy than the collected donor emission no additional background is generated.

6.7 Intensity-Dependent Enhancement

Inhibiting energy transfer is dependent on simultaneously populating the excited state of the acceptor and the donor such that the transfer pathway is no longer accessible. Given the relatively fast lifetimes of the excited state (~ns) for typical organic fluorophores, one would expect enhancement would only result from fairly high cw excitation rates. In order to estimate the required intensities and the potential enhancement, the behavior of FRET systems with two laser excitation was modeled. A state diagram was constructed depicting the various transitions populating and depopulating each state (Figure 6.7A). Included in the model are donor ground (D) and excited (D*) states, as well as acceptor ground (A), excited (A*). The dark states for the acceptor are also included and are indicated by (A^d). The symbol (k) indicates a rate where transitions into the excited state are represented by the subscript Exc and Fl denotes fluorescence. For typical FRET studies using single laser excitation, the donor is initially in the ground state (D) until an absorption event populates the excited state (D*). The molecule can then either emit a photon returning to (D) or undergo energy transfer populating (A*). The presence of a secondary laser creates an alternate pathway to populate (A*), resulting in a fairly complicated diagram with 6 separate states and multiple transitions between states.

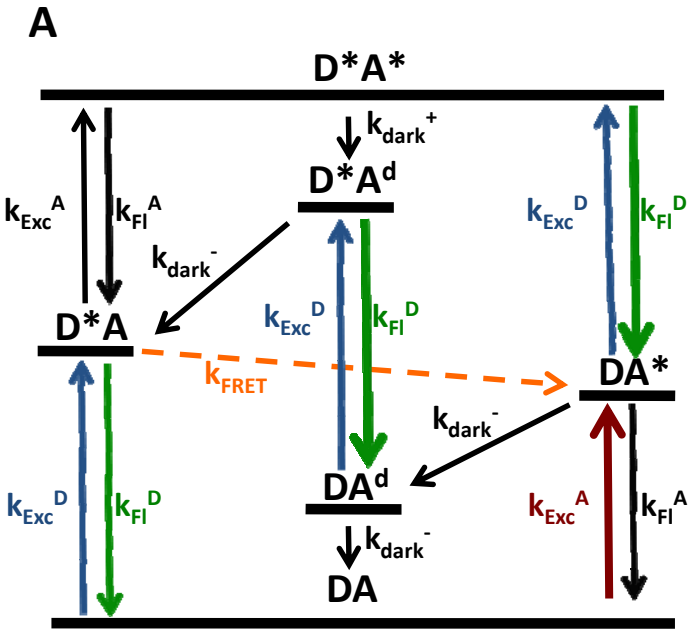

B

$$\frac{d}{dt}\begin{bmatrix} DA \\ D^{*}A \\ DA^{*} \\ D^{*}A^{*} \\ DA^{d} \\ D^{*}A^{d} \end{bmatrix} =$$

$$\begin{bmatrix} -(k_{Exc}^{D}+k_{Exc}^{A}) & k_{Fl}^{D} & k_{Fl}^{A} & 0 & k_{dark}^{-} & 0 \\ k_{Exc}^{D} & -(k_{Fl}^{D}+k_{Exc}^{A}+k_{FRET}) & 0 & k_{Fl}^{A} & 0 & k_{dark}^{-} \\ k_{Exc}^{A} & k_{FRET} & -(k_{Exc}^{D}+k_{Fl}^{A}+k_{dark}^{+}) & k_{Fl}^{D} & 0 & 0 \\ 0 & k_{Exc}^{A} & k_{Exc}^{D} & -(k_{Fl}^{D}+k_{Fl}^{A}+k_{dark}^{+}) & 0 & 0 \\ 0 & 0 & k_{dark}^{+} & 0 & -(k_{dark}^{-}+k_{Exc}^{D}) & k_{Fl}^{D} \\ 0 & 0 & 0 & k_{dark}^{+} & k_{Exc}^{D} & -(k_{Fl}^{D}+k_{dark}^{-}) \end{bmatrix} \begin{bmatrix} DA \\ D^{*}A \\ DA^{*} \\ D^{*}A^{*} \\ DA^{d} \\ D^{*}A^{d} \end{bmatrix}$$

Figure 6.7. A. Schematic model enabling donor fluorescence enhancement and modulation through dual laser excitation. B. Rate equations corresponding to population and depopulation of all 6 levels as diagrammed in A.

Excitation rates are defined as simply the absorption cross section (σ) multiplied by the excitation intensity (I), while fluorescence rates are determined by the inverse of the fluorescence lifetime**.** The energy transfer rate, k_{ET}, can be calculated from the fluorescence rate and the energy transfer efficiency, as depicted in equation 6.1

$$k_{\mathrm{ET}} = \mathrm{k_{Fl}}/(\frac{1}{\mathrm{E}} - 1) \qquad \text{Equation 6.1}$$

where the E represents the transfer efficiency. From this diagram a system of rate equations can be constructed that describe the population and depopulation of each of the states (Figure 6.7B). Solving this set of differential equations yields the relative steady state populations in each of the 6 states. In the presence of only donor excitation, the population of the acceptor excited and dark states are entirely dependent on energy transfer. The introduction of the secondary laser results in additional pathways for acceptor population. The steady state population of the acceptor excited state was solved for both the case of single and dual laser excitation. The rates of energy transfer and fluorescence of the donor (i.e. quantum yield) were solved for each case. Subsequently the calculated rate of fluorescence in the absence of a secondary laser divided by the corresponding rate under dual laser excitation yields the enhancement factor for a given set of paramaters.

For comparison, two separate FRET systems were chosen based on labeling opposite ends of the hairpin shown in Figure 6.6 (5'-**TAT CCG TCC CCC ACG GAT A**-3') with corresponding FRET pairs. The first system comprised of 6-Fam (6-carboxyfluorescein) on the 5’ end and TAMRA (tetramethyl rhodamine) to the 3’ end

was chosen because TAMRA is known to have a low dark state quantum yield (~.001) and short dark state lifetime (~10 μs).[184,185] Experimental studies of this system were then compared to the modeled data. Using a typical confocal setup, a 125 nM solution of 6-FAM/ TAMRA was exposed to constant 10 kW/cm^2 donor excitation while the secondary laser (561 nm) intensity was varied. A maximum enhancement of 60% was achieved at a 561 nm intensity of 100 kW/cm^2 (Figure 6.8A, black). Modeling the same system as described above, the photophysical parameters used for determining transitions between states for 6-fam-Tamra were λ_d = 476 nm, λ_a = 561 nm, $\square_{dark}$ = .001, τ_d = 3.5 ns, τ_a = 3.0 ns , E_{fret} = .90, τ_{dark}- = 10 μs, I_d = 10 kW/cm^2, ε_d= 60,000, ε_a = 50,000. The calculated intensities correspond quite well with the experimental data with both showing the same trend in response to increasing secondary laser intensities and similar maximum enhancement of ~60% (Figure 6.8A, red). A comparison of steady-state fluorescence from just the donor and the donor in the presence of the acceptor showed a FRET efficiency of ~90%. Analogous to the calculations for dark state transitions, the maximum potential enhancement for FRET based systems is represented by equation 6.2

$$Max\ Enhancement = \frac{1}{1-E} \qquad Equation\ 6.2$$

This gives 6-FAM/ TAMRA a 10 fold potential enhancement. Even at the high intensities used for these experiments, the enhancement never approached the maximum levels. While 6-FAM/TAMRA studies clearly demonstrate the feasibility of engineering FRET based signal enhancement, such high intensities would be prohibitive for biological experiments due to dye photobleaching, background generation, and sample

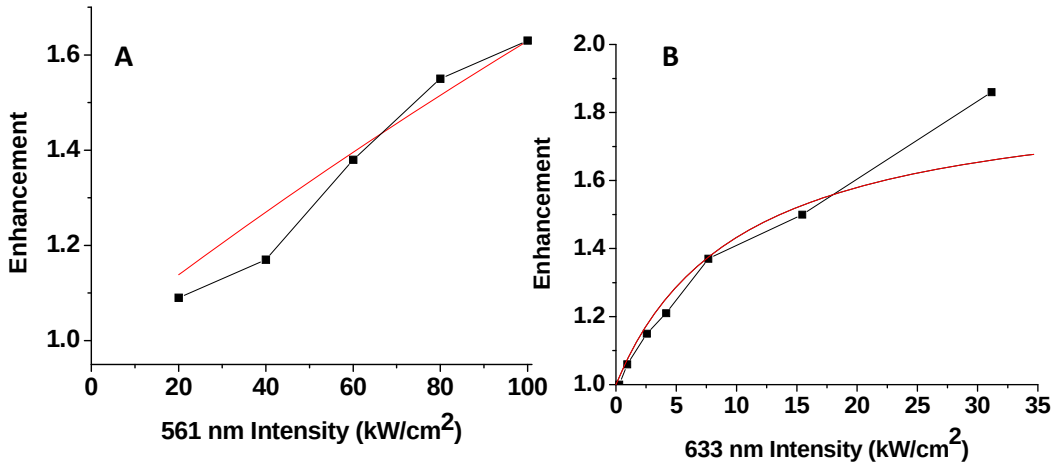

Figure 6.8. Predicted and experimental intensity dependence of donor fluorescence enhancement upon acceptor co-illumination. **A**. Predicted enhancement (red line) of a 6-Fam/TAMRA-labeled hairpin undergoing FRET (E_{FRET} measured at ~90%) with constant cw 476 nm (10 kW/cm^2) excitation and varied cw 561 nm intensity using a dark state quantum yield of 10^{-3} and dark state lifetime of 10 μs. Measured enhancement from a 125nM aqueous solution (black ■) with 476-nm (10 kW/cm^2) primary and varied 561-nm secondary excitation. **B**. Predicted enhancement (red line) of a Cy3/Cy5 hairpin exhibiting FRET (E_{FRET}~47%) with constant cw 496-nm (750 W/cm^2) primary excitation and varied cw 633-nm secondary excitation using an acceptor dark state quantum yield of $6x10^{-4}$ and dark state lifetime of 100 μs. Measured enhancement with constant 496-nm (750 W/cm^2) primary excitation and varied cw 633-nm secondary intensity (black ■)

survivability. More efficient enhancement requires either longer acceptor excited state lifetimes or more efficient excited state population.

As the population of any state that suppresses FRET should increase enhancement, the presence of a long lived acceptor dark state should inhibit energy transfer at much lower intensities. As cy5 has been reported to have a long lived dark state (~100 μs) resulting from cis-trans isomerization,[186,187] 6-FAM and TAMRA were replaced with cy3 and cy5 on an identical hairpin structure. To test their viability, this new set of dyes was modeled integrating the appropriate photophysical parameters, λ_d = 496 nm, λ_a = 633 nm, $\square_{dark}$ = .0006, τ_d = 3.5 ns, τ_a = 3.0 ns , E_{fret} = .47, τ_{dark}- = 100 μs, I_d = 1kW/cm^2, ε_d= 30,000, ε_a = 250,000. Remarkably, calculated results readily reached 90% enhancement at secondary intensities of only 30 kW/cm^2 (Figure 6.8B, red). With a measured FRET efficiency of 47%, this represents near maximum potential enhancement. Despite residing on the same hairpin structure, the efficiency shown here is lower than the 6-FAM/TAMRA system, likely resulting from a lower degree of spectral overlap. In order to verify these results experimentally, the secondary laser (633 nm) intensity dependence of a 1 μM solution was explored with constant 496 nm (1kW/cm^2) primary excitation.

Here the experimental data definitively reproduced the intensity dependence modeled using the photophysical properties of the acceptor and donor (Figure 6.8B, black). A slight variance at very high secondary excitation (> 30 kW/cm^2) is likely due to donor bleaching during the short transit time through the focal volume. Clearly the population of a long lived dark state (cy3-cy5) renders the molecule inaccessible to

energy transfer generating enhancements at lower secondary intensity than in the absence of such states (6-FAM-TAMRA).

6.8 Modulation and Signal Extraction Using FRET Systems

In systems where enhancement originates from dark state depopulation, maximum modulation frequencies are only restrained by off and on times. However, the limits on the modulation frequency of FRET systems are imposed by the lifetime of the dark state and the time needed to reach a steady state population of the dark state. As the modulation time approaches the timing of these two processes, the modulation depth should decrease until such a point where the secondary laser is modulating faster than the system has the ability to even partially recover. Using the rate model for the cy3/cy5 system, the modulation depth (i.e. enhancement factor) was calculated at increasing modulation frequencies. By limiting the duration of the secondary laser, the state steady state population of the dark state was reduced resulting in less inhibition of FRET (Figure 6.9, black). At frequencies near 4 kHz, the calculated enhancement fell from a high of 60% down to ~20%. To verify these results experimentally, a 1 μM solution of cy3/cy5 was simultaneously excited with a 496 nm laser (500 W/cm^2) and a modulated 633 nm laser (10 kW/cm^2). The resulting enhancement was calculated via two methods- direct comparison of the dual laser to the single laser emission intensity in the time trace and the amplitude of the Fourier transform of the time trace (inset Figure 5.9). A clear and steady decrease in the enhancement was observed with increasing modulation frequency (Figure 6.9, red). Corresponding well with the modeled data, the enhancement decreased to ~10% as it neared 4 kHz. As predicted by the model, the modulation frequency is

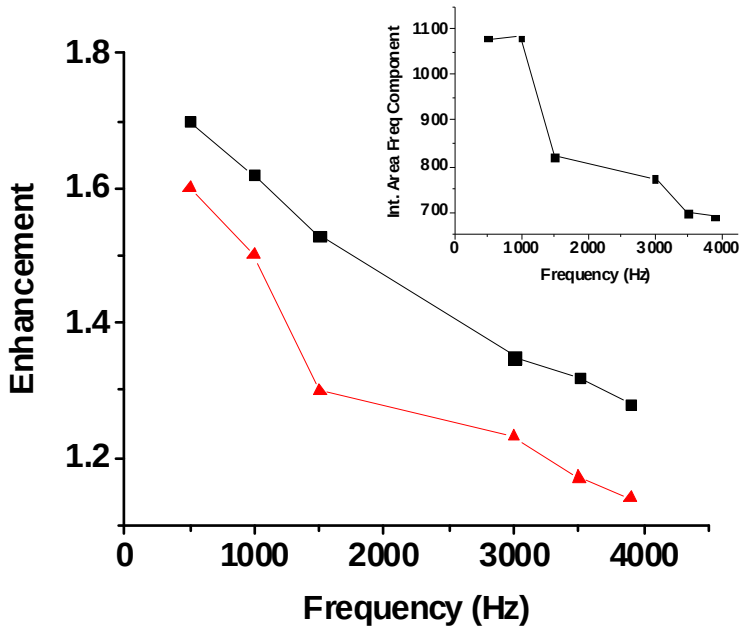

Figure 6.9. Cy3 fluorescence enhancement within the Cy3/Cy5 hairpin (1μM, aqueous), calculated from the 50-μs-binned time trace modulation depth, versus modulation frequency (red ▲, varied from 500 Hz to 3900 Hz). Cy3 emission was excited with primary 496 nm cw laser (500 W/cm^2) and secondary laser (10 kW/cm^2 633 nm cw). Modeled dependence of the enhancement on the modulation frequency (black ■) using an acceptor dark state quantum yield of 3×10^{-4} and dark state lifetime of 500 μs. Inset: Integrated area of the modulation frequency component in the Fourier transform of the time trace versus the modulation frequency.

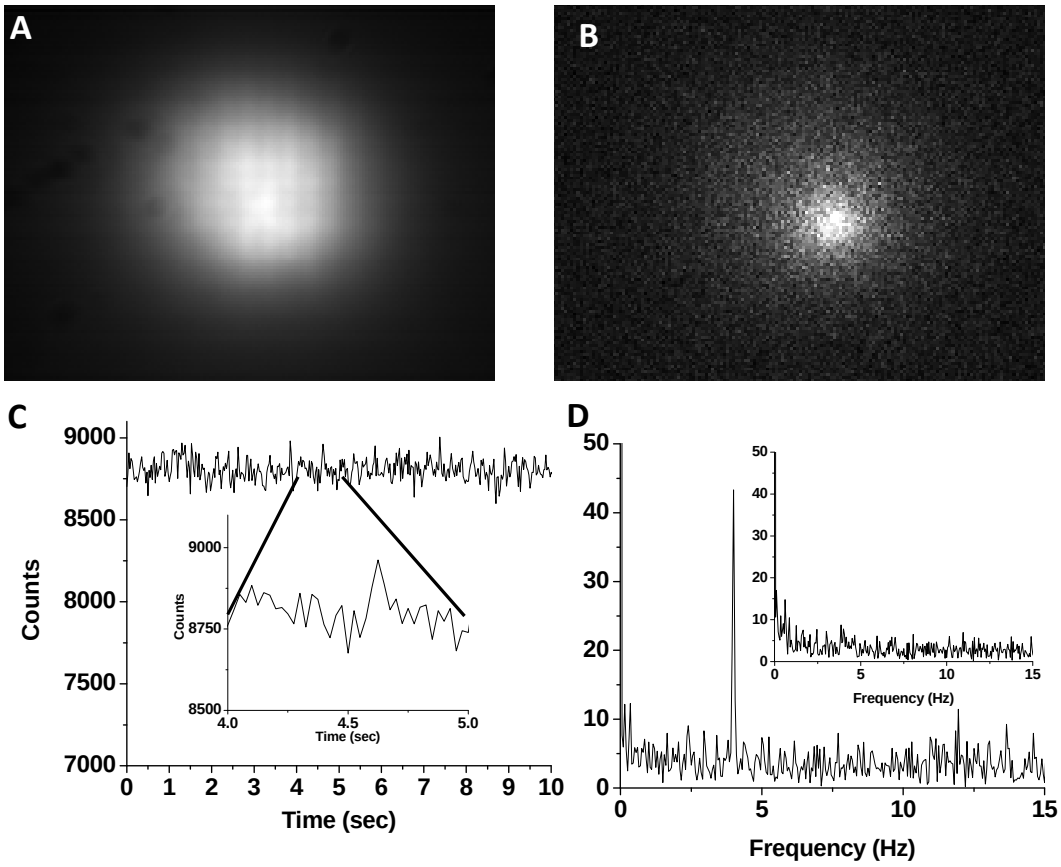

Figure 6.10. A. Average frame of Cy3-Cy5 hairpin structure in solution with 496 nm cw defocused excitation (700 W/cm^2) and more tightly focused 633 nm cw laser (10 kW/cm^2). Secondary excitation was chopped at 4 Hz; synchronous ccd detection was at 40 Hz. B. Whole image demodulation of the series of frames extracting only the modulated component at the pixels simultaneously exposed to both lasers. C. Representative time trace of a pixel within the dual illumination area. Inset showing 1 second interval of time trace. D. Fourier transform of the signal from C showing the modulation frequency encoded on the donor fluorescence, and the advantage of shifting the detection frequency away from the large low frequency peak Inset showing the Fourier transform of a single laser illuminated pixel.

approaching the time necessary to build up dark state populations that efficiently limit energy transfer. While such behavior limits available modulation frequencies, sufficient enhancement can be generated at moderate frequencies allowing us to demonstrate signal extraction.

In order to confirm that FRET based modulated signals can also be used for signal extraction, a 1 μM solution of the cy5-cy3 hairpin system was simultaneously exposed to a defocused 496 nm primary laser (700 W/cm^2) and a focused secondary 633 nm laser (10 kW/cm^2) modulated at 4 Hz. Data was collected at a frame rate of 40 Hz to insure at least 5 frames per each off and on cycle. An average frame exhibits a large fluorescence signal spread over several pixels (Figure 6.10 A). Utilizing the same pixel by pixel demodulation process as demonstrated previously for Ag nanoclusters and rose bengal, reveals a much smaller fluorescence spot corresponding to the area of the secondary laser (Figure 6.10 B). While the imposed modulation frequency is not readily apparent in the time trace from a pixel illuminated by both lasers (Figure 6.10 C), the resulting Fourier transform (Figure 6.10 D) nicely reveals the 4 Hz frequency component. To quantify the increase in signal to noise, the average image was compared directly to the demodulated image**.** Although unobservable with a signal to background estimated at ~0.005, the signal to noise within the average image is estimated in the ideal case to be ~0.44, based on the amplitude of the 4-Hz signal in the Fourier transform to the DC background noise (sqrt (8750)). Upon demodulation at 4 Hz, the signal (~41 cts) to background (~4 cts) improves to ~10 for the dual laser-illuminated pixels, while signal (41 counts) to noise (~1.8 counts), estimated from the standard deviation in frequency dependent intensities in the Fourier transform, improves to 23. Upon demodulation, signal to background and

signal to noise are therefore improved by ~2000-fold and ~50-fold, respectively. Therefore, the potential exists to engineer fluorescent systems from a wide array of existing fluorophores that can be utilized in FRET based signal extraction schemes.

6.9 Conclusion

The use of xanthenes dyes with large dark state quantum yields demonstrated that systems outside of Ag nanoclusters can be used for fluorescence modulation based signal extraction. While poorly suited for practical biological applications, these dyes helped illustrate that specific photophysical properties are required for optimized fluorescent systems. Targeting or engineering dyes with these characteristics could potentially lead to a specialized system of fluorescent labels, specifically designed for optical modulation. A limited survey of organic dyes, however, shows that these properties are exceedingly rare, and are so far best demonstrated by the as yet not fully developed Ag nanoclusters. Avoiding new fluorophore development, engineered FRET systems exhibit significant donor enhancement in the presence of direct acceptor excitation. The generalization of this new imaging concept afforded by its extension to FRET based systems offers significant advantages: a wider variety potential fluorophores, control over potential enhancement via FRET efficiency, and elimination of the need for specialized photophysical properties.

Still, there are some challenges. Even the lower intensities used for the cy3-cy5 system, would likely cause significant photobleaching for immobilized samples such as used in many biological imaging applications. Also the limitations imposed on the

modulation frequency would be incompatible with measuring dynamics on time scales faster than 10s of milliseconds. The FRET systems showing here are promising, but practical application will require improvements. Minor technical modifications, perhaps involving pulsed excitation sources, and more suitable FRET based fluorescence systems should allow for the extension of signal extraction to biological applications.

CONCLUSIONS AND FUTURE OUTLOOK

Fluorescence microscopy has grown to become one of the most widely used and versatile techniques for the characterization of cellular function and dynamics. Since its inception, the intricacy of biological imaging has grown as applications are designed for the visualization of increasingly smaller subcellular components. Imaging many of these macromolecules, which reside at low population levels in the cell, places an increased emphasis on distinguishing features through higher sensitivity. Experimental sensitivity is currently limited by inherent background fluorescence and relatively poor fluorophores. In spite of this, constant innovation in both fluorescent probes and techniques has led to our ever expanding knowledge of biological systems. Many studies, particularly at the single molecule level, would benefit greatly from the development of brighter and more photostable fluorophores.

Based on their exceptional brightness and photostability, Ag nanoclusters demonstrate the potential to increase sensitivity in biological imaging. Beyond this, we have shown that Ag nanoclusters exhibit very unique photophysical characteristics that allow for optical depopulation of a microsecond dark state. Exposing Ag nanoclusters to a secondary laser at lower energy than the emission leads to dynamic photobrightening of nanocluster emission. While this alone would result in higher sensitivity, the modulation and subsequent extraction of the fluorescent signal extends basic signal processing techniques to fluorescence imaging. From this, we have successfully demonstrated that relatively weak Ag nanocluster fluorescence can be extracted from high background signals.

Despite their great promise, Ag nanoclusters require substantial development before their application in biological imaging. Other fluorescent systems, however, can potentially be engineered to demonstrate similar characteristics. While existing fluorescent probes with the requisite properties are difficult to identify, less than ideal dyes enable the development of a general set of parameters that will be instrumental in selecting and engineering fluorophores specifically for optical modulation. Matching the necessary criteria, FRET systems readily demonstrate sensitivity improvements through signal extraction methods even in high backgrounds. Integrating other more commonly used fluorophores into modulation based schemes will simultaneously increase the utility and facilitate further optimization of this new technique.

One can easily imagine the expansion of optical modulation to applications in cellular imaging. For example, imaging of low copy number proteins, which are currently obscured by background, could potentially be realized with such sensitivity improvements. The studies shown here represent the first stage in the development of a novel concept for higher sensitivity imaging. The second stage will involve the precise development of optically modulated fluorescent systems tailored to specific applications. While requiring some technical refinement, the three systems discussed here, Ag nanoclusters, engineered dyes, and FRET systems, in some combination, are likely to play a key role in further development.

REFERENCES

(1) Kural, C.; Kim, H.; Syed, S.; Goshima, G.; Gelfand, V. I.; Selvin, P. R., *Kinesin and dynein move a peroxisome in vivo: A tug-of-war or coordinated movement? Science* **2005**, *308*, 1469-1472.

(2) Sako, Y.; Minoghchi, S.; Yanagida, T., *Single-molecule imaging of EGFR signalling on the surface of living cells. Nat. Cell. Bio.* **2000**, *2*, 168-172.

(3) Sevick-Muraca, E. M.; Houston, J. P.; Gurfinkel, M., *Fluorescence-enhanced, near infrared diagnostic imaging with contrast agents. Curr. Opin. Chem. Biol.* **2002**, *6*, 642-650.

(4) Taik Lim, Y.; Kim, S.; Nakayama, A.; Stott, N. E.; Bawendi, M. G.; Frangioni, J. V., *Selection of Quantum Dot Wavelengths for Biomedical Assays and Imaging. Molecular Imaging* **2003**, *2*, 50-64.

(5) Tokunaga, M.; Imamoto, N.; Sakata-Sogawa, K., *Highly inclined thin illumination enables clear single-molecule imaging in cells (vol 5, pg 159, 2008). Nat. Methods* **2008**, *5*, 455-455.

(6) Weissleder, R.; Pittet, M. J., *Imaging in the era of molecular oncology. Nature* **2008**, *452*, 580-589.

(7) Elf, J.; Li, G. W.; Xie, X. S., *Probing transcription factor dynamics at the single-molecule level in a living cell. Science* **2007**, *316*, 1191-1194.

(8) Hein, R.; Tsien, R. Y., *Engineering green fluorescent protein for improved brightness, longer wavelengths and fluorescence resonance energy transfer. Curr. Biol.* **1996**, *6*, 178-182.

(9) Rizzuto, R.; Brini, M.; DeGiorgi, F.; Rossi, R.; Heim, R.; Tsien, R. Y.; Pozzan, T., *Double labelling of subcellular structures with organelle-targeted GFP mutants in vivo. Curr. Biol.* **1996**, *6*, 183-188.

(10) Feng, Y.; Mitchison, T. J.; Bender, A.; Young, D. W.; Tallarico, J. A., *Multi-parameter phenotypic profiling: using cellular effects to characterize small-molecule compounds. Nat. Rev. Drug Discov.* **2009**, *8*, 567-578.

(11) Taylor, B. N.; Mehta, R. R.; Yamada, T.; Lekmine, F.; Christov, K.; Chakrabarty, A. M.; Green, A.; Bratescu, L.; Shilkaitis, A.; Beattie, C. W.; Gupta, T. K. D., *Noncationic Peptides Obtained From Azurin Preferentially Enter Cancer Cells. Cancer Res.* **2009**, *69*, 537-546.

(12) Zorrilla, S.; Lillo, M. P., *Quantitative Investigation of Biomolecular Interactions in Crowded Media by Fluorescence Spectroscopy, a Good Choice. Curr. Protein Pept. Sci.* **2009**, *10*, 376-387.

(13) Fischer, M.; Haase, I.; Wiesner, S.; Muller-Taubenberger, A., *Visualizing cytoskeleton dynamics in mammalian cells using a humanized variant of monomeric red fluorescent protein. FEBS Lett.* **2006**, *580*, 2495-2502.

(14) Bates, M.; Blosser, T. R.; Zhuang, X. W., *Short-range spectroscopic ruler based on a single-molecule optical switch. Phys. Rev. Lett.* **2005**, *94*, 108101.

(15) Bates, M.; Huang, B.; Dempsey, G. T.; Zhuang, X., *Multicolor Super-Resolution Imaging with Photo-Switchable Fluorescent Probes. Science* **2007**, *317*, 1749-1753.

(16) Betzig, E.; Patterson, G. H.; Sougrat, R.; Lindwasser, O. W.; Olenych, S.; Bonifacino, J. S.; Davidson, M. W.; Lippincott-Schwartz, J.; Hess, H. F., *Imaging Intracellular Fluorescent Proteins at Nanometer Resolution. Science* **2006**, *313*, 1642-1645.

(17) Helmuth, J. A.; Burckhardt, C. J.; Greber, U. F.; Sbalzarini, I. F., *Shape reconstruction of subcellular structures from live cell fluorescence microscopy images. J. Struct. Biol.* **2009**, *167*, 1-10.

(18) Bolte, S.; Cordelieres, F. P., *A guided tour into subcellular colocalization analysis in light microscopy. J. Microsc.-Oxf.* **2006**, *224*, 213-232.

(19) Gest, H., *The discovery of microorganisms by Robert Hooke and Antoni Van Leeuwenhoek, fellows of the Royal Society. Notes Rec. R. Soc. Lond.* **2004**, *58*, 187-201.

(20) Kruger, D. H.; Schneck, P.; Gelderblom, H. R., *Helmut Ruska and the visualisation of viruses. Lancet* **2000**, *355*, 1713-1717.

(21) Yasuda, K.; Coons, A. H., *LOCALIZATION BY IMMUNOFLUORESCENCE OF AMYLASE TRYPSINOGEN AND CHYMOTRYPSINOGEN IN ACINAR CELLS OF PIG PANCREAS. J. Histochem. Cytochem.* **1966**, *14*, 303-&.

(22) Weller, T. H.; Coons, A. H., *FLUORESCENT ANTIBODY STUDIES WITH AGENTS OF VARICELLA AND HERPES ZOSTER PROPAGATED INVITRO. Proc. Soc. Exp. Biol. Med.* **1954**, *86*, 789-794.

(23) Coons, A. H.; Kaplan, M. H., *LOCALIZATION OF ANTIGEN IN TISSUE CELLS .2. IMPROVEMENTS IN A METHOD FOR THE DETECTION OF ANTIGEN BY MEANS OF FLUORESCENT ANTIBODY. J. Exp. Med.* **1950**, *91*, 1-13.

(24) Monici, M. *Cell and tissue autofluorescence research and diagnostic applications*; Elsevier Science Bv, 2005.

(25) Jorgensen, L.; Wood, G. K.; Rosenkrands, I.; Petersen, C.; Christensen, D., *Protein adsorption and displacement at lipid layers determined by total internal reflection fluorescence (TIRF). J. Liposome Res.* **2009**, *19*, 99-104.

(26) Mettlen, M.; Stoeber, M.; Loerke, D.; Antonescu, C. N.; Danuser, G.; Schmid, S. L., *Endocytic Accessory Proteins Are Functionally Distinguished by Their Differential Effects on the Maturation of Clathrin-coated Pits. Mol. Biol. Cell* **2009**, *20*, 3251-3260.

(27) Zipfel, W. R.; Williams, R. M.; Webb, W. W., *Nonlinear magic: multiphoton microscopy in the biosciences. Nat. Biotechnol.* **2003**, *21*, 1368-1376.

(28) Xu, C.; Zipfel, W.; Shear, J. B.; Williams, R. M.; Webb, W. W., *Multiphoton fluorescence excitation: New spectral windows for biological nonlinear microscopy. Proc. Natl. Acad. Sci. U. S. A.* **1996**, *93*, 10763-10768.

(29) Cavanagh, H. D.; El-Agha, M. S.; Petroll, W. M.; Jester, J. V., *Specular microscopy, confocal microscopy, and ultrasound biomicroscopy - Diagnostic tools of the past quarter century. Cornea* **2000**, *19*, 712-722.

(30) Nie, S. M.; Zare, R. N., *Optical detection of single molecules. Annu. Rev. Biophys. Biomol. Struct.* **1997**, *26*, 567-596.

(31) Falk, M. M.; Lauf, U., *High resolution, fluorescence deconvolution microscopy and tagging with the autofluorescent tracers CFP, GFP, and YFP to study the structural composition of gap junctions in living cells. Microsc Res Tech* **2001**, *52*, 251-62.

(32) Antony, T.; Subramaniam, V., *Molecular beacons: Nucleic acid hybridization and emerging applications. J. Biomol. Struct. Dyn.* **2001**, *19*, 497-504.

(33) Vermot, J.; Fraser, S. E.; Liebling, M., *Fast fluorescence microscopy for imaging the dynamics of embryonic development. Hfsp J.* **2008**, *2*, 143-155.

(34) Van Manen, H. J.; Van Bruggen, R.; Roos, D.; Otto, C., *Single-cell optical imaging of the phagocyte NADPH oxidase. Antioxid. Redox Signaling* **2006**, *8*, 1509-1522.

(35) Walther, A.; Wendland, J., *Apical localization of actin patches and vacuolar dynamics in Ashbya gossypii depend on the WASP homolog Wal1p. J. Cell Sci.* **2004**, *117*, 4947-4958.

(36) Oghalai, J. S.; Patel, A. A.; Nakagawa, T.; Brownell, W. E., *Fluorescence-imaged microdeformation of the outer hair cell lateral wall. J. Neurosci.* **1998**, *18*, 48-58.

(37) Cardinale, S.; Cisterna, B.; Bonetti, P.; Aringhieri, C.; Biggiogera, M.; Barabino, S. M. L., *Subnuclear localization and dynamics of the pre-mRNA 3 ' end processing factor mammalian cleavage factor I 68-kDa subunit. Mol. Biol. Cell* **2007**, *18*, 1282-1292.

(38) Poulsen, A. K.; Petersen, M. O.; Olsen, L. F., *Single cell studies and simulation of cell-cell interactions using oscillating glycolysis in yeast cells. Biophys. Chem.* **2007**, *125*, 275-280.

(39) Santra, S.; Yang, H.; Stanley, J. T.; Holloway, P. H.; Moudgil, B. M.; Walter, G.; Mericle, R. A., *Rapid and effective labeling of brain tissue using TAT-conjugated CdS: Mn/ZnS quantum dots. Chem. Commun.* **2005**, 3144-3146.

(40) Chen, I.; Choi, Y. A.; Ting, A. Y., *Phage display evolution of a peptide substrate for yeast biotin ligase and application to two-color quantum dot labeling of cell surface proteins. J. Amer. Chem. Soc.* **2007**, *129*, 6619-6625.

(41) Liang, M. M.; Liu, X. R.; Cheng, D. F.; Nakamura, K.; Wang, Y.; Dou, S. P.; Liu, G. Z.; Rusckowsci, M.; Hnatowich, D. J., *Optical Antisense Tumor Targeting in Vivo with an Improved Fluorescent DNA Duplex Probe. Bioconjugate Chem.* **2009**, *20*, 1223-1227.

(42) Shoji, Y.; Akhtar, S.; Periasamy, A.; Herman, B.; Juliano, R. L., *MECHANISM OF CELLULAR UPTAKE OF MODIFIED OLIGODEOXYNUCLEOTIDES CONTAINING METHYLPHOSPHONATE LINKAGES. Nucleic Acids Res.* **1991**, *19*, 5543-5550.

(43) Wang, D. O.; Kim, S. M.; Zhao, Y. L.; Hwang, H.; Miura, S. K.; Sossin, W. S.; Martin, K. C., *Synapse- and Stimulus-Specific Local Translation During Long-Term Neuronal Plasticity. Science* **2009**, *324*, 1536-1540.

(44) Handa, N.; Amitani, I.; Gumlaw, N.; Sandler, S. J.; Kowalczykowski, S. C., *Single Molecule Analysis of a Red Fluorescent RecA Protein Reveals a Defect in Nucleoprotein Filament Nucleation That Relates to Its Reduced Biological Functions. J. Biol. Chem.* **2009**, *284*, 18664-18673.

(45) Kubin, R. F.; Fletcher, A. N., *FLUORESCENCE QUANTUM YIELDS OF SOME RHODAMINE DYES. J. Lumin.* **1982**, *27*, 455-462.

(46) Lakowicz, J. R. *Principles of Fluorescence Spectroscopy*; 2nd ed.; Kluwer Academic/Plenum Publishers: New York, 1999.

(47) Mujumdar, R. B.; Ernst, L. A.; Mujumdar, S. R.; Lewis, C. J.; Waggoner, A. S., *Cyanine Dye Labeling Reagents - Sulfoindocyanine Succinimidyl Esters. Bioconjugate Chem.* **1993**, *4*, 105-111.

(48) Rasnik, I.; McKinney, S. A.; Ha, T., *Nonblinking and longlasting single-molecule fluorescence imaging. Nat. Methods* **2006**, *3*, 891-893.

(49) Fu, Y.; Lakowicz, J. R., *Modification of single molecule fluorescence near metallic nanostructures. Laser Photon. Rev.* **2009**, *3*, 221-232.

(50) Holder, A. N.; Ellis, A. L.; Zou, J.; Chen, N.; Yang, J. J., *Facilitating chromophore formation of engineered Ca2+ binding green fluorescent proteins. Arch. Biochem. Biophys.* **2009**, *486*, 27-34.

(51) Renesto, P.; Gouin, E.; Raoult, D., *Expression of green fluorescent protein in Rickettsia conorii. Microb. Pathog.* **2002**, *33*, 17-21.

(52) Asimakopoulos, F.; Varmus, H. E., *Cell-Specific Transduction of Prdm1-Expressing Lineages Mediated by a Receptor for Avian Leukosis Virus Subgroup B. J. Virol.* **2009**, *83*, 4835-4843.

(53) Douglass, A. D.; Vale, R. D. In *Fluorescent Proteins, Second Edition*; Elsevier Academic Press Inc: San Diego, 2008; Vol. 85, p 113-125.

(54) Sun, J. J.; Goldys, E. M., *Linear absorption and molar extinction coefficients in direct semiconductor quantum dots. J. Phys. Chem. C* **2008**, *112*, 9261-9266.

(55) Dubertret, B.; Skourides, P.; Norris, D. J.; Noireaux, V.; Brivanlou, A. H.; Libchaber, A., *In vivo imaging of quantum dots encapsulated in phospholipid micelles. Science* **2002**, *298*, 1759-1762.

(56) Michalet, X.; Pinaud, F. F.; Bentolila, L. A.; Tsay, J. M.; Doose, S.; Li, J. J.; Sundaresan, G.; Wu, A. M.; Gambhir, S. S.; Weiss, S., *Quantum dots for live cells, in vivo imaging, and diagnostics. Science* **2005**, *307*, 538-544.

(57) Gaeta, S. A.; Bub, G.; Abbott, G. W.; Christini, D. J., *Dynamical Mechanism for Subcellular Alternans in Cardiac Myocytes. Circ.Res.* **2009**, *105*, 335-U55.

(58) Lowery, R. L.; Zhang, Y.; Kelly, E. A.; Lamantia, C. E.; Harvey, B. K.; Majewska, A. K., *Rapid, Long-Term Labeling of Cells in the Developing and Adult Rodent Visual Cortex Using Double-Stranded Adeno-Associated Viral Vectors. Dev. Neurobiol.* **2009**, *69*, 674-688.

(59) Ni, Q.; Titov, D. V.; Zhang, J., *Analyzing protein kinase dynamics in living cells with FRET reporters. Methods* **2006**, *40*, 279-286.

(60) Verbrugge, S.; Lechner, B.; Woehlke, G.; Peterman, E. J. G., *Alternating-Site Mechanism of Kinesin-1 Characterized by Single-Molecule FRET Using Fluorescent ATP Analogues. Biophys. J.* **2009**, *97*, 173-182.

(61) Rock, R. S.; Rice, S. E.; Wells, A. L.; Purcell, T. J.; Spudich, J. A.; Sweeney, H. L., *Myosin VI is a processive motor with a large step size. Proc. Natl. Acad. Sci. U. S. A.* **2001**, *98*, 13655-13659.

(62) Onoa, B.; Tinoco, I., *RNA folding and unfolding. Curr. Opin. Struct. Biol.* **2004**, *14*, 374-379.

(63) Pljevaljcic, G.; Millar, D. P.; Deniz, A. A., *Freely diffusing single hairpin ribozymes provide insights into the role of secondary structure and partially folded states in RNA folding. Biophys. J.* **2004**, *87*, 457-467.

(64) Marshall, R. A.; Aitken, C. E.; Dorywalska, M.; Puglisi, J. D., *Translation at the single-molecule level. Annu. Rev. Biochem.* **2008**, *77*, 177-203.

(65) Blanchard, S. C.; Kim, H. D.; Gonzalez, R. L.; Puglisi, J. D.; Chu, S., *tRNA dynamics on the ribosome during translation. Proc. Natl. Acad. Sci. U. S. A.* **2004**, *101*, 12893-12898.

(66) Zondervan, R.; Kulzer, F.; Orlinskii, S. B.; Orrit, M., *Photoblinking of Rhodamine 6G in Poly(vinyl alcohol): Radical Dark State Formed through the Triplet. The Journal of Physical Chemistry A* **2003**, *107*, 6770-6776.

(67) Yip, W. T.; Hu, D. H.; Yu, J.; Vanden Bout, D. A.; Barbara, P. F., *Classifying the photophysical dynamics of single- and multiple- chromophoric molecules by single molecule spectroscopy. J. Phys. Chem. A* **1998**, *102*, 7564-7575.

(68) Yip, W. T.; Hu, D. H.; Yu, J.; Vanden Bout, D. A.; Barbara, P. F., *Classifying the photophysical dynamics of single- and multiple-chromophoric molecules by single molecule spectroscopy. J. Phys. Chem. A* **1998**, *102*, 7564-7575.

(69) Eggeling, C.; Widengren, J.; Brand, L.; Schaffer, J.; Felekyan, S.; Seidel, C. A. M., *Analysis of photobleaching in single-molecule multicolor excitation and forster resonance energy transfer measurement. J. Phys. Chem. A* **2006**, *110*, 2979-2995.

(70) Larkin, J. M.; Donaldson, W. R.; Knox, R. S.; Foster, T. H., *Reverse intersystem crossing in rose bengal. II. Fluence dependence of fluorescence following 532 nm laser excitation. Photochem. and Photobiol.* **2002**, *75*, 221-228.

(71) Seefeldt, B.; Kasper, R.; Seidel, T.; Tinnefeld, P.; Dietz, K. J.; Heilemann, M.; Sauer, M., *Fluorescent proteins for single-molecule fluorescence applications. J. Biophotonics* **2008**, *1*, 74-82.

(72) Dickson, R. M.; Cubitt, A. B.; Tsien, R. Y.; Moerner, W. E., *On/off blinking and switching behaviour of single molecules of green fluorescent protein. Nature* **1997**, *388*, 355-358.

(73) Biebricher, A.; Sauer, M.; Tinnefeld, P., *Radiative and nonradiative rate fluctuations of single colloidal semiconductor nanocrystals. J. Phys. Chem. B* **2006**, *110*, 5174-5178.

(74) Yao, J.; Larson, D. R.; Vishwasrao, H. D.; Zipfel, W. R.; Webb, W. W., *Blinking and nonradiant dark fraction of water-soluble quantum dots in aqueous solution. Proc. Natl. Acad. Sci. U. S. A.* **2005**, *102*, 14284-14289.

(75) Nirmal, M.; Dabbousi, B. O.; Bawendi, M. G.; Macklin, J. J.; Trautman, J. K.; Harris, T. D.; Brus, L. E., *Fluorescence intermittency in single cadmium selenide nanocrystals. Nature* **1996**, *383*, 802-804.

(76) Sabanayagam, C. R.; Eid, J. S.; Meller, A., *Long time scale blinking kinetics of cyanine fluorophores conjugated to DNA and its effect on Forster resonance energy transfer. J. Chem. Phys.* **2005**, *123*.

(77) Yeh, H. C.; Puleo, C. M.; Ho, Y. P.; Bailey, V. J.; Lim, T. C.; Liu, K.; Wang, T. H., *Tunable blinking kinetics of Cy5 for precise DNA quantification and single-nucleotide difference detection. Biophys. J.* **2008**, *95*, 729-737.

(78) Daniel, D. C.; Thompson, M.; Woodbury, N. W., *Fluorescence intensity fluctuations of individual labeled DNA fragments and a DNA binding protein in solution at the single molecule level: A comparison of photobleaching, diffusion, and binding dynamics. J. Phys. Chem. B* **2000**, *104*, 1382-1390.

(79) Eggeling, C.; Widengren, J.; Rigler, R.; Seidel, C. A. M., *Photobleaching of fluorescent dyes under conditions used for single-molecule detection: Evidence of two-step photolysis. Anal. Chem.* **1998**, *70*, 2651-2659.

(80) Haupts, U.; Maiti, S.; Schwille, P.; Webb, W. W., *Dynamics of fluorescence fluctuations in green fluorescent protein observed by fluorescence correlation spectroscopy. Proc. Natl. Acad. Sci. U. S. A.* **1998**, *95*, 13573-13578.

(81) Malvezzi-Campeggi, F.; Jahnz, M.; Heinze, K. G.; Dittrich, P.; Schwille, P., *Light-induced flickering of DsRed provides evidence for distinct and interconvertible fluorescent states. Biophys. J.* **2001**, *81*, 1776-1785.

(82) Schwille, P.; Kummer, S.; Heikal, A. A.; Moerner, W. E.; Webb, W. W., *Fluorescence correlation spectroscopy reveals fast optical excitation-driven intramolecular dynamics of yellow fluorescent proteins. Proc. Natl. Acad. Sci. U. S. A.* **2000**, *97*, 151-156.

(83) Vosch, T.; Antoku, Y.; Hsiang, J. C.; Richards, C. I.; Gonzalez, J. I.; Dickson, R. M., *Strongly emissive individual DNA-encapsulated Ag nanoclusters as single-molecule fluorophores. Proc. Natl. Acad. Sci. U. S. A.* **2007**, *104*, 12616-12621.

(84) Huang, Z. X.; Ji, D. M.; Wang, S. F.; Xia, A. D.; Koberling, F.; Patting, M.; Erdmann, R., *Spectral identification of specific photophysics of Cy5 by means of ensemble and single molecule measurements. J. Phys. Chem. A* **2006**, *110*, 45-50.

(85) Widengren, J.; Schwille, P., *Characterization of photoinduced isomerization and back-isomerization of the cyanine dye Cy5 by fluorescence correlation spectroscopy. J. Phys. Chem. A* **2000**, *104*, 6416-6428.

(86) Blom, H.; Chmyrov, A.; Hassler, K.; Davis, L. M.; Widengren, J., *Triplet-State Investigations of Fluorescent Dyes at Dielectric Interfaces Using Total Internal Reflection Fluorescence Correlation Spectroscopy. J. Phys. Chem. A* **2009**, *113*, 5554-5566.

(87) Vogelsang, J.; Cordes, T.; Tinnefeld, P., *Single-molecule photophysics of oxazines on DNA and its application in a FRET switch. Photochem. Photobiol. Sci.* **2009**, *8*, 486-496.

(88) Kolwas, K.; Derkachova, A.; Shopa, M.; Pergamon-Elsevier Science Ltd: 2009, p 1490-1501.

(89) Tiago, M. L.; Idrobo, J. C.; Ogut, S.; Jellinek, J.; Chelikowsky, J. R., *Electronic and optical excitations in Ag-n clusters (n=1-8): Comparison of density-functional and many-body theories. Phys. Rev. B* **2009**, *79*, 14.

(90) Drude, P., *On the electron theory of metals. Ann. Phys.-Berlin* **1900**, *1*, 566-613.

(91) Kreibig, U.; Vollmer, M. *Optical Properties of Metal Clusters*; Springer: Berlin, 1995; Vol. 25.

(92) Dupree, R.; Smithard, M. A., *Electronic Properties of Small Metal Particles - Electric Polarizability. Journal of Physics Part C Solid State Physics* **1972**, *5*, 408-&.

(93) Johnston, R. L. *Atomic and Molecular Clusters*; Taylor & Francis: London and New York, 2002.

(94) Diederich, T.; Tiggesbaumker, J.; Meiwes-Broer, K. H., *Spectroscopy on rare gas-doped silver clusters in helium droplets. J. Chem. Phys.* **2002**, *116*, 3263-3269.

(95) Ievlev, D.; Rabin, L.; Schulze, W.; Ertl, G., *Fluorescence spectroscopy of silver clusters formed in rare gas droplets. European Physical Journal D* **2001**, *16*, 157-160.

(96) Schulze, W.; Rabin, I.; Ertl, G., *Formation of light-emitting Ag-2 and Ag-3 species in the course of condensation of Ag atoms with Ar. ChemPhysChem* **2004**, *5*, 403-407.

(97) Fedrigo, S.; Harbich, W.; Buttet, J., *Optical response of Ag2, Ag3, Au2, and Au3 in argon matrices. J. Chem. Phys.* **1993**, *99*, 5712-5717.

(98) Radcliffe, P.; Przystawik, A.; Diederich, T.; Doppner, T.; Tiggesbaumker, J.; Meiwes-Broer, K. H., *Excited-state relaxation of Ag-8 clusters embedded in helium droplets. Phys. Rev. Lett.* **2004**, *92*.

(99) Yoon, J.; Kim, K. S.; Baeck, K. K., *Ab initio study of the low-lying electronic states of Ag_3^-, Ag_3, and Ag_3^+: a coupled-cluster approach. J. Chem. Phys.* **2000**, *112*, 9335-9342.

(100) Henglein, A., *Small-Particle Research - Physicochemical Properties of Extremely Small Colloidal Metal and Semiconductor Particles. Chem. Rev.* **1989**, *89*, 1861-1873.

(101) Linnert, T.; Mulvaney, P.; Henglein, A.; Weller, H., *Long-Lived Nonmetallic Silver Clusters in Aqueous-Solution - Preparation and Photolysis. J. Amer. Chem. Soc.* **1990**, *112*, 4657-4664.

(102) Henglein, A.; Mulvaney, P.; Linnert, T., *Chemistry of Agn Aggregates in Aqueous-Solution - Nonmetallic Oligomeric Clusters and Metallic Particles. Faraday Discuss.* **1991**, 31-44.

(103) Janata, E.; Henglein, A.; Ershov, B. G., *First Clusters of Ag+ Ion Reduction in Aqueous-Solution. J. Phys. Chem.* **1994**, *98*, 10888-10890.

(104) Zheng, J.; Petty, J. T.; Dickson, R. M., *High Quantum Yield Blue Emission from Water-Soluble Au_8 Nanodots. J. Amer. Chem. Soc.* **2003**, *125*, 7780-7781.

(105) Peyser, L. A.; Vinson, A. E.; Bartko, A. P.; Dickson, R. M., *Photoactivated fluorescence from individual silver nanoclusters. Science* **2001**, *291*, 103-106.

(106) Shang, L.; Dong, S. J., *Silver nanocluster-based fluorescent sensors for sensitive detection of Cu(II). J. Mater. Chem.* **2008**, *18*, 4636-4640.

(107) Richards, C. I.; Choi, S.; Hsiang, J. C.; Antoku, Y.; Vosch, T.; Bongiorno, A.; Tzeng, Y. L.; Dickson, R. M., *Oligonucleotide-stabilized Ag nanocluster fluorophores. J Amer. Chem. Soc.* **2008**, *130*, 5038-5039.

(108) Petty, J. T.; Zheng, J.; Hud, N. V.; Dickson, R. M., *DNA-Templated Ag Nanocluster Formation. J. Amer. Chem. Soc.* **2004**, *126*, 5207-5212.

(109) Junhua Yu, S. C., Robert M. Dickson, *Shuttle-Based Fluorogenic Silver-Cluster Biolabels. Angewandte Chemie International Edition* **2009**, *48*, 318-320.

(110) O'Neill, P. R.; Velazquez, L. R.; Dunn, D. G.; Gwinn, E. G.; Fygenson, D. K., *Hairpins with Poly-C Loops Stabilize Four Types of Fluorescent Ag-n:DNA. J. Phys. Chem. C* **2009**, *113*, 4229-4233.

(111) Weizmann, Y.; Braunschweig, A. B.; Wilner, O. I.; Cheglakov, Z.; Willner, I., *A polycatenated DNA scaffold for the one-step assembly of hierarchical nanostructures. Proc. Natl. Acad. Sci. U. S. A.* **2008**, *105*, 5289-5294.

(112) Nishinaka, T.; Takano, A.; Doi, Y.; Hashimoto, M.; Nakamura, A.; Matsushita, Y.; Kumaki, J.; Yashima, E., *Conductive metal nanowires templated by the nucleoprotein filaments, complex of DNA and RecA protein. J. Am. Chem. Soc.* **2005**, *127*, 8120-8125.

(113) Eichhorn, G. L.; Shin, Y. A., *Interaction of metal ions with polynucleotides and related compounds. XII. The relative effect of various metal ions on DNA helicity. J. Amer. Chem. Soc.* **2002**, *90*, 7323-7328.

(114) Storhoff, J. J.; Mirkin, C. A., *Programmed materials synthesis with DNA. Chem. Rev.* **1999**, *99*, 1849-1862.

(115) Mucic, R. C.; Storhoff, J. J.; Mirkin, C. A.; Letsinger, R. L., *DNA-directed synthesis of binary nanoparticle network materials. J. Amer. Chem. Soc.* **1998**, *120*, 12674-12675.

(116) Elghanian, R.; Storhoff, J. J.; Mucic, R. C.; Letsinger, R. L.; Mirkin, C. A., *Selective colorimetric detection of polynucleotides based on the distance-dependent optical properties of gold nanoparticles. Science* **1997**, *277*, 1078-1081.

(117) Mirkin, C. A.; Letsinger, R. L.; Mucic, R. C.; Storhoff, J. J., *A DNA-based method for rationally assembling nanoparticles into macroscopic materials. Nature* **1996**, *382*, 607-609.

(118) Becerril, H. A.; Woolley, A. T., *DNA-templated nanofabrication. Chem. Soc. Rev.* **2009**, *38*, 329-337.

(119) Park, S. H.; Prior, M. W.; LaBean, T. H.; Finkelstein, G., *Optimized fabrication and electrical analysis of silver nanowires templated on DNA molecules. Appl. Phys. Lett.* **2006**, *89*, 3.

(120) Ongaro, A.; Griffin, F.; Beeeher, P.; Nagle, L.; Iacopino, D.; Quinn, A.; Redmond, G.; Fitzmaurice, D., *DNA-templated assembly of conducting gold nanowires between gold electrodes on a silicon oxide substrate. Chem. Mat.* **2005**, *17*, 1959-1964.

(121) Zinchenko, A. A.; Yoshikawa, K.; Baigl, D., *DNA-templated silver nanorings. Adv. Mater.* **2005**, *17*, 2820-+.

(122) Duguid, J.; Bloomfield, V. A.; Benevides, J.; Thomas, G. J., *RAMAN SPECTRAL STUDIES OF NUCLEIC-ACIDS .44. RAMAN-SPECTROSCOPY OF DNA-METAL COMPLEXES .1. INTERACTIONS AND CONFORMATIONAL EFFECTS OF THE DIVALENT-CATIONS - MG, CA, SR, BA, MN, CO, NI, CU, PD, AND CD. Biophys. J.* **1993**, *65*, 1916-1928.

(123) Eichhorn, G. L.; Butzow, J. J.; Clark, P.; Tarien, E., *INTERACTION OF METAL IONS WITH POLYNUCLEOTIDES AND RELATED COMPOUNDS .X. STUDIES ON REACTION OF SILVER(I) WITH NUCLEOSIDES AND POLYNUCLEOTIDES AND*

EFFECT OF SILVER(1) ON ZINC(2) DEGRADATION OF POLYNUCLEOTIDES. Biopolymers **1967**, *5*, 283-&.

(124) Yamane, T.; Davidson, N., *ON COMPLEXING OF DEOXYRIBONUCLEIC ACID BY SILVER(I). Biochimica Et Biophysica Acta* **1962**, *55*, 609-&.

(125) Sengupta, B.; Ritchie, C. M.; Buckman, J. G.; Johnsen, K. R.; Goodwin, P. M.; Petty, J. T., *Base-Directed Formation of Fluorescent Silver Clusters. J. Phys. Chem. C* **2008**, *112*, 18776-18782.

(126) Patel, S. Ph.D. Thesis, Georgia Institute of Technology, 2009.

(127) Brown, M. A. *MRI : basic principles and applications*; Wiley-Liss: New York :, 1995.

(128) Mandon, J.; Guelachvili, G.; Picque, N.; Druon, F.; Georges, P., *Femtosecond laser Fourier transform absorption spectroscopy. Opt. Lett.* **2007**, *32*, 1677-1679.

(129) Smith, S. W. *The Scientist & Engineer's Guide to Digital Signal Processing*; California Technical Publishing: San Diego, Ca, 1997.

(130) Zhang, L. R.; Xu, Q. X.; Xing, D.; Gao, C. J.; Xiong, H. W., *Real-Time Detection of Caspase-3-Like Protease Activation in Vivo Using Fluorescence Resonance Energy Transfer during Plant Programmed Cell Death Induced by Ultraviolet C Overexposure. Plant Physiol.* **2009**, *150*, 1773-1783.

(131) Nienhaus, G. U., *Exploring protein structure and dynamics under denaturing conditions by single-molecule FRET analysis. Macromol. Biosci.* **2006**, *6*, 907-922.

(132) Mori, T.; Vale, R. D.; Tomishige, M., *How kinesin waits between steps. Nature* **2007**, *450*, 750-U15.

(133) Chung, H. S.; Louis, J. M.; Eaton, W. A., *Experimental determination of upper bound for transition path times in protein folding from single-molecule photon-by-photon trajectories. Proc. Natl. Acad. Sci. U. S. A.* **2009**, *106*, 11837-11844.

(134) Jares-Erijman, E. A.; Jovin, T. M., *FRET imaging. Nat. Biotechnol.* **2003**, *21*, 1387-1395.

(135) Beutler, M.; Makrogianneli, K.; Vermeij, R. J.; Keppler, M.; Ng, T.; Jovin, T. M.; Heintzmann, R., *satFRET: estimation of Forster resonance energy transfer by acceptor saturation. European Biophysics Journal with Biophysics Letters* **2008**, *38*, 69-82.

(136) Schonle, A.; Hanninen, P. E.; Hell, S. W., *Nonlinear fluorescence through intermolecular energy transfer and resolution increase in fluorescence microscopy. Ann. Phys.-Berlin* **1999**, *8*, 115-133.

(137) Hanninen, P. E.; Lehtela, L.; Hell, S. W., *Two- and multiphoton excitation of conjugate-dyes using a continuous wave laser. Optics Communications* **1996**, *130*, 29-33.

(138) Becker, W. *Advanced Time-Correlated Single Photon Counting Techniques*; Springer: Berlin, 2005.

(139) Schwille, P.; Haustein, H. *Fluorescence Correlation Spectroscopy: An Introduction to its Concepts and Applications.*

(140) Schwille, P.; Korlach, J.; Webb, W. W., *Fluorescence correlation spectroscopy with single-molecule sensitivity on cell and model membranes. Cytometry* **1999**, *36*, 176-182.

(141) Bartko, A. P.; Dickson, R. M., *Three-dimensional orientations of polymer-bound single molecules. J. Phys. Chem. B* **1999**, *103*, 3053-3056.

(142) Bartko, A. P.; Dickson, R. M., *Imaging three-dimensional single molecule orientations. J. Phys. Chem. B* **1999**, *103*, 11237-11241.

(143) Bartko, A. P.; Peyser, L. A.; Dickson, R. M.; Mehta, A.; Thundat, T.; Bhargava, R.; Barnes, M. D., *Observation of dipolar emission patterns from isolated Eu3+: Y2O3 doped nanocrystals: new evidence for single ion luminescence. Chem. Phys. Lett.* **2002**, *358*, 459-465.

(144) Seki, K.; Tachiya, M., *Theory of antibunching of photon emission I. J. Chem. Phys.* **2009**, *130*, 10.

(145) Fedrigo, S.; Harbich, W.; Belyaev, J.; Buttet, J., *Evidence for electronic shell structure of small silver clusters in the optical-absorption spectra. Chem. Phys. Lett.* **1993**, *211*, 166-170.

(146) De Cremer, G.; Coutino-Gonzalez, E.; Roeffaers, M. B. J.; Moens, B.; Ollevier, J.; Van der Auweraer, M.; Schoonheydt, R.; Jacobs, P. A.; De Schryver, F. C.; Hofkens, J.; De Vos, D. E.; Sels, B. F.; Vosch, T., *Characterization of Fluorescence in Heat-Treated Silver-Exchanged Zeolites. J. Amer. Chem. Soc.* **2009**, *131*, 3049-3056.

(147) Karthikeyan, B., *Fluorescent glass embedded silver nanoclusters: An optical study. J. Appl. Phys.* **2008**, *103*, 5.

(148) Bonacic-Kouteck, V.; Burgel, C.; Kronik, L.; Kuznetsov, A. E.; Mitric, R., *Optical properties of small silver clusters supported at MgO. European Physical Journal D* **2007**, *45*, 471-476.

(149) Tom Vosch, Y. A., Jung-Cheng Hsiang, Chris I. Richards, Jose I. Gonzalez, and Robert M. Dickson, *Strongly emissive individual DNA-encapsulated Ag nanoclusters as single-molecule fluorophores. Proceedings of the National Academy of Sciences* **2007**.

(150) Al-Said, S. A. F.; Hassanien, R.; Hannant, J.; Galindo, M. A.; Pruneanu, S.; Pike, A. R.; Houlton, A.; Horrocks, B. R., *Templating Ag on DNA/polymer hybrid nanowires: Control of the metal growth morphology using functional monomers. Electrochem. Commun.* **2009**, *11*, 550-553.

(151) Cui, S. Q.; Liu, Y. C.; Yang, Z. S.; Wei, X. W., *Construction of silver nanowires on DNA template by an electrochemical technique. Mater. Des.* **2007**, *28*, 722-725.

(152) Gwinn, E. G.; O'Neill, P.; Guerrero, A. J.; Bouwmeester, D.; Fygenson, D. K., *Sequence-dependent fluorescence of DNA-hosted silver nanoclusters. Adv. Mater.* **2008**, *20*, 279-+.

(153) Verma, A.; Yadav, V. K.; Basundra, R.; Kumar, A.; Chowdhury, S., *Evidence of genome-wide G4 DNA-mediated gene expression in human cancer cells. Nucleic Acids Res.* **2009**, *37*, 4194-4204.

(154) Dias, N.; Stein, C. A., *Antisense oligonucleotides: Basic concepts and mechanisms. Mol. Cancer Ther.* **2002**, *1*, 347-355.

(155) Kricka, L. J., *Stains, labels and detection strategies for nucleic acids assays. Annals of Clinical Biochemistry* **2002**, *39*, 114-129.

(156) Zinchenko, A. A.; Baigl, D. M.; Chen, N.; Pyshkina, O.; Endo, K.; Sergeyev, V. G.; Yoshikawa, K., *Conformational behavior of giant DNA through binding with Ag+ and metallization. Biomacromolecules* **2008**, *9*, 1981-1987.

(157) Zeiss, C. *Advanced Imaging Microscopy- Confocor 2 Applications Handbook*; Zeiss: Jena, Germany, 2001.

(158) Smith, A. M.; Nie, S., *Minimizing the Hydrodynamic Size of Quantum Dots with Multifunctional Multidentate Polymer Ligands. J. Amer. Chem. Soc.* **2008**, *130*, 11278-11279.

(159) Wang, J. Y.; Wang, X. Q.; Ren, L.; Wang, Q.; Li, L.; Liu, W. M.; Wan, Z. F.; Yang, L. Y.; Sun, P.; Ren, L. L.; Li, M. L.; Wu, H.; Wang, J. F.; Zhangt, L., *Conjugation of Biomolecules with Magnetic Protein Microspheres for the Assay of Early Biomarkers Associated with Acute Myocardial Infarction. Anal. Chem.* **2009**, *81*, 6210-6217.

(160) Phillips, W. T.; Medina, L. A.; Klipper, R.; Goins, B., *A novel approach for the increased delivery of pharmaceutical agents to peritoneum and associated lymph nodes. J. Pharmacol. Exp. Ther.* **2002**, *303*, 11-16.

(161) Bagh, S.; Paige, M. F., *Ensemble and single-molecule fluorescence spectroscopy of a calcium-ion indicator dye. J. Phys. Chem. A* **2006**, *110*, 7057-7066.

(162) Barkai, E.; Jung, Y. J.; Silbey, R., *Theory of single-molecule spectroscopy: Beyond the ensemble average. Annu. Rev. Phys. Chem.* **2004**, *55*, 457-507.

(163) Hoogenboom, J. P.; van Dijk, E.; Hernando, J.; van Hulst, N. F.; Garcia-Parajo, M. F., *Power-law-distributed dark states are the main pathway for photobleaching of single organic molecules. Phys. Rev. Lett.* **2005**, *95*, 097401.

(164) Darzacq, X.; Yao, J.; Larson, D. R.; Causse, S. Z.; Bosanac, L.; de Turris, V.; Ruda, V. M.; Lionnet, T.; Zenklusen, D.; Guglielmi, B.; Tjian, R.; Singer, R. H., *Imaging Transcription in Living Cells. Ann. Rev. Biophys.* **2009**, *38*, 173-196.

(165) Xie, X. S.; Choi, P. J.; Li, G. W.; Lee, N. K.; Lia, G., *Single-molecule approach to molecular biology in living bacterial cells. Ann. Rev. Biophys.* **2008**, *37*, 417-444.

(166) Brecht, M.; Radics, V.; Nieder, J. B.; Bittl, R., *Protein dynamics-induced variation of excitation energy transfer pathways. Proc. Natl. Acad. Sci. U. S. A.* **2009**, *106*, 11857-11861.

(167) Owen, D. M.; Williamson, D.; Rentero, C.; Gaus, K., *Quantitative Microscopy: Protein Dynamics and Membrane Organisation. Traffic* **2009**, *10*, 962-971.

(168) Fitter, J., *The perspectives of studying multi-domain protein folding. Cell. Mol. Life Sci.* **2009**, *66*, 1672-1681.

(169) Tinnefeld, P.; Buschmann, V.; Weston, K. D.; Sauer, M., *Direct observation of collective blinking and energy transfer in a bichromophoric system. J. Phys. Chem. A* **2003**, *107*, 323-327.

(170) Cordes, T.; Vogelsang, J.; Tinnefeld, P., *On the Mechanism of Trolox as Antiblinking and Antibleaching Reagent. J. Amer. Chem. Soc.* **2009**, *131*, 5018-+.

(171) Ishitobi, H.; Kai, T.; Fujita, K.; Sekkat, Z.; Kawata, S., *On fluorescence blinking of single molecules in polymers. Chem. Phys. Lett.* **2009**, *468*, 234-238.

(172) Suzuki, T.; Fujikura, K.; Higashiyama, T.; Takata, K., *DNA staining for fluorescence and laser confocal microscopy. J. Histochem. Cytochem.* **1997**, *45*, 49-53.

(173) Schiedt, J.; Weinkauf, R.; Neumark, D. M.; Schlag, E. W., *Anion spectroscopy of uracil, thymine and the amino-oxo and amino-hydroxy tautomers of cytosine and their water clusters. Chem. Phys.* **1998**, *239*, 511-524.

(174) Vogelsang, J.; Kasper, R.; Steinhauer, C.; Person, B.; Heilemann, M.; Sauer, M.; Tinnefeld, P., *A reducing and oxidizing system minimizes photobleaching and blinking of fluorescent dyes. Angew. Chem.-Int. Edit.* **2008**, *47*, 5465-5469.

(175) Ringemann, C.; Schonle, A.; Giske, A.; von Middendorff, C.; Hell, S. W.; Eggeling, C., *Enhancing fluorescence brightness: Effect of reverse intersystem crossing studied by fluorescence fluctuation spectroscopy. Chemphyschem* **2008**, *9*, 612-624.

(176) Mao, S.; Benninger, R. K. P.; Yan, Y. L.; Petchprayoon, C.; Jackson, D.; Easley, C. J.; Piston, D. W.; Marriott, G., *Optical lock-in detection of FRET using synthetic and genetically encoded optical switches. Biophys. J.* **2008**, *94*, 4515-4524.

(177) Marriott, G.; Mao, S.; Sakata, T.; Ran, J.; Jackson, D. K.; Petchprayoon, C.; Gomez, T. J.; Warp, E.; Tulyathan, O.; Aaron, H. L.; Isacoff, E. Y.; Yan, Y., *Optical lock-in detection imaging microscopy for contrast-enhanced imaging in living cells. Proc. Natl. Acad. Sci. U. S. A.* **2008**, *105*, 17789-17794.

(178) Rust, M. J.; Bates, M.; Zhuang, X. W., *Sub-diffraction-limit imaging by stochastic optical reconstruction microscopy (STORM). Nature Methods* **2006**, *3*, 793-795.

(179) Shroff, H.; Galbraith, C. G.; Galbraith, J. A.; Betzig, E., *Live-cell photoactivated localization microscopy of nanoscale adhesion dynamics. Nature Methods* **2008**, *5*, 417-423.

(180) Larkin, J. M.; Donaldson, W. R.; Knox, R. S.; Foster, T. H., *Reverse intersystem crossing in rose bengal. II. Fluence dependence of fluorescence following 532 nm laser excitation. Photochemistry and Photobiology* **2002**, *75*, 221-228.

(181) Gratz, H.; Penzkofer, A., *Saturable absorption dynamics in the triplet system and triplet excitation induced singlet fluorescence of some organic molecules. Chem. Phys.* **2001**, *263*, 471-490.

(182) Larkin, J. M.; Donaldson, W. R.; Foster, T. H.; Knox, R. S., *Reverse intersystem crossing from a triplet state of rose bengal populated by sequential 532-+1064-nm laser excitation. Chem. Phys.* **1999**, *244*, 319-330.

(183) Reindl, S.; Penzkofer, A., *Higher excited-state triplet-singlet intersystem crossing of some organic dyes. Chem. Phys.* **1996**, *211*, 431-439.

(184) Widengren, J.; Dapprich, J.; Rigler, R., *Fast interactions between Rh6G and dGTP in water studied by fluorescence correlation spectroscopy. Chem. Phys.* **1997**, *216*, 417-426.

(185) Gregor, I.; Heupel, M.; Thiel, E., *Precise fluorescence measurement for determination of photophysical properties of dyes. Chem. Phys.* **2001**, *272*, 185-197.

(186) Buschmann, V.; Weston, K. D.; Sauer, M., *Spectroscopic study and evaluation of red-absorbing fluorescent dyes. Bioconjugate Chem.* **2003**, *14*, 195-204.

(187) Jia, K.; Wan, Y.; Xia, A. D.; Li, S. Y.; Gong, F. B.; Yang, G. Q., *Characterization of photoinduced isomerization and intersystem crossing of the cyanine dye Cy3. J. Phys. Chem. A* **2007**, *111*, 1593-1597.